ibvt-Schriftenreihe

Schriftenreihe des Instituts für Bioverfahrenstechnik

der Technischen Universität Braunschweig

Herausgegeben von Christoph Wittmann

Band 42

Sequential Co-simulation as Method to Couple CFD and Biological Growth in a Yeast Reactor

Coupling of multiphase fluid dynamics and biological growth is a common area of application in process engineering. At the forefront, environmental conditions and rising energy cost force companies to optimize reactor systems and processes. In optimization problems virtual methods play a major role. Models form the basis of virtual methods.

Differences in time scales for computational fluid dynamics and biological growth make direct co-simulation infeasible. A sequential method has to be applied. This work proposes the sequential co-simulation in application to baker's yeast production in a 200 L bubble column reactor.

The method combines a module for fluid dynamics implemented in CFX by Ansys and a module for biological growth implemented in Matlab and Simulink by Mathworks. Data interfaces are defined for module changes between sequences. Switching from the fluid dynamics module to the growth module data is mapped to a reduced set of elements by the neural gas algorithm. Computational demand for sequences of growth is significantly reduced.

Validation of this method follows two steps. First, computational fluid dynamics are validated with experimental data for axial liquid velocity. Second, growth model and the sequential method are validated with cultivation data. Experimental data has been determined in the same bubble column reactor. Target prediction for the sequential co-simulation deviates less than three percent from measured values.

Keywords: Sequential, Co-simulation, Coupling, CFD, Biological Growth, Yeast, Bubble Column Reactor

Sequenzielle Co-Simulation zur Kopplung von CFD und biologischem Wachstum in einem Hefereaktor

Die Kombination aus Mehrphasenströmung und biologischem Wachstum findet eine weit verbreitete Anwendung in der Prozesstechnik. In erster Linie zwingen anspruchsvolle Auflagen zum Umweltschutz und steigende Energiepreise Unternehmen dazu ihre Anlagen und Prozesse zu optimieren. Virtuelle Methoden sind ein wesentliches Hilfsmittel zur Lösung von Optimierungsproblemen. Modelle stellen die Grundlage für diese Methoden dar.

Derzeit ist eine direkte Co-Simulation aufgrund unterschiedlicher Zeitskalen für die Berechnung von Strömungs- und Wachstumsvorgängen nicht machbar. Alternativ werden sequenzielle Methoden angewandt. In dieser Arbeit wird die sequenzielle Co-Simulation am Beispiel der Backhefeherstellung in einem 200 L Blasensäulenreaktor vorgestellt.

Implementiert ist diese Methode in Form von zwei Modulen. Das Modul für die Strömungssimulation ist in CFX von Ansys umgesetzt. Das Wachstumsmodell ist als Modul in Matlab und Simulink von Mathworks realisiert. Schnittstellen beschreiben die Datenübergabe zwischen den Sequenzen. Bei der Übergabe von CFX an Matlab werden die Daten mithilfe des Neural Gas Algorithmus einem reduzierten Elementsatz zugeordnet. Damit sinkt der Rechenbedarf für Wachstumssequenzen deutlich.

Die sequenzielle Co-Simulation wird in zwei Schritten validiert. Im ersten Schritt dienen Messungen der axialen Komponente der Flüssigkeitsgeschwindigkeit zur Validierung der numerischen Strömungssimulation. Im zweiten Schritt werden experimentell ermittelte Wachstumsdaten mit Ergebnissen des Wachstumsmodells und der sequenziellen Methode abgeglichen. Grundlage der Daten ist immer der gleiche Reaktor. Der mit der sequenziellen Co-Simulation berechnete Zielwert weicht weniger als drei Prozent vom Messwert ab.

Suchbegriffe: Sequenziell, Co-Simulation, Kopplung, CFD, Biologisches Wachstum, Hefe, Blasensäulenreaktor

Sequential Co-simulation as Method to Couple CFD and Biological Growth in a Yeast Reactor

Von der Fakultät für Maschinenbau
der Technischen Universität Carolo-Wilhelmina zu Braunschweig
zur Erlangung der Würde
eines Doktor-Ingenieurs (Dr.-Ing.)

genehmigte Dissertation

von Dipl.-Ing. Andreas Christian Vetter
aus Clausthal-Zellerfeld

FIT-Verlag
für Innovation und Technologietransfer
Paderborn 2009

Die folgende Arbeit wurde an der Technischen Universität Carolo-Wilhelmina zu Braunschweig an der Fakultät für Maschinenbau als Dissertation angefertigt.

Eingereicht am: 11. Juni 2009
Mündliche Prüfung am: 23. September 2009

Prüfungsvorsitz: Prof. Dr.-Ing. D. C. Hempel
1. Referent: Prof. Dr. rer. nat. A. Haarstrick
2. Referent: Prof. Dr.-Ing. M. Bohnet

Bibliographic Information

The German Library lists this publication in the German National Bibliography. Detailed information can be retrieved via internet from *http://dnb.ddb.de*.

ISSN 1431-7230, ISBN 978-3-932252-48-8

Acknowledgement

Herrn Prof. Dr. A. Haarstrick danke ich herzlich für die Betreuung meiner Arbeit, für zahlreiche Gespräche und für die persönliche Atmosphäre in der Arbeitsgruppe.

Herrn Prof. Dr. M. Bohnet danke ich für die freundliche und spontane Übernahme des Korreferats.

Herr Prof. Dr. D. C. Hempel gab mir die Möglichkeit an einem interessanten Projekt zu arbeiten und zu promovieren. Außerdem unterstützte er mich dabei und leitete die Prüfungskommission. Dafür vielen Dank.

Meinen Kollegen danke ich für die angenehme Zeit. Hervorheben möchte ich die außergewöhnliche Zusammenarbeit mit Christina Appel. Außerdem danke ich Detlev Rasch und Cornelia Wiebels, die durch Diskussionen und praktische Unterstützung zum Erfolg der Arbeit beigetragen haben.

Ein besonderer Dank geht auch an Sebastian Niedenführ, der durch seine Mitarbeit als studentische Hilfskraft und seine Studienarbeit Außergewöhnliches geleistet hat. Robert Walisko danke ich für die tatkräftige Unterstützung durch seine Diplomarbeit.

Liebsten Dank meiner Frau Roswitha für die Geduld und Unterstützung während dieser Zeit. Ohne sie wäre diese Arbeit nicht das, was sie ist.

Meiner Familie danke ich herzlich für die umfassende Unterstützung.

Auch Irina danke ich besonders herzlich für die Unterstützung und Motivation. Natürlich danke ich ebenso herzlich allen anderen Freunden und Unterstützern wie Christina, Andrea, Yvonne, Katina, Irena und noch einigen anderen.

Ich kann hier nicht alle namentlich erwähnen, danke aber allen, die mir geholfen haben und allen, von denen ich etwas gelernt habe.

I gratefully acknowledge the financial support by the German Federation of Industrial Research Associations "Otto von Guericke" e.V. (AiF). I also acknowledge the cooperation with the Versuchsanstalt der Hefeindustrie e.V. in Berlin (VH).

Wolfsburg, Oktober 2009

Publications

- Vetter, A. C.; Wiebels, C. V.; Schallenberg, J.; Enß, J. H.; Hempel, D. C.; Haarstrick, A.
  Importance and Influence of Bubble Size on Bubble Column Reactors
  7th German/Japanese Symposium on Bubble Columns, May 20th-23rd, 2006, Goslar, Germany, 189–194

- Wiebels, C. V.; Vetter, A. C.
  Modelling and Experimental Investigation of Oxygen Transfer and Gas Hold-up in Pilot Reactors
  VH Yeast Conference 2006, Hamburg, Germany, 65–80

- Vetter, A. C.
  Modelling and Sequencial Cosimulation of Selected Industrial Yeast Reactors
  VH Yeast Conference 2007, Berlin, Germany, 89–102

- Vetter, A. C.; Hempel, D. C.; Haarstrick, A.
  Sequential Cosimulation of Hydrodynamics and Growth for Optimization of Reactors and Processes
  International Conference on Multiphase Flow ICMF 2007, July 9th-13th, 2007, Leipzig, Germany, PS6-14

Contents

$\mathcal{S}$ **Summary** **xvii**

$\mathcal{Z}$ **Zusammenfassung** **xix**

1 Introduction and Scope **1**
1.1 Introduction 1
1.2 Scope of the Work 2

2 Fluid Dynamics and Simulation **5**
2.1 Bubble Column Reactors 5
2.2 Multiphase Flow in Simulation 7
2.2.1 Simulation Approaches 8
2.2.2 Bubble Size Classes 9
2.2.3 Bubble Drag 10
2.2.4 Bubble Induced Turbulence 10
2.2.5 Other Forces 11
2.2.6 Mass Transfer 12
2.2.7 Mesh Convergency 13
2.2.8 Single Phase Versus Multiphase 13
2.3 Biological Growth and Fluid Dynamics 14
2.4 Basic Equations 16
2.5 Bubbles and Bubble Swarms 20
2.6 Interface Momentum Transfer 22
2.7 Turbulence Model 25
2.8 Mass Transfer 28
2.9 System, Geometry and Simplifications 32

2.10 Mesh . . . 35
2.11 Simulation Conditions . . . 37

3 Fluid Velocity in Measurement and Simulation 41
3.1 Measurement Techniques . . . 41
3.1.1 Non-invasive Measurement Techniques . . . 42
3.1.2 Invasive Measurement Techniques . . . 43
3.2 Pressure Probe for Velocity Measurement . . . 46
3.3 Measured Velocity Profiles . . . 49
3.4 Simulated Velocity Profiles . . . 50

4 Growth Model 55
4.1 Saccharomyces cerevisiae . . . 55
4.2 Kinetic Growth Model . . . 56
4.3 Mass Balances . . . 60
4.4 Structure of the Implemented Model . . . 61

5 Cultivation of Yeast 63
5.1 Type of Cultivation . . . 63
5.2 Experimental Setup . . . 63
5.3 Cultivation Experiment . . . 65
5.4 Sample Analysis . . . 66
5.5 Cultivation Report . . . 66

6 Sequential Co-simulation 73
6.1 Principle of the Method . . . 73
6.2 Interfaces . . . 75
6.2.1 Interface from CFX to Matlab . . . 75
6.2.2 Interface from Matlab to CFX . . . 76
6.3 Sequencing . . . 77
6.4 Data Reduction . . . 79
6.4.1 Neural Gas Algorithm . . . 80
6.4.2 Neural Gas 2D Example . . . 80
6.5 Model Assumptions . . . 82

7 Sequential Co-simulation Example 83

8 Summary and Future Prospects 89

$\mathcal{R}$ **References** **91**

A Cantilever Probe **107**
A.1 Measuring Device 107
A.2 Eigen Frequencies of a Cantilever Beam 110
A.3 Calibration 112
A.4 Signal Analysis 114
A.5 Probe Angular Characteristic 115
A.6 Measured Velocity Profiles 117
A.7 Attempts in Measurement Development 117

B Constants and Parameters for the Growth Model **121**

C Material for Cultivation Experiments **123**
C.1 Instruments for Experimental Setup 123
C.2 Material for Experiments 124
C.3 Instruments for Analysis 125
C.4 Constants for the Pure Growth Model 125

$\mathcal{N}$ **Notation** **127**
$\mathcal{N}$.1 Variables 127
$\mathcal{N}$.2 Greek Symbols 135
$\mathcal{N}$.3 Universal Constants 136
$\mathcal{N}$.4 Special Symbols, Abbreviations 137

List of Figures

2.1 Reactor Geometry 33
2.2 Gassing System Detail 34
2.3 Mesh on Plane $z = 90$ and $z = 500$ 36

3.1 Cross Section of Pressure Probe 47
3.2 Pressure Probe and Inclined Tube Manometer 48
3.3 Measured and Simulated Velocity Profiles, 900 mm 51
3.4 Measured and Simulated Velocity Profiles, 1120 mm 52
3.5 Simulated Liquid Velocity, Planes $x = 0$, $y = 0$ 53

4.1 Implemented Model Structure 61

5.1 Reactor Flow Scheme 64
5.2 Biomass Dry Weight Concentration 67
5.3 Substrate Feed 68
5.4 Overall Volume 68
5.5 Glucose Concentration 69
5.6 Solved Oxygen Concentration 70

6.1 Sequential Co-simulation 74
6.2 Neural Gas Example, Original Data, Ten, 50 and 100 Epochs 82

7.1 Simulated Oxygen Concentration in Gas Phase, 0 h 84
7.2 Simulated Oxygen Concentration Water, 0 h, 12 h and 18 h . 85
7.3 Biomass Dry Weight Concentration, Sequential Co-simulation 87

A.1 Strain Gauge Probe 108

A.2 Cross Section of Strain Gauge Probe 108
A.3 Stain Gauge Bridge 109
A.4 Structure of the Measuring System 109
A.5 Cantilever With Example Load 110
A.6 Probe Angle Definition 113
A.7 Probe Calibrator 113
A.8 Calibration Curve 0° and 180° 114
A.9 Probe Angular Characteristic, 0.5 m/s 116
A.10 Measured and Simulated Velocity Profiles, 900 mm 118
A.11 Measured and Simulated Velocity Profiles, 1120 mm 119

List of Tables

2.1 Constants of k-ε Model 27
2.2 Maximum Allowed Element Size 37

6.1 Continuous Phase Physical Properties 77
6.2 Decision Criteria 79
6.3 NG Example Settings and Results 81

A.1 Calibration Polynomials 115

B.1 Model Parameters 122

C.1 Parameters of Pure Growth Simulation 126

Summary

Sequential Co-simulation as Method to Couple CFD and Biological Growth in a Yeast Reactor

Coupling of multiphase fluid dynamics and biological growth is a common area of application in process engineering. At the forefront, environmental conditions and rising energy cost force companies to optimize reactor systems and processes. In optimization problems virtual methods play a major role. Models form the basis of virtual methods.

Differences in time scales for computational fluid dynamics and biological growth make direct co-simulation infeasible. A sequential method has to be applied. This work proposes the sequential co-simulation in application to baker's yeast production in a 200 L bubble column reactor.

The method combines a module for fluid dynamics implemented in CFX by Ansys and a module for biological growth implemented in Matlab and Simulink by Mathworks. Data interfaces are defined for module changes between sequences. Switching from the fluid dynamics module to the growth module data is mapped to a reduced set of elements by the neural gas algorithm. Computational demand for sequences of growth is significantly reduced.

Validation of this method follows two steps. First, computational fluid dynamics are validated with experimental data for axial liquid velocity. Second, growth model and the sequential method are validated with cultivation data. Experimental data has been determined in the same bubble column reactor. Target prediction for the sequential co-simulation deviates less than three percent from measured values.

Zusammenfassung

Sequenzielle Co-Simulation zur Kopplung von CFD und biologischem Wachstum in einem Hefereaktor

Die Kombination aus Mehrphasenströmung und biologischem Wachstum findet eine weit verbreitete Anwendung in der Prozesstechnik. In erster Linie zwingen anspruchsvolle Auflagen zum Umweltschutz und steigende Energiepreise Unternehmen dazu ihre Anlagen und Prozesse zu optimieren. Virtuelle Methoden sind ein wesentliches Hilfsmittel zur Lösung von Optimierungsproblemen. Modelle stellen die Grundlage für diese Methoden dar.

Derzeit ist eine direkte Co-Simulation aufgrund unterschiedlicher Zeitskalen für die Berechnung von Strömungs- und Wachstumsvorgängen nicht machbar. Alternativ werden sequenzielle Methoden angewandt. In dieser Arbeit wird die sequenzielle Co-Simulation am Beispiel der Backhefeherstellung in einem 200 L Blasensäulenreaktor vorgestellt.

Implementiert ist diese Methode in Form von zwei Modulen. Das Modul für die Strömungssimulation ist in CFX von Ansys umgesetzt. Das Wachstumsmodell ist als Modul in Matlab und Simulink von Mathworks realisiert. Schnittstellen beschreiben die Datenübergabe zwischen den Sequenzen. Bei der Übergabe von CFX an Matlab werden die Daten mithilfe des Neural Gas Algorithmus einem reduzierten Elementsatz zugeordnet. Damit sinkt der Rechenbedarf für Wachstumssequenzen deutlich.

Die sequenzielle Co-Simulation wird in zwei Schritten validiert. Im ersten Schritt dienen Messungen der axialen Komponente der Flüssigkeitsgeschwindigkeit zur Validierung der numerischen Strömungssimulation. Im zweiten Schritt werden experimentell ermittelte Wachstumsdaten mit Ergebnissen des Wachstumsmodells und der sequenziellen Methode abgeglichen.

Grundlage der Daten ist immer der gleiche Reaktor. Der mit der sequenziellen Co-Simulation berechnete Zielwert weicht weniger als drei Prozent vom Messwert ab.

Chapter 1

Introduction and Scope

1.1 Introduction

Baker's yeast has a variety of fields of application. It is primarily used in bakeries as baking agent and as taste donator. Another growing field of application is the food industry in general using yeast extracts. In agriculture, the high protein content makes yeast an important part of modern animal feed. The nitrogen content is a reason for also using yeast as fertilizer. Beside these common areas, current research attempts to extend the applicability of yeast. An interesting example is the use of dead yeast cells to create hollow pigments for paper industry [147].

Yeast as a low price product requires efficient production in huge amounts. Therefore, in production large reactors with operation volumes up to several hundred cubic meters are used. Molasses as by-product of sugar industry usually serves as substrate. Without exception, production reactors are air-lift type reactors. They combine both, ease in handling because of only a few internal installations and a good mixing and aeration performance at relatively low energy input. Reactors are generally designed as bubble columns or air-lift loop reactors with static or dynamic gassing systems.

Installation as well as running costs are major reasons for decisions for a certain reactor type. Energy cost for oxygen support hold the principal share of running costs. On the one hand, the cost for buying a reactor are generally higher for dynamic in comparison to static gassing systems. On

the other hand, dynamic systems may show supreme energy efficiency and can thus help to reduce running costs [53]. With increasing environmental standards, the comprehensive efficiency of running and planned systems will win its share.

International pricing pressure with respect to the product yeast especially challenges industrialized nations where energy prices are at elevated levels and environmental standards increase running costs.

Industrial yeast strains have extensively been improved. Basically only changes due to different substrates are still subject of investigation. The yeast market is saturated or even oversaturated. As a consequence, optimization via market volume is not possible. Currently, yeast is delivered as block, as granulate, dry and as liquid to serve the special needs of customers. Increasing yeast quality and shelf life is taken for granted and cannot serve as argument for a rise in price. Thus, the only realistic way to increase international competitiveness is to reduce the running costs. First, the comprehensive need for energy has to be minimized and second, oxygen and mixing yield have to be maximized.

Understanding the flow characteristics, the reactive processes and the combination of both is substantial for optimization of yeast reactors. The aim is to produce with highest yield at lowest energy consumption. Therefore, mass transfer has to be enhanced. At the same time mass transfer is a complex function of the bubble size distribution, the mass transfer coefficient and thus, a function of the physical properties of the fluids. For a given set of fluid properties, also the gassing system and the operation conditions have their indirect share on mass transfer.

1.2 Scope of the Work

Coupling of multiphase fluid dynamics and biological growth is a common area of application in process engineering. The use of computational fluid dynamics in combination with growth models allows for general applicability to different reactor systems. Physics, biology, geometry and conditions are separately described.

Yeast cultivations last up to 24 hours. During cultivation parameters such as gas flow rate and volume may change. Accordingly, flow characteristics also change. Fluid dynamics and growth cannot be taken as being constant.

The direct interaction of fluid dynamics and growth requires combined simulations.

Related time scales differ and generally challenge to combine computational fluid dynamics and biological growth. While major changes in fluid dynamics happen within milli seconds to seconds, changes in growth may take hours to days. A direct co-simulation of this problem is not feasible.

The aim of this work is to develop a method to sequentially combine fluid dynamics and biological growth. Exemplary application in this work is baker's yeast production. Fluid dynamics are simulated with the commercial code CFX 11.0 by Ansys. The biological part has been implemented in Matlab and Simulink R2008a by Mathworks.

A 200 L reactor system is the basis for validation of simulated fluid dynamics and growth. The reactor is a bubble column with jet tubes as gassing system. This system has been chosen in relation to commonly applied industrial gassing systems. Axial liquid velocity serves to validate the fluid dynamics module. A cultivation experiment serves for validation of the growth model and the framework of sequential co-simulation. In contrast to industrial yeast production glucose directly serves as substrate.

Simulation of multiphase flow for reaction volumes above about five cubic meters is not practicable at the present time since element numbers rise up to billions. It is up to research and development in future decades.

Chapter 2

Fluid Dynamics and Simulation

2.1 Bubble Column Reactors

Bubble column reactors are vertically oriented cylinders with generally circular cross section area. Bubble columns are filled with liquid or liquid and solid to a certain level and aerated in the bottom section of the column.

These systems make use of the density difference between aeration gas and the liquid inside the reactor. The density difference in the gravitational field makes the gas bubbles rise. The slip velocity between gas and liquid causes drag forces and liquid motion is induced.

In general, bubble column reactors have only a few internal parts. As a result, their design is simple and cheap [93]. Being very easy and fast to clean is one of their greatest advantages.

In addition to fluid motion induced by bubble drag, fluid motion may be enforced. This directly influences the mean residence time of gas bubbles and may also increase oxygen utilization. As important as residence time are especially the total height of the column, the coalescence behavior in the adjacent multiphase mixture and the bubble size [120].

Additional parts may be installed in the bubble column in order to direct liquid and gas flow. The most common example is the group of airlift loop

reactors. The basic concept of such internal or external installations is the separation of liquid up- and down-flow regions.

In comparison to simple bubble column reactors, loop reactors may be operated with less energy input. Net draft tubes are used to even enhance mixing performance [57].

There are bubble columns of almost any size with volumes from some cubic centimeters up to about twenty thousand cubic meters. After decades of intense research on bubble columns the complete physical behavior is not entirely understood. Even though researchers have been trying to come up with general rules for scale-up [89, 135, 34, 137], up to now no general scale-up method is known which holds true for a relevant range of size.

Industrial application of bubble column reactors is as wide as their range in size. Typical areas are food production, chemical and biotechnological industry, processing and refinement of raw materials and waste water treatment [138, 46].

There are two basic concepts of gassing systems, static and dynamic. Static systems such as sparger plates, sieve plates and sintered plates are known to produce larger bubbles due to their position at the bottom of the reactor [133]. The change of flow direction at the bottom causes major radial velocity components and thus increased bubble coalescence in this area. A number of single vertically oriented nozzles as well as horizontally oriented tubes with holes or membranes and a distinct distance to the bottom of the column [29, 131] show much better performance.

Dynamic systems defined in the classical way are mainly injector and ejector nozzles [23] or liquid jets applied to the free liquid surface similar to sprinkling systems [23, 120]. The latter type of system is still used for oxygenation of biological systems with relatively low oxygen consumption. The modern definition of dynamic gassing systems relates to systems with moving parts such as rotors with openings on their surface [13, 96, 53]. The dynamic pressure at certain areas of rotating parts reduces the local pressure such that gas is intaken with low or even without positive primary pressure.

In combination with additional installations for bubble distribution, such systems reach very homogeneous gas distributions, small bubbles and good mixing performance. Additional parts impede cleaning. Up to now, no generally accepted optimum gassing system is known.

The bubble size distribution depends upon used liquids, solids and gases, the gassing system, the gas flow rate, the column dimensions and even more factors. At the same time, this distribution causes a certain gas holdup and

the related liquid flow field [93]. The effects are coupled in a complex manner which makes research especially on scale-up as difficult as it is.

2.2 Multiphase Flow in Simulation

In bubble column reactors a continuous liquid phase is gassed with a dispersed gaseous phase. The holdup or volume fraction characterizes whether a phase is regarded to being continuous or dispersed [75].

The complexity of model description increases with increasing number of phases. In practice, the number of adjacent phases is reduced to the smallest physically meaningful set. In bubble column reactors for yeast production there are a liquid and a gas phase as well as a solid phase representing yeast cells. Since yeast cells have a diameter of 5 to 10 μm and a mass density very similar to water, in approximation the solid phase can be omitted for most simulations. Yeast cells almost perfectly follow the flow and do not significantly change flow characteristics. The suspension is treated as one pseudo phase with fluid characteristics of water.

Oxygen is one of the central components for yeast growth of interest in this case, thus oxygen has explicitly to be taken into account in the simulation. Oxidative yeast growth consumes oxygen while producing carbon dioxide. Oxygen is transferred from gas into liquid phase and carbon dioxide leaves the liquid in the opposite direction. For simplicity reasons, the number of oxygen molecules entering the liquid phase is assumed to be of the same order as the number of carbon dioxide molecules leaving it. Accordingly, volume changes in the gas phase due to biological growth are negligible.

Bubble column reactors obviously show three dimensional and time dependent flow fields. Nevertheless, time averaged information corresponds to a probability of occurrence and thus gives hints for optimization. It is common sense that the transient character of the flow field also has to be taken into account. The flow field is characterized by its unsteadiness and the turbulence.

Computer resources limit computational fluid dynamics. In order to simulate systems of relevant size, first approaches have therefore been reduced to two dimensions. Such a simplification is allowed when the system has at least one almost infinite dimension not being the main flow direction. This dimension may often be omitted without the loss of important information.

Even though columns with rectangular cross section do not fulfill this requirement, literature shows that researchers often neglect the direction of lowest extension [20, 11]. The assumption of two dimensionality is not justified in most simulations of bubble columns but especially not for those with a circular cross section area [49, 105, 91, 30, 126, 54, 115]. Continuity requirements must provide different flow fields for columns with rectangular and with circular cross section area. Most systems of industrial relevance do have a circular cross section area.

The top region of bubble column reactors is filled with the gas leaving the mixture of gas and liquid. This interface in the top region between gas and the mixture of gas and liquid is called free surface. It is not a sharp boundary. Simulations with free surfaces in heterogeneous multiphase systems give rise to severe difficulties. As long as the free surface is not of special interest it can be approximated by a plane surface where no shear forces occur. Thus, the computational domain can be reduced to the region captured by the gas liquid mixture. This method is generally accepted [86, 11, 115].

2.2.1 Simulation Approaches

There are two main approaches in simulation of multiphase flow. The first approach deals with descriptions of systems where one finite volume element may contain more than one phase. This kind of description is named disperse and is known as Euler-Lagrange or Euler-Euler [44]. In the second approach the phase boundary is tracked for all cells [78]. Descriptions of this kind are therefore named separated. The best known description is the Volume of Fluid method.

The Euler-Lagrange method treats the dispersed phase as separated particles of zero volume. The trajectories for every single particle are calculated based on the main flow field of the continuous phase [44]. This method gives insight into dispersed phase flows [43]. The approach suffers from computational demand. Therefore, simulations using the Euler-Lagrange approach are limited to a number of some thousand dispersed phase particles. Bubble columns with millions of bubbles per cubic meter cannot realistically be described.

The Euler-Euler method is also called two fluid or multi fluid method. The different phases are treated as inter-penetrating continua [44]. Thus, this method does not account for direct particle interaction. There is a mass and momentum conservation equation for every fluid. The volume fraction

of every single phase is calculated for all volume elements [125]. The Euler-Euler method is applicable for high volume fractions of the dispersed phase. Its computational demand is relatively modest. This is the main reason for the wide usage of this approach [126].

In contrast, the Volume of Fluid method captures the shape and even the shape deformation of single dispersed particles [43, 79]. Obviously, it is the physically most realistic way of simulating multiphase systems. The method has been applied to single bubble motion as well as to bubble interactions [15]. It is a great tool to study principle behavior of bubbles and to deduce advanced drag, break-up and coalescence models [15]. At the same time, it is computationally so demanding that only a few bubbles can be simulated at the present time. As a consequence, the Volume of Fluid approach suffers from similar limitations as experiments. Up to now, this method has not come up with overall better performing models.

2.2.2 Bubble Size Classes

The discussion about one definite bubble size versus bubble size distributions is as old as simulation of bubble columns. In real systems independent from the flow regime, there is always a bubble size distribution. Gas holdup, surface tension as well as influencing surface active agents and forces entail distributions of different sharpness. In simulations bubble size classes represent bubble size distributions. In most cases, bubble size is kept constant for every single class over the entire reactor.

Simple approaches use one averaged bubble size where averaging is problem related [126]. It has been shown that one single bubble size does not always capture flow physics [16]. Thus, researchers often apply two bubble size classes [81, 138, 101, 115]. These classes may interact with each other but also may coexist without interaction still enhancing the results. The assumption of two bubble size classes representing the distribution adequately results from dynamic disengagement experiments for aqueous systems [119, 68].

Population balances based on breakup and coalescence models are used to most realistically represent bubble size distributions [32]. Restricted computational resources often demand for simplified models based on the idea of population balances. An early approach is a kinetic model for the bubble rise velocity based on experimental knowledge [68]. The bubble size distribution might for example also be reduced to a local mean bubble size [32]. Other researchers use population balances to calculate bubble size distributions and

to reduce those to a finite number of bubble size classes. In a second step, the classes are used for Euler-Euler simulations [101, 115]. This approach is similar to the use of experimentally determined representative bubble size classes [54, 149].

Up to now, most implementations of population balances capture effects such as mass transfer but do not account for interphase forces based on local bubble size distributions. Instead, one single rise velocity is assumed for all bubbles. For correct simulations of the flow field, the interphase forces such as the drag force are of special importance. The first serious approach of taking into account such detailed interaction has been published in 2008 [18].

2.2.3 Bubble Drag

The drag force is the most important one acting between the continuous and the dispersed phase [32]. The fact that both phases are fluids results in possible motions inside the bubble and in generally deformable surfaces. Gas compressibility, viscosity and surface active forces make the system very complex.

There is no general applicable or accepted model for the drag force accounting for all known effects in any system. Most models are based on experiments or detailed simulation of very few bubbles [15]. They are therefore restricted in their application. Complexity on the one hand and the major importance of the drag force for simulation on the other hand are the present challenge in simulating bubble column reactors [16, 32].

2.2.4 Bubble Induced Turbulence

Bubble induced turbulence is the influence of moving bubbles on continuous phase turbulence [24]. Bubbles may increase as well as decrease the level of turbulence by their flexible surface and their wake structure depending on the flow [126]. Even though models for bubble induced turbulence have been developed for decades, the deduced models are still suffering from not understanding the exact physics behind.

There are three basic approaches to describe bubble induced turbulence in bubble column reactors. The first approach accounts for bubble induced effects by superposition of a shear and a bubble induced term for the effective viscosity [114, 112, 113, 92]. The additional term is taken to be proportional to gas holdup and slip velocity. The second approach assumes bubbles to

influence liquid turbulence by displacement of liquid while bubbles move. Similarly to the first model, a shear induced and a bubble induced term are superposed to form the stress tensor [126]. The third approach assumes bubbles to influence turbulence production and dissipation. Source terms for turbulent kinetic energy as well as for turbulent energy dissipation rate are derived [71].

Comparison of models has shown the third approach to give the best results [101] while the first two approaches often underestimate the effect [126]. Models of this type have widely been applied in simulations [105, 84, 90, 126, 115].

2.2.5 Other Forces

In addition to the drag force acting on moving gas bubbles, other forces such as added mass force, lift force or turbulent dispersion force are subject of current research. Physics behind are not entirely understood wherefore models and even effects are not generally accepted. Some researchers propose a force concept dividing forces into two groups. The first group describes physically validated forces while the second group describes forces with significant effect in numerical simulation [124, 126].

The drag force represents the force of liquid acting on the constantly moving dispersed phase. For accelerated bubbles, liquid in the bubble wake has also to be accelerated and causes an additionally decelerating force [124]. Even though the effect of added mass force or virtual mass force is generally accepted because of its physical plausibility, experimental determination and thus modeling is still complicated. The added mass force so far is known as a tuning parameter also leading to numerical difficulties and may be neglected [32, 138]. Since highly accelerated flow situations are the basis of added mass force, the effect is referred to being high frequency related. Most multiphase flow simulations do not resolve high frequency effects. As a consequence, added mass force must not separately be accounted for [124].

The concept of lift force, lateral or radial force describes forces perpendicular to the incident flow direction such as Magnus force or Saffmann force. For bubbly flows, there is no theoretical concept because of the complexity of bubble motion [124]. Current practice of modeling superposes physically not entirely understood effects. As a consequence, models are very uncertain [126, 32]. A fair amount of published literature presents lift force for better fit of experiment and simulation [138, 124]. Due to uncertainty and the lack

of knowledge based on physics, it is accepted to neglect lift force. Simulation results without lift force are not reported to be worse [138, 126, 32]. Lately published experimental work emphasizes uncertainty and further need of investigation [82].

Turbulent dispersion is based on turbulent motion of the liquid phase. Turbulence additionally disperses gas bubbles. The force is known to have a significant impact [47]. Even though there are well known examples without application of turbulent dispersion force [105, 32], many researchers claim for the need of application [126, 27]. The latest work on turbulent dispersion force introduces a random dispersion model. It directly deduces turbulent dispersion effects from the local flow characteristics and works without adjustable parameters [48]. The random turbulent dispersion model promises more physically founded simulations.

2.2.6 Mass Transfer

Since flow physics are only one aspect of bubble columns and reactions are the other, a word has to be said about mass transfer. For application to simulation there are two basic approaches to describe mass transport from one phase into the other. The first assumes the transferred component to be an additional variable without direct influence on flow physics. The second approach divides the fluids into components. Mass transfer then directly influences fluid characteristics. In both cases the transfer rate has to be defined via source and sink terms for the mass balance equation of each phase.

Often, mass transfer simulations are of major importance for reactor design. Therefore, models shall be as general as possible to be applied to reactors of any scale. Resilient simulation results have to be produced in a short time. On the one hand, using correlations for mass transfer is very fast but suffers from the need of experience, knowledge and assumptions. On the other hand models based on detailed fluid dynamics simulations can be generally applied but cost a lot of time and computational power. This is why different approaches for mass transfer coexist today.

The most classical way of simulating mass transfer is the use of empirical correlations [72]. Correlations are easily applied to modern CFD codes. CFD methods have been in use for a good decade now. Before, compartment models have been used. The fluid domain is divided into very few compartments. Mass and momentum conservation equations are applied. Assuming

perfect mixing for any compartment, this method quickly gives acceptable results [123]. There are even system based macro scale models without directly accounting for fluid flow [148, 153].

In CFD simulations most researchers do not directly couple mass transfer to fluid dynamics but treat transferred components as non-reactive tracers in the relevant phases. Mass transfer is modeled to depend upon differences in partial pressure of the components in adjacent phases. Either a single bubble size class or a mean bubble diameter is used for local mass transfer calculation [139, 80, 90]. Advanced approaches use several size classes with a population balance model for detailed local mass transfer calculation [45, 146].

Volume of Fluid or Euler-Lagrange approaches are restricted in a systematic manner. Nevertheless, some researchers have presented very good results [73, 40]. Even though these methods cannot be used for large systems in the near future, they may help to increase model quality for less detailed approaches in parallel to experiments.

2.2.7 Mesh Convergency

As stated in section 2.10, the mesh convergency study is a basic method to assure simulation results to be grid independent. This is meant to be general consensus but few researchers report convergency studies [126]. In general, the mesh has to be as fine as the scale of physics [105]. Small scale turbulence would demand for micro scaled grid cells which is unrealistic for most problems. This is why models account for small scale effects and the size of grid cells can be increased accordingly. Nevertheless, coarser grids are the reason for increased discretization error.

It has been reported that refinement of the cell size to one fifth of the Kolmogorov length scale entails apparently grid independent results [11]. Even though this is out of question for applications of industrial significance, it clearly points out the vagueness of the current state of multiphase flow simulation.

2.2.8 Single Phase Versus Multiphase

Single phase simulation has reached a high level prediction quality not making use of too much empirical models. At the same time multiphase simulation is much less reliable due to the number of effects, the reduced knowledge and understanding of multiphase related physics and the corresponding modeling

difficulties. It is common sense that on top of the complexity are uniformly aerated systems such as bubble column reactors [16, 126].

In this complexity the aim has to be to simulate significant systems in finite time reaching acceptable results. As long as computational resources in majority restrict multiphase flow simulations, an engineering level of accuracy has to be seen as the state of the art [32]. Further research has thus two objectives. First, to study physics in detail and second, to come up with knowledge based models and approaches capturing the main physics, being applicable to real world problems at the same time [83].

2.3 Biological Growth and Fluid Dynamics

A major number of applications of multiphase flow dynamics is related to chemical reactions or biological growth. Accordingly, early attempts have been made to co-simulate fluid dynamics and reaction or growth.

Models range theoretically from overall growth models without fluid dynamics to directly coupled direct numerical simulation and metabolic flux models [145]. On the one hand, former models are too simple especially for large scale applications in order to give reliable results. On the other hand, latter models are currently not manageable for lack of computational power and knowledge about physics and biology.

Compartment or zone models discretize the reactor into a very small number of elements. Discretization generally follows information about the flow field of the related problem [145]. As a consequence, detailed experimental information about the flow field has to be known up-front. Reaction or growth is simulated as well as exchange between the compartments or zones. The simplicity of the model does not limit application with respect to dimension or time.

An external airlift loop reactor can thus be represented by a top and a bottom section with perfect mixing as well as by a riser and a downcomer with axial dispersion [154]. In a similar manner, compartments of agitator vessels are defined based on long time averaged information about the flow field [97].

Similarly, cell models need some information about the flow characteristics. Simple models are based on circle time distributions using element numbers in the order of 10 [5]. Since detailed information about the flow

field is not needed, this model is more generally applicable by nature. Cycle time information is easily accessible in experiments.

Advanced cell models with general flow definitions between adjacent cells can be seen as early stages of modern computational fluid dynamics formulations in combination with reaction and growth [8]. Nevertheless, information about flow is fed into discretization.

A fair amount of models utilizes computational fluid dynamics to come up with reduced order maps while reaction or growth is simulated on the mapped system only. Basic assumption of this approach is one-way coupling [118, 108, 69]. Hence, reaction does not influence fluid dynamics significantly. The advantages of a reduced but mapped system for reaction and growth are the reduction of computational cost and the proximity to the real application [69].

Some models use long time averaged information of the flow field to come up with zone models [9, 10]. Advanced approaches iteratively optimize the flow field mapping once before transient simulation of growth [108]. It is sufficient to calculate the mapping only once if flow fields are virtually stationary and volume changes are negligible [118].

The model proposed in this work maps flow field information of a computational fluid dynamics calculation to a reduced set of elements. The mapping automatically accounts for element density of the original grid. Transient growth is simulated on the mapped system for a defined time. The results are back-mapped to the original grid or to a new grid related to volume changes before again simulating fluid dynamics and mass transfer. This method is referred to as sequential co-simulation (chapter 6).

A basic model assumption is that fluid dynamics are not significantly influenced by biological growth except for surface tension (section 2.11). Each sequence may maximally be as long as changes to fluid dynamics can be assumed to be small. On the one hand, this method obviously consumes more computational resources than the methods mentioned before. On the other hand, it is generally applicable and provides a feasible method for simulation of long lasting processes.

Even more advanced approaches directly couple fluid dynamics simulations and fast chemical reactions [110, 39, 69, 40]. At the present time, no feasible approach other than the proposed is known for direct coupling of fluid dynamics and biological growth, simulating relevant real time. The basic problem of direct coupling lies in differences in time scales wherefore either of the domains is not sufficiently represented. Thus, direct coupling

does only make sense for involved domains with similar and small time scales such as for fast chemical reactions.

2.4 Basic Equations

The basic equations of fluid flow are derived from conservation laws, namely the conservation of mass, the conservation of momentum and the conservation of energy.

In the following, the governing equations in three dimensions for compressible fluids in multiphase flow are shown in detail. There is a single set of equations for each phase with additional interface exchange and source terms. With the phase holdup r_α for phase α or alternatively r_β for phase β equation 2.1 defines the continuity equation [143].

$$\frac{\partial(r_\alpha \varrho_\alpha)}{\partial t} + \frac{\partial(r_\alpha \varrho_\alpha u_\alpha)}{\partial x} + \frac{\partial(r_\alpha \varrho_\alpha v_\alpha)}{\partial y} + \frac{\partial(r_\alpha \varrho_\alpha w_\alpha)}{\partial z} = S_{M\alpha} + \sum_{\beta=1}^{N_\beta} \Gamma_{\alpha\beta} \quad (2.1)$$

$S_{M\alpha}$ are defined mass sources and $\Gamma_{\alpha\beta}$ are the mass flow rates from all N_β phases to phase α.

The equations of conservation of momentum follow [100].

$$\begin{aligned} \frac{\mathrm{D}(r_\alpha \varrho_\alpha u_\alpha)}{\mathrm{D}t} = & -r_\alpha \frac{\partial p_\alpha}{\partial x} + \eta_\alpha \left(\frac{\partial^2(r_\alpha u_\alpha)}{\partial x^2} + \frac{\partial^2(r_\alpha u_\alpha)}{\partial y^2} + \frac{\partial^2(r_\alpha u_\alpha)}{\partial z^2} \right) + \\ & \eta_\alpha \left(\frac{\partial^2(r_\alpha u_\alpha)}{\partial x^2} + \frac{\partial^2(r_\alpha v_\alpha)}{\partial y \partial x} + \frac{\partial^2(r_\alpha w_\alpha)}{\partial z \partial x} \right) + \\ & \lambda_\alpha \left(\frac{\partial^2(r_\alpha u_\alpha)}{\partial x^2} + \frac{\partial^2(r_\alpha v_\alpha)}{\partial x \partial y} + \frac{\partial^2(r_\alpha w_\alpha)}{\partial x \partial z} \right) + \\ & \sum_{\beta=1}^{N_\beta} (\Gamma_{\alpha\beta} u_\beta - \Gamma_{\beta\alpha} u_\alpha) + S_{Mx\alpha} + M_{\alpha x} \end{aligned} \quad (2.2)$$

$$\begin{aligned}\frac{\mathrm{D}(r_\alpha \varrho_\alpha v_\alpha)}{\mathrm{D}t} &= -r_\alpha \frac{\partial p_\alpha}{\partial y} + \eta_\alpha \left(\frac{\partial^2 (r_\alpha v_\alpha)}{\partial x^2} + \frac{\partial^2 (r_\alpha v_\alpha)}{\partial y^2} + \frac{\partial^2 (r_\alpha v_\alpha)}{\partial z^2} \right) + \\ & \eta_\alpha \left(\frac{\partial^2 (r_\alpha u_\alpha)}{\partial x \partial y} + \frac{\partial^2 (r_\alpha v_\alpha)}{\partial y^2} + \frac{\partial^2 (r_\alpha w_\alpha)}{\partial z \partial y} \right) + \\ & \lambda_\alpha \left(\frac{\partial^2 (r_\alpha u_\alpha)}{\partial y \partial x} + \frac{\partial^2 (r_\alpha v_\alpha)}{\partial y^2} + \frac{\partial^2 (r_\alpha w_\alpha)}{\partial y \partial z} \right) + \\ & \sum_{\beta=1}^{N_\beta} (\Gamma_{\alpha\beta} v_\beta - \Gamma_{\beta\alpha} v_\alpha) + S_{My\alpha} + M_{\alpha y} \end{aligned} \tag{2.3}$$

$$\begin{aligned}\frac{\mathrm{D}(r_\alpha \varrho_\alpha w_\alpha)}{\mathrm{D}t} &= -r_\alpha \frac{\partial p_\alpha}{\partial z} + \eta_\alpha \left(\frac{\partial^2 (r_\alpha w_\alpha)}{\partial x^2} + \frac{\partial^2 (r_\alpha w_\alpha)}{\partial y^2} + \frac{\partial^2 (r_\alpha w_\alpha)}{\partial z^2} \right) + \\ & \eta_\alpha \left(\frac{\partial^2 (r_\alpha u_\alpha)}{\partial x \partial z} + \frac{\partial^2 (r_\alpha v_\alpha)}{\partial y \partial z} + \frac{\partial^2 (r_\alpha w_\alpha)}{\partial z^2} \right) + \\ & \lambda_\alpha \left(\frac{\partial^2 (r_\alpha u_\alpha)}{\partial z \partial x} + \frac{\partial^2 (r_\alpha v_\alpha)}{\partial z \partial y} + \frac{\partial^2 (r_\alpha w_\alpha)}{\partial z^2} \right) + \\ & \sum_{\beta=1}^{N_\beta} (\Gamma_{\alpha\beta} w_\beta - \Gamma_{\beta\alpha} w_\alpha) + S_{Mz\alpha} + M_{\alpha z} \end{aligned} \tag{2.4}$$

Γ-terms on the righthand side of equations 2.2 to 2.4 represent interphase momentum transfer due to interphase mass flow. The S_M-terms stand for external body forces as well as for user defined momentum sources. Finally, the M-terms represent interphase momentum exchange such as drag forces. An accepted working approximation for the second dynamic viscosity is $3\lambda_\alpha = -2\eta_\alpha$ [143, 116].

Two additional classes of equations make the set of equations complete. First, the conservation of volume (equation 2.5) and second, the pressure constraints, assuming the pressure to be the same for all phases (equation 2.6) [1].

$$r_\alpha + \sum_{\beta=1}^{N_\beta} r_\beta = 1 \tag{2.5}$$

$$p_\beta = p \qquad \forall\, \beta = 1, \ldots, N_\beta \tag{2.6}$$

The Navier-Stokes equations account for all effects of a compressible turbulent flow, i.e. the random and three-dimensional behavior. Since turbulence consists of many different length scales and relevant turbulent flows are described by high Reynolds numbers, simulations using the Navier-Stokes equations require very fine meshes and very small time steps to completely resolve turbulence effects. Generally, problem geometries are far too big to be simulated with direct numerical simulation (DNS). Even in the near future under the assumption of continued fast development of computational power, practical problems will not be solved by DNS in the next decades [143].

In many cases time-averaged information about flow fields is sufficient. Thus, the instantaneous turbulent information does not necessarily have to be calculated. The mean Φ of a flow property $\varphi(t)$ is defined [65].

$$\Phi = \frac{1}{\Delta t} \int_0^{\Delta t} \varphi(t) \mathrm{d}t. \tag{2.7}$$

The variables can be seen as being combined of a mean Φ and a time-varying portion φ'. By definition, the time average of the time-varying portion has to be zero. Time-averaged portions are marked by an over-line and time-varying portions by a prime.

$$\varphi(t) = \Phi + \varphi'(t) \tag{2.8}$$

$$\overline{\varphi'} = \frac{1}{\Delta t} \int_0^{\Delta t} \varphi'(t) \mathrm{d}t \equiv 0 \tag{2.9}$$

Application of equation 2.8 to the variables u, v, w and p in the equations 2.1 to 2.4 and averaging leads to the following set of equations for every single phase called the Reynolds averaged Navier-Stokes equations (RANS).

$$\frac{\partial(r_\alpha \varrho_\alpha)}{\partial t} + \frac{\partial(r_\alpha \varrho_\alpha U_\alpha)}{\partial x} + \frac{\partial(r_\alpha \varrho_\alpha V_\alpha)}{\partial y} + \frac{\partial(r_\alpha \varrho_\alpha W_\alpha)}{\partial z} = S_{M\alpha} + \sum_{\beta=1}^{N_\beta} \Gamma_{\alpha\beta} \tag{2.10}$$

$$\frac{\mathrm{D}(r_\alpha \varrho_\alpha U_\alpha)}{\mathrm{D}t} = -r_\alpha \frac{\partial P_\alpha}{\partial x} + \eta_\alpha \left(\frac{\partial^2 (r_\alpha U_\alpha)}{\partial x^2} + \frac{\partial^2 (r_\alpha U_\alpha)}{\partial y^2} + \frac{\partial^2 (r_\alpha U_\alpha)}{\partial z^2} \right) + \eta_\alpha \left(\frac{\partial^2 (r_\alpha U_\alpha)}{\partial x^2} + \frac{\partial^2 (r_\alpha V_\alpha)}{\partial y \partial x} + \frac{\partial^2 (r_\alpha W_\alpha)}{\partial z \partial x} \right) + \lambda_\alpha \left(\frac{\partial^2 (r_\alpha U_\alpha)}{\partial x^2} + \frac{\partial^2 (r_\alpha V_\alpha)}{\partial x \partial y} + \frac{\partial^2 (r_\alpha W_\alpha)}{\partial x \partial z} \right) + \left[-\frac{\partial \left(r_\alpha \varrho_\alpha \overline{u_\alpha'^2} \right)}{\partial x} - \frac{\partial (r_\alpha \varrho_\alpha \overline{u_\alpha' v_\alpha'})}{\partial y} - \frac{\partial (r_\alpha \varrho_\alpha \overline{u_\alpha' w_\alpha'})}{\partial z} \right] + S_{Mx_\alpha} + M_{\alpha x} \tag{2.11}$$

$$\frac{\mathrm{D}(r_\alpha \varrho_\alpha V_\alpha)}{\mathrm{D}t} = -r_\alpha \frac{\partial P_\alpha}{\partial y} + \eta_\alpha \left(\frac{\partial^2 (r_\alpha V_\alpha)}{\partial x^2} + \frac{\partial^2 (r_\alpha V_\alpha)}{\partial y^2} + \frac{\partial^2 (r_\alpha V_\alpha)}{\partial z^2} \right) + \eta_\alpha \left(\frac{\partial^2 (r_\alpha U_\alpha)}{\partial x \partial y} + \frac{\partial^2 (r_\alpha V_\alpha)}{\partial y^2} + \frac{\partial^2 (r_\alpha W_\alpha)}{\partial z \partial y} \right) + \lambda_\alpha \left(\frac{\partial^2 (r_\alpha U_\alpha)}{\partial y \partial x} + \frac{\partial^2 (r_\alpha V_\alpha)}{\partial y^2} + \frac{\partial^2 (r_\alpha W_\alpha)}{\partial y \partial z} \right) + \left[-\frac{\partial (r_\alpha \varrho_\alpha \overline{u_\alpha' v_\alpha'})}{\partial x} - \frac{\partial \left(r_\alpha \varrho_\alpha \overline{v_\alpha'^2} \right)}{\partial y} - \frac{\partial (r_\alpha \varrho_\alpha \overline{v_\alpha' w_\alpha'})}{\partial z} \right] + S_{My_\alpha} + M_{\alpha y} \tag{2.12}$$

$$\frac{\mathrm{D}(r_\alpha \varrho_\alpha W_\alpha)}{\mathrm{D}t} = -r_\alpha \frac{\partial P_\alpha}{\partial z} + \eta_\alpha \left(\frac{\partial^2 (r_\alpha W_\alpha)}{\partial x^2} + \frac{\partial^2 (r_\alpha W_\alpha)}{\partial y^2} + \frac{\partial^2 (r_\alpha W_\alpha)}{\partial z^2} \right) + \eta_\alpha \left(\frac{\partial^2 (r_\alpha U_\alpha)}{\partial x \partial z} + \frac{\partial^2 (r_\alpha V_\alpha)}{\partial y \partial z} + \frac{\partial^2 (r_\alpha W_\alpha)}{\partial z^2} \right) + \lambda_\alpha \left(\frac{\partial^2 (r_\alpha U_\alpha)}{\partial z \partial x} + \frac{\partial^2 (r_\alpha V_\alpha)}{\partial z \partial y} + \frac{\partial^2 (r_\alpha W_\alpha)}{\partial z^2} \right) + \left[-\frac{\partial (r_\alpha \varrho_\alpha \overline{u_\alpha' w_\alpha'})}{\partial x} - \frac{\partial (r_\alpha \varrho_\alpha \overline{v_\alpha' w_\alpha'})}{\partial y} - \frac{\partial \left(r_\alpha \varrho_\alpha \overline{w_\alpha'^2} \right)}{\partial z} \right] + S_{Mz_\alpha} + M_{\alpha z} \tag{2.13}$$

In equations 2.11 to 2.13 the terms in square brackets result from the averaging process. These nine terms of which six are independent are the so called Reynolds stresses. It is worth mentioning that the terms are apparent stresses. They have the character of stress terms but result from the averaging process. Reynolds stresses are the resulting problem since they are unknown. The set of equations is not closed. Objective of turbulence models is a sensible description of the six independent Reynolds stresses (**section 2.7**).

2.5 Bubbles and Bubble Swarms

Density difference causes bubbles to move in the opposite direction of the gravitational vector. The movement applies different forces to the bubble surface and consequently often results in breakup and coalescence. A dynamic equilibrium between breakup and coalescence may result [21].

Traditionally, bubbles are classified due to their shape. The shape very much depends on fluid characteristics. For air-water systems bubbles up to a diameter of 0.5 mm are referred to being rigid spheres. Medium sized bubbles with diameters between 0.5 and 2.5 mm are characterized by spherical shape but with inner gas circulation [35]. This effect is also known as Marangoni effect [73].

Bubbles with diameters above 2.5 mm have a mobile surface and ellipsoidal shape. With increasing diameter, inner circulation depends upon different eddies and thus, bubble shape becomes irregular. Such bubbles moving in undisturbed liquid may form caps giving the name of this class [23]. Apart from cap bubbles, breakup becomes a significant effect, limiting bubble diameter to dynamic maximum stable diameter.

For small bubbles surface tension forces are the main effect for shape and behavior. With increasing diameter the influence of inertia forces increases while the influence of surface tension forces decreases. For large bubbles, surface tension forces are negligible [55].

Continuity reasons force liquid motion due to bubble motion. Bubble shape, size and the number of bubbles decide whether liquid moves locally or globally. Behind bubbles a wake structure is formed. Depending on flow conditions as well as on fluid characteristics, wake structure varies from closed laminar to open turbulent [55, 36]. Liquid in front of the bubble and in the bubble wake has to be accelerated which is the physical explanation for virtual

mass formulations [73]. This effect is comparable to virtual increase in bubble volume [141, 117].

Bubble shape, size and behavior are influenced by the reactor geometry, the liquid, surface active agents as well as solid particles, the inlet conditions, presence of other bubbles and the flow field. Complexity arises from these effects being highly coupled [35].

Increasing liquid viscosity reduces the influence of acceleration effects [78]. Salinity together with other surface active agents directly influences bubble behavior [17]. These molecules and particles accumulate at the interface. In many cases the accumulation is characterized by gradients with highest concentrations at the bubble wake. As a consequence, inner circulation is reduced, bubble shape is stabilized and coalescence is hindered [31].

It has been shown that initial deformation is an important parameter for bubble shape and movement [73]. Highly deformed bubbles form ellipsoids and move on helical paths while initially spherical bubbles may keep their shape and move upwards on an almost straight line. Inlet velocity as well as sparger type and geometry decide about initial deformation. The adjacent flow field has an important impact as permanent boundary condition.

In bubble columns bubbles move as group or swarm. Swarm velocity might be up to the sixfold the velocity of a single bubble [78]. With decreasing distance between bubbles, a following bubble accelerates and reaches the velocity of the leading bubble or even coalesce [78]. As gas holdup rises, swarm velocity increases and decreases again after reaching a maximum [25]. In contrast, researchers also state that a single bubble moves slower up to a gas holdup of about 15 percent while above that bubble swarms are slower [122].

For practical reasons in simulation, bubble swarms with different bubble classes have to be summarized to account for effects such as drag and mass transfer. If bubble classes are to be represented as one single class, the Sauter mean diameter represents a class where the ratio of surface to volume is kept constant.

Sriram and Mann [129] proposed the dynamic disengagement technique for simple characterization of bubble size distributions. Gas supply is instantaneously interrupted and the liquid operation level is measured in the following as function of time.

Since gas is generally supplied from the reactor bottom, the disengagement process also starts from the bottom [119]. Large bubbles rise faster than small ones such that large bubble fractions tend to leave the reactor

first. As a result, operation level does not linearly decrease with time. Large fractions cause a steeper decrease at the beginning.

In this work a single size class with the bubble diameter of 0.005 m has been used for pure fluid dynamics simulation. Combined simulations of fluid dynamics and mass transfer have been performed using three classes with diameters 0.0008 m, 0.003 m and 0.08 m experimentally determined by dynamic disengagement. These classes are assumed to be capable to sufficiently account for all relevant effects.

2.6 Interface Momentum Transfer

Research on drag coefficients of differently shaped bubbles in many liquid constellations has been done. There is still no commonly applicable and generally accepted drag formulation. The formulation used seems to be best practice in the relevant range of parameters [122].

The continuous phase α interacts with all dispersed phases β. Momentum is transferred between the phases. In equations 2.11 to 2.13 mass transfer is accounted for by the M_α terms. Using the Kronecker delta $\delta_{\alpha\beta}$, equation 2.14 defines the sum of momentum transferred to phase α.

$$M_\alpha = \sum_\beta M_{\alpha\beta}(1 - \delta_{\alpha\beta}) \tag{2.14}$$

$M_{\alpha\beta}$ generally consists of terms related to every acting force such as drag, lift, virtual mass and turbulent dispersion force. Since drag force has major impact and sufficiently validated terms, it is the only force considered. Drag force is represented by the term $M_{\alpha\beta}$ here.

Bubble drag force for a single bubble follows.

$$D_{p\beta} = \frac{\varrho_\alpha}{2} c_{D\beta} \left(\underline{u}_\beta - \underline{u}_\alpha\right)^2 A_\beta \tag{2.15}$$

ϱ_α is the continuous phase density, $c_{D\beta}$ the drag coefficient, the term in brackets of equation 2.15 the slip velocity and A_β the projected area of a bubble in flow direction. The overall interface drag is the product of the

number of dispersed bubbles $n_{p\beta}$ and the drag for a single bubble $D_{p\beta}$.

$$M_{\alpha\beta} = n_{p\beta} D_{p\beta} \tag{2.16}$$

$$n_{p\beta} = \frac{6 r_\beta}{\pi d_\beta^3} \tag{2.17}$$

$$A_\beta = \frac{\pi d_\beta^2}{4} \tag{2.18}$$

Hence, equation 2.19 gives the interface momentum transfer from dispersed phase β to continuous phase α.

$$M_{\alpha\beta} = \frac{3}{4} \frac{c_{D\beta}}{d_\beta} r_\beta \varrho_\alpha \left| \underline{u}_\beta - \underline{u}_\alpha \right| \left(\underline{u}_\beta - \underline{u}_\alpha \right) \tag{2.19}$$

The definition of the drag coefficient and the bubble diameter from equation 2.19 for every single dispersed phase β is the challenge of modeling multiphase flow. As mentioned earlier in section 2.5 the behavior greatly changes with size and dispersed phase holdup. A great number of mostly empirical equations for drag coefficients exists. The dispersed phase Reynolds number is part of most definitions.

$$\mathrm{Re}_\beta = \frac{d_\beta \varrho_\alpha \left| \underline{u}_\beta - \underline{u}_\alpha \right|}{\eta_\alpha} \tag{2.20}$$

The drag coefficient for a single bubble depends upon the bubble size and shape. The decision about the drag coefficient of a single bubble $c_{D\beta\infty}$ is implemented as follows.

$$c_{D\beta\infty} = \max(c_{D\beta\infty,sphere}, \min(c_{D\beta\infty,ellipsoid}, c_{D\beta\infty,cap})) \tag{2.21}$$

For a spherical bubble a correlation proposed by Schiller and Naumann in 1933 is used [23].

$$c_{D\beta\infty,sphere} = \frac{24}{\mathrm{Re}_\beta} \left(1 + 0.15 \mathrm{Re}_\beta^{0.687} \right) \tag{2.22}$$

Bubble drag coefficients for bubbles of ellipsoidal shape are calculated from the Grace drag model [37]. This model performs especially well for air bubbles in aqueous solutions.

$$c_{D\beta\infty,ellipsoid} = \frac{4}{3} \frac{g d_\beta}{u_t^2} \frac{\varrho_\alpha - \varrho_\beta}{\varrho_\alpha} \tag{2.23}$$

Where g is the gravitational acceleration, d_β the equivalent diameter of a sphere of same volume and u_t is the terminal velocity:

$$u_t = \frac{\eta_\alpha}{\varrho_\alpha d_\beta} \mathrm{Mo}^{-0.149} (J - 0.857) \tag{2.24}$$

The Morton number Mo, the Eötvös number Eo

$$\mathrm{Mo} = \frac{\eta_\alpha^4 g(\varrho_\alpha - \varrho_\beta)}{\varrho_\alpha \sigma^3} \tag{2.25}$$

$$\mathrm{Eo} = \frac{g(\varrho_\alpha - \varrho_\beta) d_\beta^2}{\sigma} \tag{2.26}$$

and the following terms are necessary to calculate drag coefficients with equation 2.23:

$$J = \begin{cases} 0.94 H^{0.751} & 2 < H \leq 59.3 \\ 3.42 H^{0.441} & H > 59.3 \end{cases} \tag{2.27}$$

$$H = \frac{4}{3} \mathrm{EoMo}^{-0.149} \left(\frac{\eta_\alpha}{\eta_{ref}} \right)^{-0.14} \tag{2.28}$$

$$\eta_{ref} = 0.0009 \frac{\mathrm{kg}}{\mathrm{s\,m}} \tag{2.29}$$

The drag coefficient for bubbles in the cap regime is constant [37].

$$c_{D\beta\infty,cap} = \frac{8}{3} \tag{2.30}$$

Large bubbles tend to pull other bubbles into their wakes and increase their velocity. Obviously, the effect is related to local dispersed phase holdup. In order to account for such effects a correction factor $f_{c_{D\beta\infty}}$ [15] with $n = 2$ is used for all drag coefficients.

$$f_{c_{D\beta\infty}} = (1 - r_\beta)^n \tag{2.31}$$

Hence, equation 2.32 defines the corrected drag coefficient $c_{D\beta}$.

$$c_{D\beta} = f_{c_{D\beta\infty}} c_{D\beta\infty} \tag{2.32}$$

2.7 Turbulence Model

Turbulence is one of the last great problems in classical physics. The Clay Mathematics Institute mentions turbulence as one of the millennium problems. Turbulence effects have a great impact on fluid flow as well as on other regarded effects such as mass transfer. One of the most commonly applied turbulence models in multiphase flow is the k-ε model. k is the turbulence kinetic energy and ε the turbulent energy dissipation rate. Even though it is known to poorly perform in swirling flows, it shows good performance for many industrially relevant systems [143]. For general information about turbulence models it is referred to the corresponding literature.

The averaging process in section 2.4 was necessary to get a set of equations for calculation of practical problems. Unfortunately, the set of equations is not closed for averaging has caused additional unknown terms called Reynolds stresses. Analogous to the definition of the Newtonian stresses, the Reynolds stresses are defined via the eddy viscosity $\eta_{\alpha t}$. It remains to give a physically motivated definition of the eddy viscosity. This is known as the Boussinesq approximation [65]. Even though $\eta_{\alpha t}$ is called viscosity, it is not to be mistaken as the physical molecular viscosity. As a consequence of the Boussinesq approximation, the effective viscosity is the sum of molecular and eddy viscosity.

$$\eta_{\alpha eff} = \eta_\alpha + \eta_{\alpha t} \tag{2.33}$$

Beside many different approaches, the k-ε model is one of the two equation eddy viscosity models. It uses two partial differential equations for both, the turbulent kinetic energy k_α and the energy dissipation rate ε_α. First, the eddy viscosity $\eta_{\alpha t}$ reads [143].

$$\eta_{\alpha t} = \varrho_\alpha C_\mu \frac{k_\alpha^2}{\varepsilon_\alpha} \tag{2.34}$$

The transport equations for k_α and ε_α are defined:

$$\begin{aligned} \frac{\partial(\varrho_\alpha k_\alpha)}{\partial t} + \frac{\partial(\varrho_\alpha k_\alpha U_\alpha)}{\partial x} + \frac{\partial(\varrho_\alpha k_\alpha V_\alpha)}{\partial y} + \frac{\partial(\varrho_\alpha k_\alpha W_\alpha)}{\partial z} = \\ P_\alpha - \varrho_\alpha \varepsilon_\alpha + T_{\alpha\beta k} + \frac{\partial}{\partial x}\left[\left(\eta_\alpha + \frac{\eta_{\alpha t}}{\sigma_{k_\alpha}}\right)\frac{\partial k_\alpha}{\partial x}\right] + \\ \frac{\partial}{\partial y}\left[\left(\eta_\alpha + \frac{\eta_{\alpha t}}{\sigma_{k_\alpha}}\right)\frac{\partial k_\alpha}{\partial y}\right] + \frac{\partial}{\partial z}\left[\left(\eta_\alpha + \frac{\eta_{\alpha t}}{\sigma_{k_\alpha}}\right)\frac{\partial k_\alpha}{\partial z}\right] \end{aligned} \tag{2.35}$$

$$\frac{\partial(\varrho_\alpha\varepsilon_\alpha)}{\partial t}+\frac{\partial(\varrho_\alpha\varepsilon_\alpha U_\alpha)}{\partial x}+\frac{\partial(\varrho_\alpha\varepsilon_\alpha V_\alpha)}{\partial y}+\frac{\partial(\varrho_\alpha\varepsilon_\alpha W_\alpha)}{\partial z}=$$
$$C_{\varepsilon 1}\varrho_\alpha\frac{\varepsilon_\alpha}{k_\alpha}P_\alpha-C_{\varepsilon 2}\varrho_\alpha\frac{\varepsilon_\alpha^2}{k_\alpha}+T_{\alpha\beta\varepsilon}+\frac{\partial}{\partial x}\left[\left(\eta_\alpha+\frac{\eta_{\alpha t}}{\sigma_{\varepsilon_\alpha}}\right)\frac{\partial\varepsilon_\alpha}{\partial x}\right]+$$
$$\frac{\partial}{\partial y}\left[\left(\eta_\alpha+\frac{\eta_{\alpha t}}{\sigma_{\varepsilon_\alpha}}\right)\frac{\partial\varepsilon_\alpha}{\partial y}\right]+\frac{\partial}{\partial z}\left[\left(\eta_\alpha+\frac{\eta_{\alpha t}}{\sigma_{\varepsilon_\alpha}}\right)\frac{\partial\varepsilon_\alpha}{\partial z}\right] \tag{2.36}$$

P_α is the turbulence production term [65].

$$P_\alpha=-\varrho_\alpha\left[\left(\overline{u_\alpha'^2}\frac{\partial U_\alpha}{\partial x}+\overline{u_\alpha'v_\alpha'}\frac{\partial V_\alpha}{\partial x}+\overline{u_\alpha'w_\alpha'}\frac{\partial W_\alpha}{\partial x}\right)+\right.$$
$$\left(\overline{u_\alpha'v_\alpha'}\frac{\partial U_\alpha}{\partial y}+\overline{v_\alpha'^2}\frac{\partial V_\alpha}{\partial y}+\overline{v_\alpha'w_\alpha'}\frac{\partial W_\alpha}{\partial y}\right)+$$
$$\left.\left(\overline{u_\alpha'w_\alpha'}\frac{\partial U_\alpha}{\partial z}+\overline{v_\alpha'w_\alpha'}\frac{\partial V_\alpha}{\partial z}+\overline{w_\alpha'^2}\frac{\partial W_\alpha}{\partial z}\right)\right] \tag{2.37}$$

Turbulent kinetic energy k_α is defined as the kinetic energy due to turbulent motion [143]:

$$k_\alpha=\frac{1}{2}\left(\overline{u_\alpha'^2+v_\alpha'^2+w_\alpha'^2}\right) \tag{2.38}$$

The energy dissipation rate ε_α is defined as follows [65].

$$\varepsilon_\alpha=\frac{\eta_\alpha}{\varrho_\alpha}\left[\overline{\left(\frac{\partial u_\alpha'}{\partial x}\right)^2}+\overline{\left(\frac{\partial v_\alpha'}{\partial y}\right)^2}+\overline{\left(\frac{\partial w_\alpha'}{\partial z}\right)^2}+\right.$$
$$\overline{\left(\frac{\partial u_\alpha'}{\partial y}+\frac{\partial v_\alpha'}{\partial x}\right)^2}+\overline{\left(\frac{\partial u_\alpha'}{\partial z}+\frac{\partial w_\alpha'}{\partial x}\right)^2}+\left.\overline{\left(\frac{\partial v_\alpha'}{\partial z}+\frac{\partial w_\alpha'}{\partial y}\right)^2}\right]-$$
$$2\frac{\eta_\alpha}{\varrho_\alpha}\left(\overline{\frac{\partial u_\alpha'}{\partial y}\frac{\partial v_\alpha'}{\partial x}}+\overline{\frac{\partial v_\alpha'}{\partial z}\frac{\partial w_\alpha'}{\partial y}}+\overline{\frac{\partial w_\alpha'}{\partial x}\frac{\partial u_\alpha'}{\partial z}}\right) \tag{2.39}$$

Model constants of the standard k-ε model are listed in **table 2.1**.

The k-ε model has been used for modeling the turbulence of the continuous phase. As mentioned above, the dispersed phase has a significant influence on the continuous phase motion. This also holds true for the continuous phase turbulence. Thus, the terms $T_{\alpha\beta k}$ and $T_{\alpha\beta\varepsilon}$ in equations 2.35 and 2.36 respectively represent interphase transfer of k_α and ε_α. In terms of

Table 2.1: Model constants of the standard k-ε model [143]

C_μ	σ_{k_α}	$\sigma_{\varepsilon_\alpha}$	$C_{\varepsilon 1}$	$C_{\varepsilon 2}$
0.09	1	1.3	1.44	1.92

gas bubbles as dispersed phase in liquid, the effect is referred to as bubble induced turbulence [114].

There are different approaches to account for bubble induced turbulence. In 1975, Sato and Sekoguchi [114] proposed to represent the portion of bubble induced turbulence as a summand $\eta_{t,bit}$ in equation 2.33.

$$\eta_{t,bit} = k_1 \frac{d_\beta}{2} r_\alpha \varrho_\alpha |\underline{u}_\alpha - \underline{u}_\beta| \tag{2.40}$$

From experiments, k_1 has been determined having the value 1.2 [112].

A second type of model describes additional terms for the stress tensor assuming linear superposition. The approach has been proposed by Arnold in 1988 and is similar to an approach by Lopez de Bertodano [126].

These two models underestimate bubble induced turbulence significantly [126, 152]. Turbulence as a transported variable can exist quite a time downstream. Thus, a third type of model has been developed accounting for transport of the turbulent kinetic energy k as well as for the energy dissipation rate ε. By drag, deformation and wake bubbles may increase turbulence but also the deformable surface may decrease turbulence by dissipation. Such bubble or drag induced turbulence terms have been proposed by Kataoka and Serizawa [71]. Similar models exist, differing in the time scale of the bubble induced turbulence [134].

Here, the description of Pfleger and Becker [105] has been implemented using $C_k = C_{\varepsilon 1}$ and $C_{\varepsilon 3} = C_{\varepsilon 2}$ (table 2.1). The $T_{\alpha\beta k}$-term has been proposed by Bel F'Dhila and Simomin in 1992 and the $T_{\alpha\beta\varepsilon}$-term by Elgobashi and Abou-Arab in 1983 [94].

$$T_{\alpha\beta k} = r_\alpha C_k \left|M_{\alpha\beta}\right| |\underline{u}_\alpha - \underline{u}_\beta| \tag{2.41}$$

$$T_{\alpha\beta\varepsilon} = C_{\varepsilon 3} \frac{\varepsilon}{k} T_{\alpha\beta k} = C_{\varepsilon 3} \frac{\varepsilon}{k} r_\alpha C_k \left|M_{\alpha\beta}\right| |\underline{u}_\alpha - \underline{u}_\beta| \tag{2.42}$$

The approach by Pfleger and Becker [105] has been reported to perform best [152]. Nevertheless, it only accounts for drag related turbulence production and dissipation. As a matter of fact, all forces related to the phase boundary have their share. Existing models can only be the beginning [101]. It has already been reported, that $C_{\varepsilon 3}$ in equation 2.42 is likely to not being constant but a function of bubble diameter and dispersed phase holdup [84].

Turbulence of the dispersed phase is modeled using the dispersed phase zero equation model. The dispersed phase effective viscosity is calculated following equation 2.33. The dispersed phase eddy viscosity $\eta_{\beta t}$ is defined as:

$$\eta_{\beta t} = \frac{\varrho_\beta}{\varrho_\alpha} \eta_{\alpha t} \tag{2.43}$$

Equation 2.43 becomes negligible for dispersed phase densities much less than the continuous phase density.

2.8 Mass Transfer

Sufficiently supporting cells with oxygen is of major interest in baker's yeast production. A lack of oxygen leads to ethanol production, reduced biomass yield and quality.

Driving force for mass transfer by diffusion is the concentration difference of adjacent phases. Mass transfer can be hindered by boundary layers. Within the layer, concentration differences of adjacent boundaries are balanced by the gradient [116]. For oxygen mass transfer from air into an aqueous phase or vice versa resistance on the liquid side significantly exceeds resistance on the gaseous side. Thus, only liquid side mass transfer resistance has to be considered. This still holds true in case of sinks in the gas phase for relatively slow reactions such as biological growth. The mass flow rate is given by $\Gamma_{\alpha\beta}$.

$$\Gamma_{\alpha\beta} = k_L a_{\alpha\beta} (c^*_\alpha - c_\alpha) \tag{2.44}$$

k_L is the mass transfer coefficient, c^*_α the liquid side saturation concentration for a given temperature and pressure and c_α the actual liquid side mass concentration. $a_{\alpha\beta}$ is the volume specific interphase area also called interphase area density. The sign convention in equation 2.44 assumes the mass transfer to occur from dispersed to continuous phase.

Assuming spherical equal sized bubbles for each class, the volume specific surface area $a_{\alpha\beta}$ for more than one class is given as the sum over the individual

volume specific surface areas $a_{\alpha\beta i}$. Equation 2.45 is written for three classes.

$$a_{\alpha\beta} = \sum_{i=1}^{3} a_{\alpha\beta i} = 6 \sum_{i=1}^{3} \frac{r^*_{\beta i}}{d_{\beta,i}} \tag{2.45}$$

$r^*_{\beta i}$ is the local volume fraction of class i. The oxygen concentration in the liquid is an additional transport variable in CFX. Obviously, $a_{\alpha\beta}$ is a local measure but can also be determined for the overall reaction volume. In literature $k_L a_{\alpha\beta}$ is often treated as one variable referred to as volumetric mass transfer coefficient.

For the mass transfer coefficient k_L different approaches are given in literature, some of them accounting for turbulence effects (equations 2.47 and 2.48).

$$k_L = 3.1 \cdot 10^{-4} \frac{\mathrm{m}}{\mathrm{s}} \qquad \text{Hallensleben [63]} \tag{2.46}$$

$$k_L = 2\sqrt{\frac{D_\alpha}{\pi}} \sqrt[4]{\frac{\varepsilon \varrho_\alpha}{\eta_\alpha}} \qquad \text{Garcia-Ochoa and Gomez [58]} \tag{2.47}$$

$$k_L = \frac{2}{\sqrt{\pi}} \left(\frac{D_{\alpha\varrho_\alpha}}{\eta_\alpha} \right)^{\frac{2}{3}} \sqrt[4]{\frac{\eta_\alpha \varepsilon}{\varrho_\alpha}} \qquad \text{Schütze [121]} \tag{2.48}$$

Interphase area density has been reported to have much more influence on overall mass transfer than turbulence related to values calculated from equations 2.47 and 2.48. At the same time uncertainties arise from the turbulence model. Therefore, the constant value from equation 2.46 is applied.

Surface active agents are well known to significantly influence mass transfer. A surface coverage ratio is defined for description of surfactant related effects. Generally, the mass transfer coefficient decreases with increasing coverage ratio [111]. The mass transfer coefficient has been reported as being one fourth to one sixth for bubbles contaminated with surfactants such as dust particles or surface active molecules [2]. A surfactant concentration above a critical micelle concentration or accordingly above a critical coverage ratio does not further decrease mass transfer [103].

Mass transfer coefficient for bubbles smaller than 1.5 mm is solely influenced by bubble geometry and ranges around $1 \cdot 10^{-4} \frac{\mathrm{m}}{\mathrm{s}}$. For bubbles in the range from 1.5 mm to 3.5 mm k_L ranges between $1 \cdot 10^{-4} \frac{\mathrm{m}}{\mathrm{s}}$ and $4 \cdot 10^{-4} \frac{\mathrm{m}}{\mathrm{s}}$. It is influenced by the physico-chemical characteristics of the surfactants and

bubble geometry. Mass transfer coefficients increase from liquids with non-ionic surfactants over cationic and anionic surfactants to pure liquids. For bubbles above 3.5 mm in diameter, mass transfer does not depend upon bubble geometry. The coefficient then ranges about $4 \cdot 10^{-4} \frac{\mathrm{m}}{\mathrm{s}}$ [111].

Electrolyte solutions show similar effects and can be seen as a subcase of solutions with surfactants. With increasing concentration of electrolytes, k_L decreases [42, 64]. It has to be mentioned that electrolytes may hinder coalescence and increase surface area density. As a result, overall mass transfer may behave contrary. Compared to mass transfer in water, mass transfer in solutions containing molasses is reduced [42]. This is especially important for industrial yeast production.

Not only surface active agents but also biological cells can accumulate at gas liquid interphase. It has been reported that the rear stagnant point is a preferred location due to the bubble wake structure. Accumulation of cells may result in additionally reduced oxygen mass transfer [3].

Vibration excitement has been reported as an interesting method to enhance mass transfer [51]. Excitement of the homogeneous phase in the frequency range between 40 Hz to 100 Hz causes bubble size reduction of up to 50%. This increases gas holdup as well as higher amplitudes do. With increasing gas holdup also overall mass transfer increases. Additionally, the mass transfer coefficient is enhanced probably due to a higher level of turbulence at gas liquid interphase [51]. In a similar manner mass transfer has been reported as decreasing with increasing column height due to elevated turbulence level in the region of bubble generation [42].

The saturation concentration of oxygen in water is subject to oxygen partial pressure in the adjacent dispersed phase for a given temperature. Equation 2.49 gives the saturation concentration [99].

$$c_\alpha^* = \frac{p_\beta^\infty - \gamma p'_\alpha}{p_N} X_{\beta,O_2} \alpha_B \frac{M_{O_2}}{V_M} \tag{2.49}$$

with p_β^∞ as ambient pressure, γ the relative humidity of air [99], p'_α as saturation vapor pressure of water at a given temperature, the normal pressure p_N, the oxygen mole fraction in dry air X_{β,O_2}, α_B the Bunsen absorption coefficient, M_{O_2} as molecular weight of oxygen and the mole volume V_M of an ideal gas at ambient conditions.

The relationship between continuous and dispersed phase concentration at equilibrium is often referred to as Bunsen, Raoult or Henry relationship.

Equation 2.49 can be rewritten defining a Henry coefficient H_{m,O_2} [128, 99].

$$c^*_\alpha = (p^\infty_\beta - \gamma p'_\alpha) X_{\beta,O_2} H_{m,O_2} \tag{2.50}$$

Following Dalton's law, partial pressure of ideal gases is calculated from equation 2.51 with the fraction $X_{\beta,i}$ of component i [99].

$$p^\infty_{\beta,i} = X_{\beta,i} p^\infty_\beta \tag{2.51}$$

$$X_{\beta,i} = \frac{V_{\beta,i}}{V_\beta} \tag{2.52}$$

Saturation concentrations calculated from equation 2.50 for air and pure oxygen coincide with literature data [128, 4]. A description as given by equation 2.51 using the partial pressure of the transferred component has the great advantage of being general.

The following parameters are used for implementation of oxygen transfer following equation 2.49 or 2.50.

$$\alpha_B = 2.844 \cdot 10^{-2} \quad (298.15K) \quad [99] \tag{2.53}$$

$$V_M = 2.2414 \cdot 10^{-2} \, \frac{\mathrm{m}^3}{\mathrm{mol}} \tag{2.54}$$

$$p_N = 101325 \, \frac{\mathrm{kg}}{\mathrm{s}^2\mathrm{m}} \tag{2.55}$$

$$M_{O_2} = 3.198 \cdot 10^{-2} \, \frac{\mathrm{kg}}{\mathrm{mol}} \tag{2.56}$$

The partial pressure of oxygen in the transported dispersed phase depends upon the current oxygen concentration. p^∞_{β,O_2} is the partial pressure of oxygen in air.

$$p^\infty_{\beta,O_2} = X_{\beta,O_2}(p^\infty_\beta - \gamma p'_\alpha) \tag{2.57}$$

$$X_{\beta,O_2} = \frac{n_{\beta,O_2}}{n_\beta} = \frac{n_{\beta,O_2}}{n_{\beta,0} - \Delta n_{\beta,O_2}} = \frac{n_{\beta,O_2}}{n_{\beta,0} - (n_{\beta,O_2,0} - n_{\beta,O_2})}$$

$$= \frac{n_{\beta,O_2}}{n_{\beta,0} - n_{\beta,O_2,0} + n_{\beta,O_2}} \tag{2.58}$$

$$n_{\beta,O_2} = \frac{\sum_{i=1}^{3} c_{\beta,O_2,i} \cdot r_{\beta i}}{M_{O_2} \sum_{i=1}^{3} r_{\beta i}} \tag{2.59}$$

The actual oxygen concentration in the continuous c_{α,O_2} and the dispersed phases c_{β,O_2} are taken from the transport equations of the simulation. Index

addition 0 signalizes initial conditions. Concluding, unknown terms from equations 2.57 to 2.59 are given.

$$n_{\beta,0} = 44.615\,\frac{\mathrm{mol}}{\mathrm{m}^3} \tag{2.60}$$

$$n_{\beta,O_2,0} = 9.3468\,\frac{\mathrm{mol}}{\mathrm{m}^3} \tag{2.61}$$

$$\gamma = 1 \tag{2.62}$$

$$p'_\alpha = 3170\,\frac{\mathrm{kg}}{\mathrm{s}^2\mathrm{m}} \tag{2.63}$$

The calculated mass flow is the source term for oxygen in water. The flow has to be proportionately distributed on the gas side as sink for each bubble class. The mass transfer coefficient is taken to be constant independently of the individual bubble size. For distribution then the relevant factor is the ratio of the volume specific surface area of class $a_{\alpha\beta i}$ to the overall specific surface area $a_{\alpha\beta}$.

$$\dot{m}_{\beta,i} = \Gamma_{\alpha\beta}\frac{a_{\alpha\beta i}}{a_{\alpha\beta}} \tag{2.64}$$

Oxygen consumption due to yeast growth is represented by an oxygen sink term $\dot{m}_{Y,O_2}$. The yeast is assumed to be equally distributed wherefore the sink is supposed to be constant in the entire domain. The oxygen sink cannot be negative.

$$\dot{m}_{Y,O_2} = \max\left(0, \min\left(\frac{c_{\alpha,O_2}}{\Delta t}, \dot{m}_{Y,Matlab}\right)\right) \tag{2.65}$$

Assuming carbon dioxide from yeast cultivation being transferred from the continuous to the dispersed phase, volume change due to mass transfer is not considered. The effect of simultaneously transferred oxygen and carbon dioxide has been studied [63] but is neglected as aforesaid. Mass transfer is assumed not to influence fluid dynamics. Another assumption in simulation has been to neglect temperature dependence of mass transfer coefficients.

2.9 System, Geometry and Simplifications

The bubble column reactor shown in **figure 2.1** is a circular tube. Its inner diameter is 390 mm and the overall height 2040 mm. Seven fittings are installed at one side of the reactor spanning the $x = 0$ plane. Fittings are

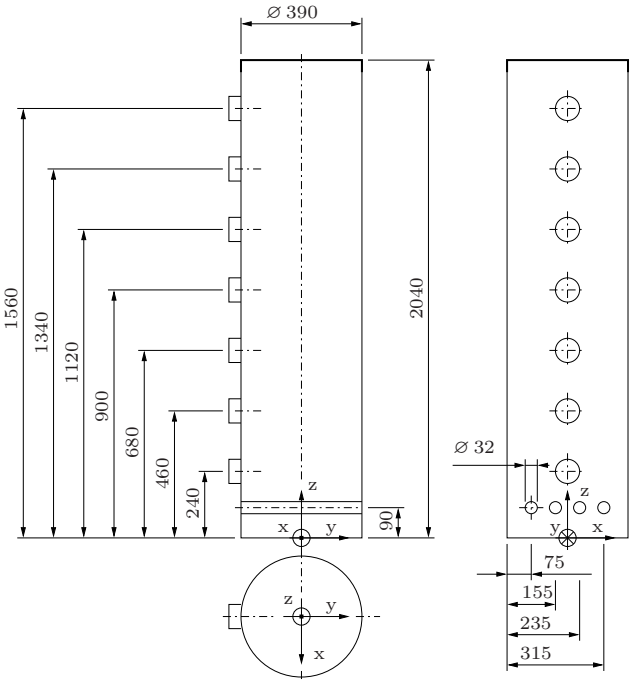

Figure 2.1: Reactor geometry, measures in mm

used for measurement probes as well as for different in- and outlets. To reduce the impact on the flow field, a flat plate separates the reactor volume and the cavities of the fittings. A lid closes the reactor at its top including an exhaust gas line.

Four jet tubes with 676 holes in total of 0.8 mm diameter on the upper side are used as static gassing system. The holes are arranged in five lines on every tube with an inter hole distance of 8 mm (**figure 2.2**). Thus, the holes build up a regular structure of equilateral triangles. Jet tubes as gassing system have been chosen because of the relation to commonly used industrial systems.

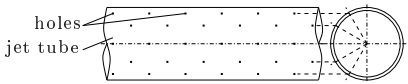

Figure 2.2: Jet tube as detail of the gassing system

A projected annulus region at the cylinder jacket of 30 mm width is designated ungassed area on the jet tubes. The near wall region is expected to be down-flow region. Down coming liquid and rising gas bubbles would work against the liquid circulation reducing the wanted effects and consuming additional energy. For practical reasons, in simulations the holes are represented in terms of an area fraction of the related enveloping surface.

In contrast to large industrial gassing systems gas is supplied only from one side of the jet tubes. Since the jet tube to hole diameter ratio is great, the pressure drop for gas entering the bubble column through the holes exceeds the pressure drop resulting from drag inside the tubes by far. As a consequence, the system accomplishes homogeneous gassing. The gas flow rate is $14.5\,\frac{\mathrm{m}^3}{\mathrm{h}}$ and corresponds to the superficial gas velocity of $0.034\,\frac{\mathrm{m}}{\mathrm{s}}$.

Jet tubes and fittings are made of polyvenylchloride. Medium and alkaline solution are fed through tubes with an inner diameter of 8 mm. The tubes enter the reactor via fittings positioned in a way that injected liquids enter the reactor in radial direction.

The operation level is defined as the filling level under gassed condition. Velocity measurements for validation reasons have been taken with an operation level of 1.8 m. The operation level during cultivation experiments varies between about 1.08 m and 1.22 m due to medium feed. For the sequential co-simulation run the operation level depends upon the calculated volume of the preceding step.

Even though the real system has a free surface, simulations have been performed with a plane surface given by $z = \text{const.}$. For detailed information about the appropriate boundary conditions it is referred to section 2.11. This representation is especially sufficient for systems with relatively low gas flow rates. Simulations with free surfaces significantly increase computational cost, in this case without additional valuable information. The reactor system and the equipment are schematically shown in figure 5.1.

Test simulations have not shown significant influence of measuring devices and the cooling circuit on flow characteristics. Therefore, simulations have been performed without. The cooling circuit has only been installed for security reasons to cool down the cultivation volume in case of rapidly increasing temperature. In fact, the reaction volume has neither been cooled nor heated during cultivation experiments. The supplied air flow caused almost constant temperature levels. Hence, the simulation setup is reduced to a simple constellation.

2.10 Mesh

There are two principle types of a volume mesh, either a structured or an unstructured mesh. Structured meshes consist of hexahedrons while the majority of unstructured meshes consist of tetrahedrons. Where applicable, structured meshes improve efficiency of calculations. Moreover, structured meshes have a higher node density providing better results for a comparable number of elements.

For complex geometries it is sometimes very difficult or even impossible to come up with an adequate fully structured mesh. Unstructured meshes are easily and quickly generated. Both mesh types can also be connected. The combination makes use of the advantages of both mesh types, being quickly generated and providing good results. Meshes used in this work have been generated with Icem CFD 11.0.

Even though the geometry shown in figure 2.1 does not appear to be complex, the intersection of the jet tubes and the reactor wall does not allow the use of a fully structured mesh. For the major fraction of the reactor, obviously a structured mesh is the best choice. The mesh above $z = 180\,\text{mm}$ have been built from hexahedrons while the bottom part in the z-range from 0 to 180 mm has been meshed with tetrahedrons. **Figure 2.3** on the left shows the unstructured mesh on the plane $z = 90\,\text{mm}$. Jet tubes are positioned at the white stripes. In **figure 2.3** on the right a cross section of the structured mesh on plane $z = 500\,\text{mm}$ is shown.

Well behaving simulations are often based upon high quality meshes. The quality has been checked with respect to the element aspect ratio in case of the unstructured mesh and with respect to the minimum angle in case of the structured mesh. The minimum aspect ratio has been forced to be above 0.4 while the minimum angle has been forced to exceed 30 °. Element size

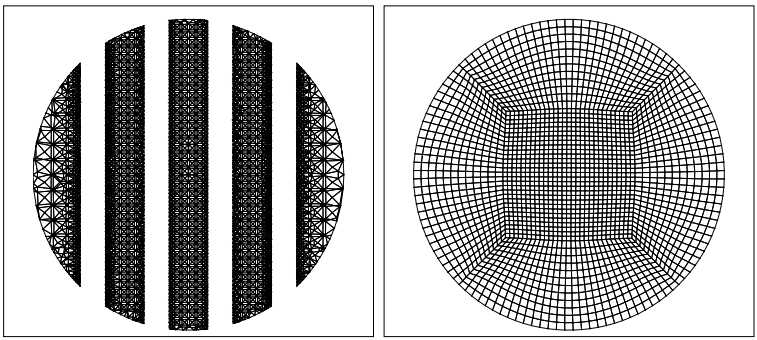

Figure 2.3: Unstructured mesh on plane $z = 90\,\text{mm}$ (left) and structured mesh on plane $z = 500\,\text{mm}$ (right)

has to be adopted to the physical problem. Hence, simulations cannot give physically correct results in scales not being resolved by the mesh. Effects based upon smaller scales can at maximum be as good as the related models are.

A mesh convergency study has been performed to assure that results calculated on a certain mesh are independent from the mesh. The mesh has been refined using half the mesh spacing in every direction resulting in about eight times the number of elements. The mesh has also been coarsened by doubling the element size ending up with about one eighth of the number of elements. Characteristic properties of the results must not differ more than 20 percent from the results of the next coarser mesh. Results from the coarse mesh shall differ more from results calculated on the medium mesh than those performed on the fine mesh do. For results behaving in such a way, simulations are performed on the medium mesh (section 3.4).

Table 2.2 names the maximum allowed element size for the coarse, the medium and the fine mesh.

In the same manner, for transient simulations a time step convergency study has been performed using the medium mesh. Results as shown in section 3.4 do not vary significantly depending on time step variations. The medium time step has been used for regular simulations. For the combination of time step and mesh size the Courant-Friedrichs-Lewy (CFL) condition in

Table 2.2: Maximum allowed element size on defined mesh areas in mm

mesh area	coarse, Δx_c	medium, Δx_m	fine, Δx_f
inlet	10	5	2.5
interface unstructured	20	10	5
interface structured	14	7	3.5
jet tube wall	16	8	4
top	14	7	3.5
wall structured	20	10	5
wall unstructured	40	20	10

equation 2.66 has to be kept where u stands for the velocity magnitude, Δt for the time step and Δx for the element size [38, 143, 131].

$$CFL = \frac{u \cdot \Delta t}{\Delta x} \overset{!}{<} 1 \tag{2.66}$$

The CFL number relates the distance an infinitesimally small fluid element moving with velocity u covers in the time Δt with the element size Δx. The condition ensures that no infinitesimally small fluid element covers more than one element length per time step which would entail physically invalid results. The CFL condition is sufficiently met using the medium time step.

2.11 Simulation Conditions

The multiphase flow is modeled using the Euler-Euler approach. For simplicity the number of fluids used depends upon the simulation type. Gravitational acceleration $g = 9.81\,\frac{\mathrm{m}}{\mathrm{s}^2}$ acts in negative z-direction.

The first fluid is based on CFX's template for water. Cultivation broths of yeast production are similar to watery systems except for the surface tension. Since density and viscosity do not significantly change during yeast cultivations these values are assumed to be constant, namely $\varrho_\alpha = 997\,\frac{\mathrm{kg}}{\mathrm{m}^3}$ and $\eta_\alpha = 8.899 \cdot 10^{-4}\,\frac{\mathrm{kg}}{\mathrm{sm}}$. The surface tension coefficient varies almost linearly between $\sigma = 0.0735\,\frac{\mathrm{kg}}{\mathrm{s}^2}$ and $\sigma = 0.04\,\frac{\mathrm{kg}}{\mathrm{s}^2}$. Surface tension coefficient has

been set to $\sigma = 0.0735\,\frac{\mathrm{kg}}{\mathrm{s}^2}$ at the beginning, to $\sigma = 0.057\,\frac{\mathrm{kg}}{\mathrm{s}^2}$ after six hours and to $\sigma = 0.04\,\frac{\mathrm{kg}}{\mathrm{s}^2}$ for cultivation times after 12 hours.

For simple fluid dynamics simulations, there is only one gas phase with the mean bubble diameter $d_\beta = 5\,\mathrm{mm}$. For sequential co-simulations, the gas phase is divided into three classes differing in bubble size. Every class is assumed to consist of equally sized bubbles. The characteristics are similar to the CFX template for air. The most important difference between the classes is their distinct mean diameter, $d_{\beta,1} = 0.08\,\mathrm{m}$, $d_{\beta,2} = 0.003\,\mathrm{m}$ and $d_{\beta,3} = 0.0008\,\mathrm{m}$. The drag coefficient $c_{D\beta,i}$ is calculated using the Grace drag model implemented in CFX with a volume fraction correction exponent of 2 (equations 2.21 to 2.32) [37]. This exponent accounts for bubble-bubble interaction especially at higher gas holdup.

In contrast to the template, the air density is a function of axial position depending on the operation level and the overall volume mixture composition. For simplification, it is assumed that the volume fraction of all components is constant. Air density ϱ_β is implemented following equation 2.68.

$$\varrho_\beta = \frac{(p_\beta^\infty + (\varrho_\alpha(1-r_\beta) + \varrho_\beta r_\beta)}{RT_\beta} g(H_r - z))M_\beta \tag{2.67}$$

$$\Longleftrightarrow \quad \varrho_\beta = \frac{(p_\beta^\infty + \varrho_\alpha(1-r_\beta)g(H_r - z))M_\beta}{RT_\beta - r_\beta g(H_r - z)M_\beta} \tag{2.68}$$

Here, r_β is the sum over the individual gas volume fractions $r_{\beta i}$ and z the coordinate in axial direction starting at the cylinder bottom.

Simple fluid dynamics simulations do not require the definitions of additional variables. For combined simulations of fluid dynamics and biological growth, transport equations for oxygen, yeast, ethanol and glucose are defined. In order to reduce the number of equations, the additional variables are defined only in relevant phases. Oxygen obviously is defined in gas and liquid while all other variables are defined in the liquid phase only.

A sub-domain is defined in CFX for declaration of these additional variables and the source terms related to bubble induced turbulence. Diffusion coefficients in the liquid and the gas are defined for calculation of oxygen transport [52, 41, 150, 73].

$$D_\alpha = 2.45 \cdot 10^{-9}\,\frac{\mathrm{m}^2}{\mathrm{s}} \tag{2.69}$$

$$D_\beta = 2 \cdot 10^{-5}\,\frac{\mathrm{m}^2}{\mathrm{s}} \tag{2.70}$$

The diffusion coefficients for ethanol and glucose in the liquid phase are neglected for advection playing the major role.

For a sequential co-simulation as described in chapter 6, the concentrations of ethanol, glucose, oxygen and yeast have to be initialized at the beginning of every CFX simulation. Initial values for following sequences result from simulations of biological growth.

Turbulence in the liquid is modeled with the modified standard k-ε-model. Gas phase turbulence is neglected. Bubble induced turbulence is considered for the liquid phase. The used model simplifies physics since only gas influences the liquid via additional source terms for the turbulence eddy dissipation and the turbulence kinetic energy. The effects do not directly influence bubble behavior. Effects of bubble induced turbulence are not taken into account for the bubble class with smallest mean diameter.

The column is entirely filled with the fluid mixture without a pure gas phase at the column top. Consequently, the top surface has to have a degassing region where the gas phase only is allowed to leave the reactor. This region is needed for continuity reasons since gas is flowing continuously into the control volume. Moreover, the top surface must have an overflow region where the liquid phase only can leave or enter the reactor. This region is also needed for continuity reasons especially at the beginning of each calculation allowing the adjustment of the correct gas holdup.

An outlet boundary condition with degassing option defines the degassing region. Only gas can leave the control volume over this region. For the liquid phase this region behaves like a wall with free slip. Simulation practice has shown that it is a good choice to set the diameter of the degassing region to the 0.85fold of the column inner diameter [90].

A concentric annulus surrounds the degassing region. Modeled as an opening it represents an infinite reservoir of liquid with the same characteristics as the adjacent liquid in the control volume. For fluid flowing back into the domain the variable values are set to the area average of the variable over the overflow region. The applied relative pressure is the adjacent pressure $p = p_\infty$.

Lines on the jet tubes enclosing all hole positions of the real system define the inlet area. A concentric annulus of the width of 30 mm between the inlet area and the cylinder jacket is considered not to be gassed. Coefficients define the gassed area on the inlet area related to the number and density of holes. Fractions of the actual gassed area for each class are based on gas holdup measurements [149].

All classes have the same inlet velocity perpendicular to the inlet surface. It is calculated via the superficial gas velocity $u_{\beta 0} = 0.034\,\frac{\mathrm{m}}{\mathrm{s}}$ and the overall gassed inlet surface. Superficial gas velocity is constant for all simulations and cultivations. The fraction coefficient for class one is 0.45, for class two 0.47 and for class three 0.08. Water is not allowed to enter the domain via this surface. Initial relative gas holdup values are 0.025, 0.051 and 0.024 for classes one to three.

The cylinder jacket, the bottom and the rest of the jet tubes are defined as walls. The wall is thought to be smooth. For contact the volume fraction of the fluids in adjacent elements is used. Water has the velocity zero at the wall whereas gas slips freely. This accounts for the fact that generally the wall is covered with a thin liquid film.

Gas-liquid operation level is set to 1800 mm for fluid dynamics simulations. For the case of sequential co-simulation in this work, the operation level starts with 1088 mm and results in 1133 mm, 1179 mm and 1224 mm after six, twelve and eighteen hours, respectively. Increase in operation level is caused by substrate feed.

Simulations are performed in three dimensions and transient manner using the commercial code CFX 11.0 by Ansys. Second order backward Euler scheme is used for discretization in time. The high resolution scheme has been used for advection. The number of coefficient loops is restricted to five. As convergence criteria root mean square residuals (RMS) have been limited to the upper residual target 10^{-4}.

The transient time step is set to $\Delta t = 0.005\,\mathrm{s}$. Thus, average CFL numbers are significantly below one. Since a fully implicit method is used, the CFL condition does not have strictly to be hold for every single element in order to obtain physically reliable results.

Chapter 3

Fluid Velocity in Measurement and Simulation

3.1 Measurement Techniques

Velocity measurement gives basic knowledge about flow characteristics. This knowledge is fundamental for optimizing systems and processes. It is also of great importance for validation of simulated velocity fields.

In multiphase flows velocity measurement of different phases is difficult since physical effects used for measurements in single phase systems often are disturbed. In gas-liquid two-phase flows with transparent phases gas bubbles give an impression of the flow. At the same time this impression can be absolutely wrong with respect to motion of the continuous phase. This is why reliable measurement techniques must give information about distinct phase velocities.

Available techniques are subdivided into invasive and non-invasive. Non-invasive techniques do normally not influence the flow. Most of these techniques are based on optical effects which is why they are restricted to almost transparent fluids with relatively low dispersed phase holdups. Therefore, common problems often require use of invasive techniques.

The interference between measurement systems and the flow depends upon the probe geometry and size. These parameters decide about the measurement volume and about the achievable resolution. Especially for local information about turbulent measures the probe size becomes important. In this work, average velocity information is sufficient, allowing the use of relatively large probe geometries.

Flow direction recognition is one of the most important requirements for transient flows where mesoscopic and macroscopic flow direction fluctuate. In such cases measurement techniques have to be stable with respect to changes in direction but also have to recognize the direction. Techniques where the flow direction has to be known up-front are not of much use for application to transient flows. Problematic incident flow directions often cause significant deviations [6].

Invasive probes have to be mechanically robust in order to be applied to a wide range of cases. It is common sense that multiphase flows stress any type of probe at elevated level.

3.1.1 Non-invasive Measurement Techniques

Non-invasive measurement techniques are generally based on particle tracking. Tracer particles have to be added which perfectly follow the flow without influencing it.

The first methods have been based on simple trajectory observation of added particles. Recent methods use fluorescent particles and imaging techniques to analyze the trajectories [33, 149]. In general these particle tracking (PT) techniques are good for qualitative flow field description.

Laser Doppler Anemometry (LDA) gives a point measure of the fluid velocity since the measurement volume is relatively small. Two coherent monochrome laser beams of the same intensity intersect in the measurement volume with a small angle. Interference patterns with stripes parallel to the bisector arise from intersection. Particles moving perpendicular to the stripes in the plane spanned by the laser beams scatter the light and modulate the frequency of the interference pattern. The modulated frequency is proportional to the particle velocity and consequently to the fluid velocity. A calibration of this system is not required [104].

Application of LDA to bubble columns is restricted to measuring depth of some centimeters and very low gas holdups [20, 83, 95, 12]. These restrictions in multiphase flow have been theoretically and practically constituted. The

main problem with optical methods in multi-phase flow are disturbances by the dispersed phase. Basic simulations have shown almost 100 % signal disturbance for bubbles of some millimeters in diameter, an overall gas holdup of only 3 % and a measuring depth of 0.2 m. Certainly, LDA in its basic form is not suitable for fluid velocity measurements in realistic multiphase problems [28].

Particle Image Velocimetry (PIV) gives flow field information on a plane. A light sheet is spanned at the section of interest. For the light sheet mainly laser systems are applied. Small tracer particles following perfectly the fluid flow scatter the light and can be detected with imaging techniques normal to the spanned plane. The movement of particle clusters is analyzed in following images [19]. As a result, the measurement resolution depends upon the selected section size. Since particle clusters are tracked instead of single particles, this method averages locally.

The method has similar problems as LDA. The gas holdup is restricted to very little percentage. Accordingly, possible measurement depths are some centimeters [33, 85]. Moreover, up-front to every analysis, bubbles have to be extracted from the images in order to get reliable information about the flow velocity. This technique is interesting for special research problems such as flow around single bubbles or bubble induced flow phenomena [87]. For most realistic multiphase problems the PIV technique is not applicable.

A developed add-on method is called Particle Tracking Velocimetry (PTV). Not only particle clusters for liquid flow measurement are analyzed but also dispersed phase velocity [19]. The analysis of the liquid phase velocity is followed by the analysis of the dispersed phase velocity. Three dimensional trajectories and related velocities can be determined by application of stereo techniques [132]. The problems stay the same as reported for PIV wherefore this method is not of major interest.

In addition there are some radioactive measurement techniques simular to PIV. Even though these methods have less problems with high phase holdups they are in disadvantage because of related restrictions in use and cost [22].

3.1.2 Invasive Measurement Techniques

Invasive techniques use for example convective heat and mass transfer or liquid phase momentum to detect fluid velocities. There are also particle tracking based methods following their non-invasive parental techniques. Invasive

probes always interact with the flow field and cause systematic measurement errors.

The most traditional probe types are pitot tubes and related probes. They generally measure the total pressure in relation to the static pressure. So, the dynamic pressure is determined which is proportional to the velocity squared. These probes measure velocity components normal to the probe head but lack the information of direction. The main flow direction has to be known up-front which is unrealistic for transient multiphase flows.

In order to account for the flow direction, multi-hole probes have been developed. After calibration, this probe type additionally gives the flow direction. Notwithstanding, the allowed angle of incident flow is restricted to about 90 degrees [98, 26].

A momentum based approach uses turbine type anemometers. These anemometers originate from wind tunnel measurements where the flow direction is known. In multiphase flows average flow velocities of the mixture are measured. The technique resolves only very low frequencies due to acting inertia forces while accelerating [56].

Heat transfer based systems are the Hot-Wire Anemometry (HWA) and the Hot-Film Anemometry (HFA). Metal probes are electrically heated. Either the temperature or the current is held constant. The correction is a measure for the convective heat transport and thus, for the fluid velocity. Since different phases have different heat transport characteristics, with some restrictions the method is also applicable to phase holdup detection [26].

For three dimensional measurements two general probe types are available. Hot-wire based multi-wire probes correlate information of different wires in order to extract directional information. In contrast, hot-film based split-film probes correlate information of two or more separated films on a single wire to determine the magnitude and the direction of the velocity vector. There are many other probe configurations especially based on hot-films.

While multi-wire probes are very restricted with respect to the incident flow direction, split-film probes can easily be used in transient flows having very good angular characteristics [56, 28]. Problems with this technique arise from two-dimensional calibration and three-dimensional measurements. The probe size restricts the resolution [7, 28]. Turbulent measures can be taken up to very high frequencies and relatively small scales [61, 60]. The technique does not depend upon optical density and thus works well in many practical solutions. Because of the thin wires most probes are mechanically weak.

Similar to HWA and HFA but measuring convective mass transport there is a technique called Electro Diffusion Measurement (EDM). Three or more wires are arranged to form a cylinder with circular cross section. The wires are isolated from each other. A not isolated end part of the formed cylinder builds up the active probe. The probes show good angular characteristics. Their size exceeds the size of HFA probes and entails a coarser resolution. Frequency resolution is significantly coarser in comparison to HFA because the technique is based on mass transport. The most important disadvantage is the requirement of electrolytes. Electrolytes change the measuring system. Major problems with probe aging have been reported. After all, EDM probes are cheap and easy to handle. Their applicability for multiphase flow systems has in conclusion not been reported [104].

Ultrasonic Doppler Anemometry (UDA) has the same working principle as LDA. Instead of added particles, bubbles reflect the sound of interfering ultrasonic sound waves in a modulated manner [76]. The technique is independent of liquid transparency. Under some assumptions, liquid velocity is calculated from gas velocities using the slip velocity [66]. Depending on the probes, this technique is limited to relatively small dispersed phase holdups.

A further development of the LDA technique for high disperse phase holdups and every needed measuring depth has been done by combining the classical LDA technique with a fiber optical system. The method is called Fiber Laser Doppler Anemometry (F-LDA) [28]. As a recent variation the Multi Mode Fiber Laser Doppler Anemometry (MMF-LDA) has been reported. The Fiber LDA methods combine the advantages of the LDA and those of an invasive measurement technique.

One of the most recent developments in flow velocity measurements is the Laser Cantilever Anemometry (LCA). This measurement technique is based on the working principle of an atomic force microscope [7]. A laser measures the tip deflection of a small cantilever beam. The tip deflection is proportional to the flow velocity squared. Very high frequencies can be measured. The system does not have sensitivity restrictions such as HFA has [7]. Generally LCA can determine the flow direction even though the reported probe shows good measurement results only for incident flow from one side [6]. Laser Cantilever Anemometry systems are not commercially available yet.

3.2 Pressure Probe for Velocity Measurement

Pressure probes as part of the invasive measurement techniques are widely applied in velocity measurement due to their simple and robust design. They are known to give precise results [98]. In literature three different types of pressure probes are mentioned for application in multiphase flow systems.

The simplest type is a pitot tube with one hole to measure total pressure [62, 70]. The static pressure has to be measured or known for determination of hydrodynamic pressure and velocity. For little impact pitot tubes shall be as thin as possible [22].

The second type is a modified pitot tube called Pavlov tube [77]. A tube is positioned across the reactor cross section. Two little holes in the surface turned about 90 ° and separated from each other inside the tube, measure the pressure. One of the holes has to be oriented opposing the flow direction of interest. The pressure difference is assumed to represent the dynamic portion of the total pressure.

The third type are multi-hole probes [98, 22]. These probes arrange a certain number of holes around a central one. Multi-hole probes can be used in two ways. First, the probe may be turned in the flow such that all surrounding holes measure the same pressure. It is assumed that the central hole then faces the main flow direction and directly measures the total pressure. Second, the probe is positioned in a known manner. Correlations between adjacent holes allow for calculation of velocity magnitude and direction [22]. Multi-hole probes are applicable in a certain cone of incident flow direction only.

Pressure measurement in multiphase flow systems has three important aspects. Bubble movement disturbs measurement and gives rise to higher values than expected [22]. This is why a correction factor depending on gas holdup has been suggested.

Probe shafts and mountings have to be as stiff as possible in order to reduce probe bending and related measurement errors [22]. Probes mounted on two sides of a reactor as well as metal shafts can sufficiently reduce the related error.

Furthermore, bubbles must not penetrate the inside of the measuring system since gas compressibility entails significant measuring error. Drainage systems with either constant drainage flow or drainage pulses before measurements guarantee gas free systems [77]. A pulse is always to be preferred because of reduced flow disturbance during measurement [22].

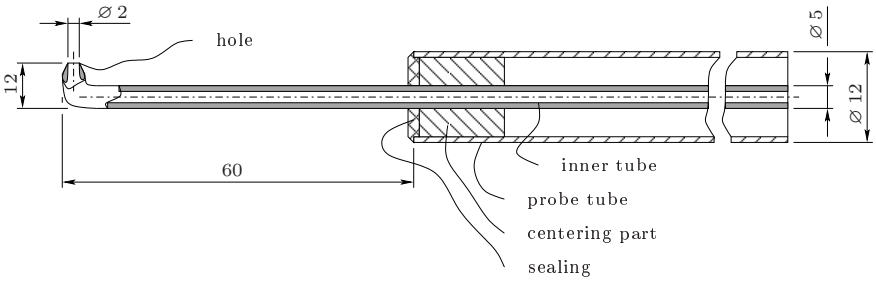

Figure 3.1: Cross sectional view of the pressure probe, measures in mm

Simplicity and robustness of the Pitot tube have been substantial arguments for the application. Reactor design does not allow probe dimensions as generally suggested [98]. The probe design is shown in **figure 3.1**. The outer steel tube provides shaft stiffness. The inner polymethylmetacrylate (PMMA) tube is filled with water. It connects the inside of the reactor with an inclined tube manometer.

The inclined tube manometer effectively measures pressure (**figure 3.2**). The inclined tube resolves pressure measurement depending on the inclination angle. Here, a resolution factor of 3.6 follows the inclination angle of $\alpha_p = 16\,°$. Inertia forces increase respond times. Resolution in time is decreased and averaged values can be taken only. Fluid flows into or out of the probe with changing pressure. Small hole diameters decrease resolution in time. At the same time, the diameter has to be small in order to hinder bubbles from penetration.

Pitot tubes are applicable as long as viscosity effects are negligible since the Bernoulli equation is limited to this region [50]. Equation 3.1 defines the probe Reynolds number Re_p:

$$\mathrm{Re}_p = \frac{\varrho_\alpha U d_p}{\eta_\alpha} \overset{!}{>} 100 \qquad \text{Eckelmann [50]} \tag{3.1}$$

Where ϱ_α is the liquid density, d_p the relevant probe outer diameter, U is the velocity magnitude and η_α the dynamic viscosity. With $U = 0.2\,\frac{\mathrm{m}}{\mathrm{s}}$ and $d_p = 0.005\,\mathrm{m}$ the probe Reynolds number becomes $\mathrm{Re}_p \approx 1000$. Thus,

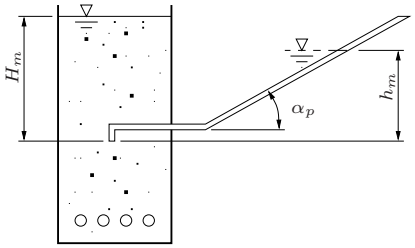

Figure 3.2: Pressure probe and inclined tube manometer

the method is applicable. Total pressure is overestimated for smaller probe Reynolds numbers.

In turbulent flows, pressure fluctuations cause overestimated total pressure [50]. Turbulence intensity Tu is defined in equation 3.2. For jet flows, it ranges between 30 and 60 %. Turbulence intensity of multiphase flows in bubble columns is assumed to range in the lower levels of jets, thus, about 30 %.

$$Tu = \frac{\sqrt{\overline{u'^2}}}{U} \tag{3.2}$$

With a maximal mean velocity component of about $U = 0.3\,\frac{\mathrm{m}}{\mathrm{s}}$, the fluctuating component becomes $u' = 0.09\,\frac{\mathrm{m}}{\mathrm{s}}$. Equation 3.3 estimates the maximum error due to turbulence ξ [50].

$$\xi = \frac{1}{2} \cdot \frac{\varrho_\alpha \overline{u'^2}}{2} \tag{3.3}$$

The ratio of maximum error due to measurements with a pitot tube in turbulent flows to the minimal measured mean velocity of about $0.1\,\frac{\mathrm{m}}{\mathrm{s}}$ and the related dynamic pressure of $5\,\frac{\mathrm{kg}}{\mathrm{s^2 m}}$, is given by

$$\frac{\xi}{\frac{\varrho_\alpha U^2}{2}} = \frac{2.025\,\frac{\mathrm{kg}}{\mathrm{s^2 m}}}{5\,\frac{\mathrm{kg}}{\mathrm{s^2 m}}} = 0.405 \tag{3.4}$$

In sum, liquid velocity measurement results with a pitot tube in the bubble column deviate at maximum about 40 %.

Pressure difference measurements are not applicable in multiphase systems with a pitot tube because the transient flow does not allow for static pressure measurement with holes commonly positioned on the side of the probe shaft. This also holds true for static pressure probes at the reactor wall. Electric devices for total pressure measurement have far too low resolution for application in watery systems since the ratio of dynamic to static pressure is very low. At the present time, no device is known with sufficient resolution and range for watery multiphase flow.

With the measures defined in figure 3.2, the velocity component in normal direction to the probe opening can be calculated by equation 3.5. Sources of error may result from uncertainties measuring the heights h_m and H_m as well as the gas holdup r_β.

$$u = \pm\sqrt{\frac{2}{\varrho_\alpha}\left(h_m \varrho_\alpha g - H_m \left(\varrho_\alpha(1-r_\beta) + \varrho_\beta r_\beta\right) g\right)} \tag{3.5}$$

Pitot tubes have to oppose the direction of flow in order to work properly. The design shown in figure 3.1 almost measures without error for incident flow directions with angles up to $\pm 20\,^\circ$ [98]. In turbulent flows, the flow direction is not necessarily known or changes direction in an unknown transient manner. For bubble columns, a time averaged flow field is well known with up-flow in the center and down-flow near the wall. Thus, average velocity on a radial profile shows a sign change measuring from the center in radial direction. As a consequence, the probe opening must face downwards in the center and upwards in the wall region. The educated guess about the position of sign change adds another uncertainty to this method.

3.3 Measured Velocity Profiles

Velocity profiles have been measured with the pressures probe (section 3.2) and with the strain gauge cantilever probe (section A).

Even though time averaged velocity profiles are generally referred to being axial symmetric [136, 28, 70], literature often also reports asymmetry [28, 66]. This may be caused by an angle between the reactor axis and direction of gravitational acceleration, due to the gassing system. Assuming symmetry, some researchers only measure on half plane. Other researchers symmetrize the measured profiles [66]. Results of this work are presented as asymmetric as measured.

Velocity profiles have been measured in parallel to the jet tubes axes on the center plane of the reactor. The levels are specified in figure 2.1. The distance between two measurement points in radial direction has been 20 mm. Each position has been measured twice with the probe normal vector in parallel to the reactor axis.

For all fitting positions a slightly asymmetric radial velocity profile has been determined. Values taken on the half-plane opposing the fittings are slightly higher than those taken on the half-plane of the fittings. The profiles for levels 900 mm and 1120 mm are shown in **figures 3.3** and **3.4**. At both levels, characteristics of the measured profiles are similar.

Measurements taken with the strain gauge cantilever probe are shown in figures A.10 and A.11 in chapter A. Values show the correct order of magnitude but differ significantly from other measurement and simulation results. The strain gauge cantilever probe has to be carefully reviewed and tested in order to be used for reliable measurement applications. Especially the probe size may be reduced in order to enhance spatial resolution.

Figures 3.3 and 3.4 also show experimental results from literature, taken 0.6 m above the gas distributor. Assuming validity of this comparison, both, measured and simulated results agree well with literature [67, 77]. Other well known correlations as those by Ueyama and Miyauchi [136] and Zehner [151] also confirm these results.

3.4 Simulated Velocity Profiles

For instance, simulated profiles for simple flow simulations without sequential coupling are shown in **figures 3.3** and **3.4**. As mentioned in section 2.10, a grid convergency study as well as a time step convergency study have been performed. Comparing central or maximal axial velocity components, it can be seen that results for the chosen time steps $\Delta t_c = 0.01\,\mathrm{s}$, $\Delta t_m = 0.005\,\mathrm{s}$ and $\Delta t_f = 0.0025\,\mathrm{s}$ do not significantly differ. Either of the time steps is acceptable in this case. Δt_m has been chosen for regular simulations because of CFL condition.

In contrast, grid convergency shows significant differences between results calculated on the different grids. Results on the coarse grid underestimate the maximum axial velocity by more than 30 %. Near wall velocities even differ about 50 %. On the contrary, the medium grid results in deviations

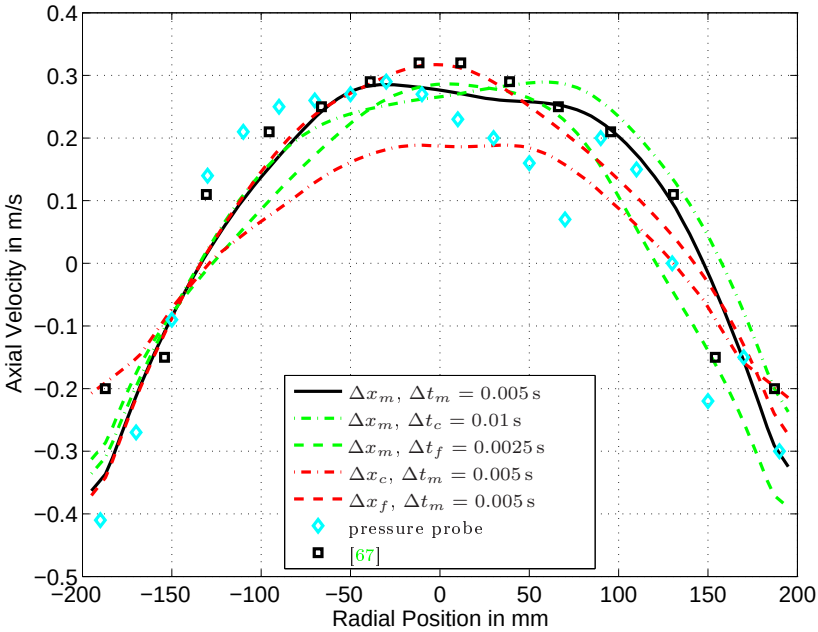

Figure 3.3: Measured and simulated velocity profiles at vertical position $z = 900\,\mathrm{mm}$, for positions and coordinates see figure 2.1, for mesh sizes see table 2.2

about 13 %. In conclusion, grid and time step convergency studies suggest the use of the medium grid Δx_m and the medium time step Δt_m.

Contour plots on planes $x = 0$ and $y = 0$ in **figure 3.5** visualize the flow field. The figure shows the time averaged axial liquid velocity component. Up-flow and down-flow regions are obvious. Jet tubes generate an adjacent flow field without major conflicts between up- and down-flow in contrast to classic gassing systems as plate spargers at the bottom.

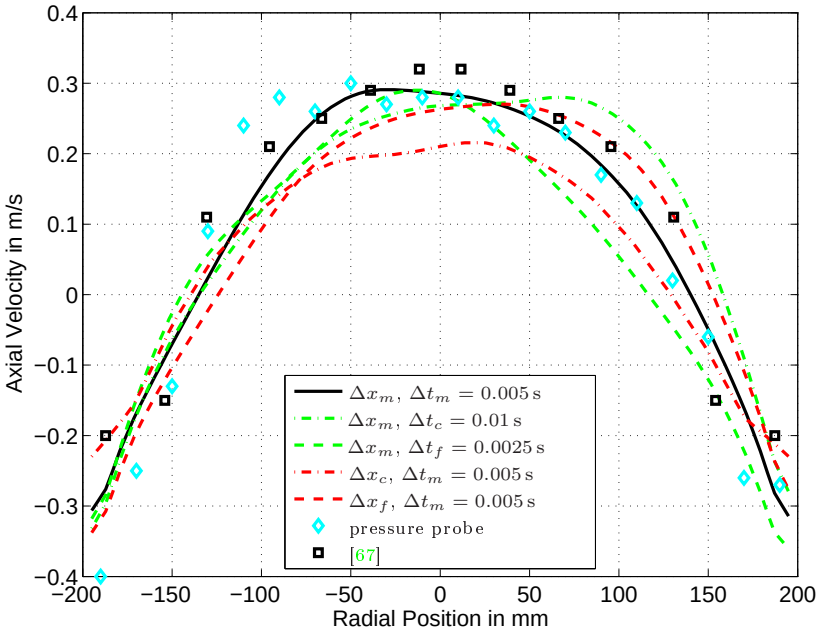

Figure 3.4: Measured and simulated velocity profiles at vertical position $z = 1120\,\mathrm{mm}$, for positions and coordinates see figure 2.1, for mesh sizes see table 2.2

Measured and simulated results show satisfactory agreement in total. Due to many aspects of the applied techniques and systems, the quality of measurements does not allow to pointwise compare velocity profiles. Spatial resolution of the probe and of the related simulation grid differ. Moreover, two-dimensional measurements may not be sufficient for detailed validation since slight inclination of the column causes significant changes in results. Differences increase with increasing distance from the sparging system.

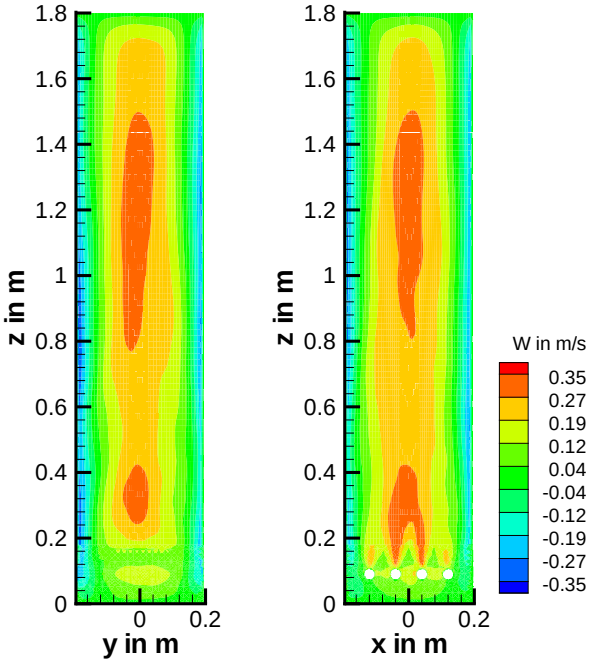

Figure 3.5: Simulated axial liquid velocity on planes $x = 0$ and $y = 0$, for positions and coordinates figure 2.1

The flow simulations of the reactor are meant to validate the method especially in terms of resolution in space and time. It is assumed that changes applied to the models for sequential co-simulation do not substantially change relevant results. That being the case, flow characteristics of sequential co-simulations have not explicitly been validated.

Chapter 4

Growth Model

4.1 Saccharomyces cerevisiae

Yeast species such as *Saccharomyces cerevisiae* grow under aerobic and anaerobic growth conditions producing new biomass. The major objective in baker's yeast production is the production of active and stable yeast cells. Activity means the ability to produce carbon dioxide under anaerobic conditions especially in a dough.

There are three ways for yeast to produce biomass, namely oxidative growth on glucose or on ethanol and reductive growth on glucose [106]. Reductive growth is also referred to as fermentation. Equations 4.1 to 4.3 describe the stoichiometry [127]. Equations 4.1 and 4.3 represent oxidative growth while equation 4.2 represents reductive growth.

$$\begin{aligned} C_6H_{12}O_6 + a \cdot O_2 + b \cdot nx \cdot NH_3 &\longrightarrow && (4.1)\\ b \cdot C_1H_{hx}O_{ox}N_{nx} &+ c \cdot CO_2 + d \cdot H_2O \\ C_6H_{12}O_6 + g \cdot nx \cdot NH_3 &\longrightarrow && (4.2)\\ g \cdot C_1H_{hx}O_{ox}N_{nx} &+ h \cdot CO_2 + i \cdot H_2O + j \cdot C_2H_6O \\ C_2H_6O + k \cdot O_2 + l \cdot nx \cdot NH_3 &\longrightarrow && (4.3)\\ l \cdot C_1H_{hx}O_{ox}N_{nx} &+ m \cdot CO_2 + n \cdot H_2O \end{aligned}$$

Biomass is represented by the formula $C_1H_{hx}O_{ox}N_{nx}$ in the equations 4.1 to 4.3. The terms hx, ox and nx as well as the molecular weight are calculated from elementary analysis.

Some yeast species are sensitive to glucose concentration [106]. This sensitivity is expressed under aerobic conditions in a change from pure oxidative growth to an oxido-reductive growth where equations 4.1 and 4.2 are applied. This state is termed respiratory bottleneck. Even though there is no limitation with respect to oxygen, glucose cannot purely be used on the oxidative path. Glucose concentrations of about $S = 0.04 \frac{g}{L}$ and above are metabolized in the oxido-reductive manner and ethanol is produced [106].

The effect is also known as glucose effect, overflow metabolism [127], Crabtree effect or as catabolite repression [106]. Respiratory capacity is not the fundamental reason for the effect [140]. Sonnleitner and Käppeli [127] propose the terms oxidative growth for equation 4.1, oxido-reductive growth for equations 4.1 and 4.3 and reductive growth for equation 4.2. In presence of ethanol, undesired oxygen from glucose oxidation can be oxidized via equation 4.3. Thus, the latter equation can be applied to the oxidative and the oxido-reductive growth.

Since the overflow metabolism in cultivations is very common, there is a need for models reflecting this effect. In this work, an unstructured kinetic model has been used [106]. Details about the model are given in section 4.2. Biomass and ethanol production as well as glucose, ethanol and oxygen consumption are considered for calculating the concentrations of biomass, glucose, ethanol and oxygen. The model also accounts for ethanol inhibition on the maximum respiration capacity of yeast. Some additions and modifications adjust the model to the special needs for use in a combined simulation of fluid dynamics and biological growth. Biomass is assumed to be of the general composition $CH_{1.82}O_{0.58}N_{0.16}$ [13, 127].

4.2 Kinetic Growth Model

The kinetic growth model is based upon the work by Pham et al. [106]. Model description is based on glucose uptake and consumption since this is known as the main substrate and inhibiting material in the considered growth of *Saccharomyces cerevisiae*. The model description follows in general the order of implementation in Matlab and Simulink. For definitions of model constants, parameters and initial values see **table B.1**.

Following Monod kinetics, the glucose uptake rate is defined as q_s considering a lag time t_L.

$$q_s = q_{s,max} \frac{S}{S + K_s} \left(1 - e^{-\frac{t}{t_L}}\right) \tag{4.4}$$

In the same manner the critical glucose uptake rate is defined with S_{crit} instead of S.

$$q_{s,crit} = q_{s,max} \frac{S_{crit}}{S_{crit} + K_s} \left(1 - e^{-\frac{t}{t_L}}\right) \tag{4.5}$$

The ratio of the glucose uptake rate q_s and the critical glucose uptake rate $q_{s,crit}$ define the portions of the glucose uptake rate used for oxidative and fermentative yeast growth.

$$q_s \leq q_{s,crit} \implies \begin{cases} q_{s_{ox}} = q_s \\ q_{s_f} = 0 \end{cases} \tag{4.6}$$

$$q_s > q_{s,crit} \implies \begin{cases} q_{s_{ox}} = q_{s,crit} \\ q_{s_f} = q_s - q_{s,crit} \end{cases} \tag{4.7}$$

Glucose taken up for oxidative growth is divided into one portion for anabolism and one for energy metabolism. $q_m = 0.01 \frac{\text{g}}{\text{gh}}$ is the glucose uptake rate for maintenance.

$$q_{s_{ox}an} = (q_{s_{ox}} - q_m) Y_{xs_{ox}} \frac{C_x}{C_s} \tag{4.8}$$

$$q_{s_{ox}en} = q_{s_{ox}} - q_{s_{ox}an} \tag{4.9}$$

Oxygen uptake rate for glucose oxidation reads as follows.

$$q_{O_2 s} = q_{s_{ox}en} Y_{os} \tag{4.10}$$

The oxygen uptake rate for glucose oxidation obviously cannot exceed the maximum specific oxygen uptake rate which is the concept of a bottleneck.

$$q_{O_2 s} \overset{!}{\leq} q_{O_2,max} \tag{4.11}$$

The limit described in equation 4.11 with consideration of ethanol inhibition is implemented as follows. If the oxygen uptake rate exceeds the specified

limit, the rate is set to the limit proportionally reducing the glucose uptake rate for oxidative growth $q_{s_{ox}an}$ and $q_{s_{ox}en}$.

$$\begin{aligned} q_{O_2 s} &> q_{O_2,max}\left(\frac{K_i}{K_i+E}\right) \\ &\Longrightarrow q_{O_2 s} = q_{O_2,max}\left(\frac{K_i}{K_i+E}\right) \qquad (4.12) \\ q_{O_2 s} &\leq q_{O_2,max}\left(\frac{K_i}{K_i+E}\right) \\ &\Longrightarrow q_{O_2 s} = q_{O_2 s} \qquad (4.13) \end{aligned}$$

Proportional reduction of $q_{s_{ox}an}$ and $q_{s_{ox}en}$ does not have to be implemented. With equation 4.12 results are the same. Nevertheless, the method is described in short. If inequation 4.12 is true, the ratio of both sides of the inequation is defined as reduction factor $f_{p,red}$. Then by definition the factor is greater than one.

$$f_{p,red} = \frac{q_{O_2 s}}{q_{O_2,max}} \qquad (4.14)$$

$$q_{s_{ox}an} = \frac{q_{s_{ox}an}}{f_{p,red}} \qquad (4.15)$$

$$q_{s_{ox}en} = \frac{q_{s_{ox}en}}{f_{p,red}} \qquad (4.16)$$

$q_{e_{en}}$ is the maximum ethanol consumption rate for energy metabolism.

$$q_{e_{en}} = \frac{q_{O_2,max} - q_{O_2 s}}{Y_{oe}} \frac{E}{E+K_e} \qquad (4.17)$$

The overall oxygen uptake rate is made up of the oxygen uptake rates for glucose and ethanol oxidation respectively.

$$q_{O_2} = q_{O_2 s} + q_{e_{en}} Y_{oe} \qquad (4.18)$$

The overall ethanol uptake rate q_{ec} and ethanol uptake rate for anabolism $q_{e_{an}}$ are defined in equations 4.19 and 4.20. In equation 4.21 this system of

equations is solved for q_{ean}.

$$q_{ec} = q_{e_{en}} + q_{e_{an}} \tag{4.19}$$

$$q_{e_{an}} = q_{ec} Y_{xe} \frac{C_x}{C_e} \tag{4.20}$$

$$q_{e_{an}} = q_{e_{en}} \frac{Y_{xe} C_x}{C_e - Y_{xe} C_x} \tag{4.21}$$

q_{ec} does not have to be limited to the actual ethanol concentration since equation 4.17 automatically limits the uptake rate.

It remains to calculate the fermentative part. In analogy to the oxidative part, it will be distinguished between anabolism and energy metabolism. The glucose uptake rate for the fermentative part is the difference between the overall glucose uptake rate and the glucose uptake rate for the oxidative part.

$$q_{s_f} = q_s - q_{s_{ox}} \tag{4.22}$$

Glucose uptake rate for the fermentative anabolism reads as follows.

$$q_{s_f an} = q_{s_f} Y_{xsf} \frac{C_x}{C_s} \tag{4.23}$$

The glucose uptake rate for fermentative energy metabolism is defined as

$$q_{s_f en} = q_{s_f} - q_{s_f an} \tag{4.24}$$

Equation 4.24 allows to calculate the ethanol production rate q_{ep}.

$$q_{ep} = q_{s_f en} Y_{es} \tag{4.25}$$

The specific growth rate μ is calculated as a combination of both, the oxidative and the fermentative part of the model.

$$\mu = (q_{s_{ox}} - q_m) Y_{xs_{ox}} + q_{s_f} Y_{xs_f} + q_{ec} Y_{xe} \tag{4.26}$$

In equation 4.26 the first summand represents the growth due to oxidative growth on glucose, the second summand stands for the fermentative growth on glucose and the third constitutes the yeast growth due to ethanol oxidation.

4.3 Mass Balances

The mass balance is a set of ordinary differential equations. Each equation for the different variables is of the following form.

$$\frac{\mathrm{d}var}{\mathrm{d}t} = var_p - var_c \tag{4.27}$$

var is a specific but arbitrary variable, var_p is the production and var_c the consumption term. In Matlab notation only the right hand side of equation 4.27 is written down. Matlab solver interprets these equations accordingly.

The mass balance equations for ethanol, oxygen, glucose, yeast mass and the volume follow are given in equations 4.28 to 4.32. Symbols with asterisk have the units of mass. Symbols without asterisk have units of mass density.

$$\frac{\mathrm{d}E^*}{\mathrm{d}t} = \frac{\mathrm{d}E \cdot V}{\mathrm{d}t} = (q_{ep} - q_{ec})XV \tag{4.28}$$

$$\frac{\mathrm{d}O^*}{\mathrm{d}t} = \frac{\mathrm{d}O \cdot V}{\mathrm{d}t} = (q_{O_2,in} - q_{O_2}X)V \tag{4.29}$$

$$\frac{\mathrm{d}S^*}{\mathrm{d}t} = \frac{\mathrm{d}S \cdot V}{\mathrm{d}t} = (q_{s,in} - q_sX)V \tag{4.30}$$

$$\frac{\mathrm{d}X^*}{\mathrm{d}t} = \frac{\mathrm{d}X \cdot V}{\mathrm{d}t} = \mu XV \tag{4.31}$$

$$\frac{\mathrm{d}V}{\mathrm{d}t} = \frac{q_{s,in}V}{S_{in}} \tag{4.32}$$

Following the exponential growth to a certain level, the glucose feed function is given by equation 4.33. S_{in} is the glucose concentration in the feed.

$$q_{s,in}V = \min(q_{s,in,0}Ve^{0.3t}; q_{s,in,max}V) \tag{4.33}$$

The oxygen input rate $q_{O_2,in}$ is calculated from mass transfer description introduced in section 2.8. The concept of co-simulation requires oxygen mass transfer to be calculated in both, the fluid dynamics module and the biological growth module.

Equations 4.28 to 4.32 are solved by the Simulink integrator block. This block integrates a function $u(t)$ over a specified interval $]t_0; t[$ considering the initial conditions y_0.

$$y(t) = \int_{t_0}^{t} u(t)\mathrm{d}t + y_0 \tag{4.34}$$

An explicit Runge-Kutta method with the Darmand-Prince pair (4, 5) implemented in Matlab as function *ode45* is used to solve the mass balances. This solver is an one step solver where only the latest solution is used for computing the next. The step size is variable. The relative tolerance is set to $1 \cdot 10^{-4}$. The absolute tolerance as well as the maximum, the minimum and the initial step size are automatically determined by Matlab.

4.4 Structure of the Implemented Model

For implementation in Matlab/Simulink the model is structured as shown in **figure 4.1**. Simulink is a block based environment. Therefore, models may be clearly structured while blocks represent subsystems of the model.

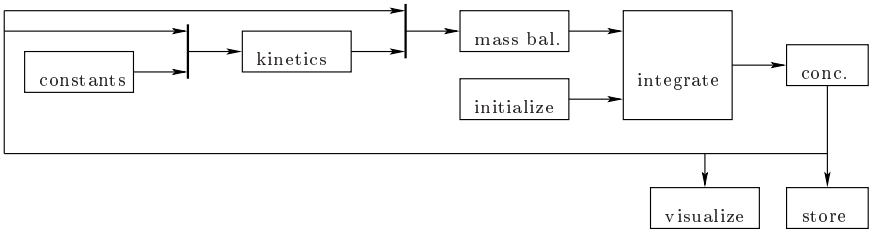

Figure 4.1: Model structure as implemented in Matlab/Simulink

Section 4.2 describes the *kinetics* block in detail while section 4.3 gives access to the *mass balance* block. This block also contains the mass transfer as described in section 2.8. Blocks *constants* and *initialize* in general cover table B.1. The *integrate* block solves equations 4.28 to 4.32. The calculation from masses to mass concentrations is performed in the *concentration* block.

For use in sequential co-simulations and for postprocessing, the blocks *store* and *visualize* respectively store and visualize simulation results.

Chapter 5

Cultivation of Yeast

5.1 Type of Cultivation

Yeast may be cultivated in the continuous, the batch and in the fed-batch mode. Baker's yeast is industrially produced in the fed-batch mode. This is why the method has been the same for the experiments.

Solved oxygen concentration serves as control parameter. In the presence of glucose or ethanol and oxygen yeast grows oxidatively. Solved oxygen concentration decreases. When substrate concentration is significantly reduced yeast growth slows down and the solved oxygen concentration rises. At this point, the control mechanism is initiated.

Every time the solved oxygen concentration exceeds a specified level, medium is fed into the reactor. The controller behaves proportionally. Consequently, setting a low critical level is the only way to increase the overall performance holding the yeast culture at a high growth rate and pure oxidative growth.

5.2 Experimental Setup

The reactor is a PMMA tube with circular cross section area as described in section 2.9. Figure 2.1 shows system geometry and measures.

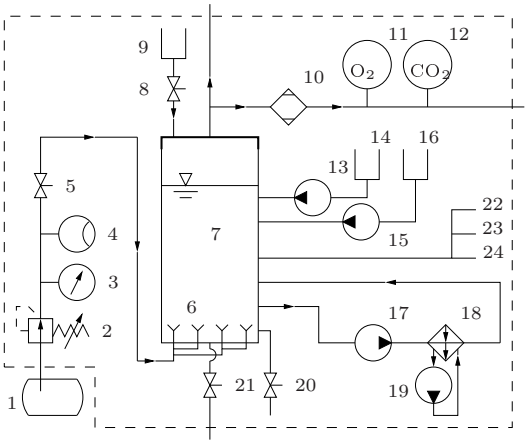

Figure 5.1: Reactor fluid flow scheme, system boundary as dashed line

The numbers of the following list refer to **figure 5.1**. The dashed line marks the boundary of the system. Used devices are listed in the appendix C.1.

1. Reservoir with compressed air
2. Pressure reduction valve
3. Manometer
4. Variable area flow meter
5. Stop valve gas inlet
6. Gassing system, jet tubes
7. Reactor
8. Stop valve anti foam agent inlet
9. Anti foam agent container
10. Gas drier
11. O_2 probe
12. CO_2 probe
13. Medium pump
14. Medium container on a scale
15. Alkaline solution pump
16. Alkaline solution container
17. Cooling and heating circuit pump
18. Heat exchanger

19. Secondary cooling and heating circuit pump and control
20. Stop valve sampling outlet
21. Stop valve reactor outlet
22. Thermometer
23. pH probe and control
24. pO_2 probe and control

5.3 Cultivation Experiment

The Cultivation experiment has been performed in order to generally check the validity of the growth model. Research in yeast growth has extensively been reported in literature wherefore cultivation in this work has been reduced to the necessary scope. At this stage of development of the sequential co-simulation, the comparison with a single cultivation has been assessed as being sufficient. Parameters have not been varied.

The initial and the feed medium composition are given in section C.2. In comparison to the feed medium, the initial medium for the reactor has some reduced concentrations. The glucose concentration for example is reduced to 2 g per liter since significantly higher concentrations cause production of ethanol. The pH value is controlled to the value of 5 by adequate feed of 5 molar NaOH. Temperature is controlled to maintain the level of 30 °C. Foam generation is hindered by manually adding anti foam agent Ucolub N115. Since anti foam agents diminish mass transfer, the addition has to be minimized only adding on demand.

During cultivation the pH value, the solved oxygen concentration pO_2, the off gas oxygen and carbon dioxide concentration as well as temperature are measured. Information about the solved oxygen concentration is of special interest because it directly relates to the actual state of cultivation in terms of being aerobic or anaerobic. 0.05 L samples have been taken every 15 minutes without filling up the volume. The related error is neglected.

The reactor is filled with water and aerated at constant superficial gas velocity $u_{\beta 0} = 0.034 \frac{\mathrm{m}}{\mathrm{s}}$ 24 hours before a cultivation. This preliminary run serves for calibration of the off gas measurement instruments. Superficial gas velocity is constant for all simulations and cultivations. The off gas is cooled and dried.

Directly before the cultivation starts initial concentrations of salts, glucose, vitamins and trace elements in the medium are adjusted. Yeast suspended in 5 L water initializes the cultivation as inoculum. In order to ac-

climatize the yeast to aerobic growth conditions medium feed is set constant to $0.6\,\frac{\mathrm{L}}{\mathrm{h}}$ for ten to twelve hours. During this period only spot check samples are taken. After that, the actual cultivation starts with the pO_2 controlled feed.

5.4 Sample Analysis

Devices and methods for sample analysis are listed in detail in section C.3. From every sample, 2 mL have been filtered and deep-freezed at $-18\,^{\circ}\mathrm{C}$ for later analysis with high performance liquid chromatography (HPLC). With HPLC glucose and ethanol concentration have been determined. A second 2 mL sample has been filtered and heated for 10 minutes at $94\,^{\circ}\mathrm{C}$. Since the medium has not been heat sterilized, the heating is necessary to fast adjust the mutarotation equilibrium. After cooling, the glucose concentration has been enzymatically measured with an analyzer (section C.3).

Biomass dry weight concentration has also been determined in two ways. First, optical density has been measured with values ranging from 0.2 to 0.8 with a sample in a micro cuvette using 600 nm wave length. The values for optical density ranged from 0.2 to 0.8 corresponding to dilutions of a hundredth. Second, 40 mL samples have been taken in a 50 mL centrifuge tube. The centrifuge tubes have been dried 24 hours at $100\,^{\circ}\mathrm{C}$ and weighted. The taken samples are centrifuged at $10,000 \cdot \mathrm{g}$ for ten minutes. After decanting the water and washing these probes with 15 mL demineralized water, they have been centrifuged another ten minutes at $10,000 \cdot \mathrm{g}$. The decanted samples in the centrifuge tubes have been dried at $100\,^{\circ}\mathrm{C}$ for 48 hours and afterwards weighted.

5.5 Cultivation Report

Yeast has been cultivated over 18 hours. The substrate feed has been pO_2 controlled. Thus, the feed profile is self-adjusted. A pure growth simulation has been carried out to compare with the cultivation results. Model parameters differing from those given in table B.1 are given in **table C.1**. Since biomass production is the main goal in baker's yeast industry, analysis of results is focused on correct simulation of biomass dry weight concentration. **Figure 5.2** shows the results for biomass dry weight concentration for cul-

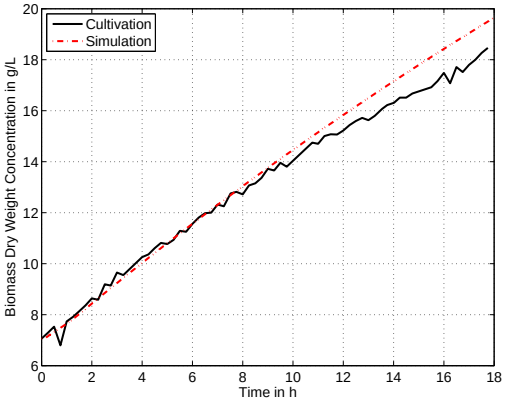

Figure 5.2: Biomass dry weight concentration in fed-batch cultivation and growth simulation at 30 °C, $u_{\beta 0} = 0.034\,\frac{\mathrm{m}}{\mathrm{s}}$

tivation and simulation. The prediction of the simulation is good. During the last eight hours the simulation over-predicts the biomass concentration about 6 %.

In **figure 5.3** the substrate feed profiles for cultivation and simulation are compared. The feed rate for the simulation has been set according to the measured feed rate and the feed function (equation 4.33).

Simulation and cultivation of the overall reaction volume given in **figure 5.4** have to agree, since an increase in volume in the simulation is directly affected by the given substrate feed rate and the feed concentration. The maximum deviation is less than one percent.

Glucose concentration profiles in **figure 5.5** are simular but deviate in their absolute value. Neither of the applied measurement techniques has given reliable results for glucose concentration. Deviation is partially caused by elevated levels of salt concentration. The definite reason for the deviation has not been found. It is of minor importance in this case since biomass dry weight concentration has very well been predicted and overall model performance is reasonable.

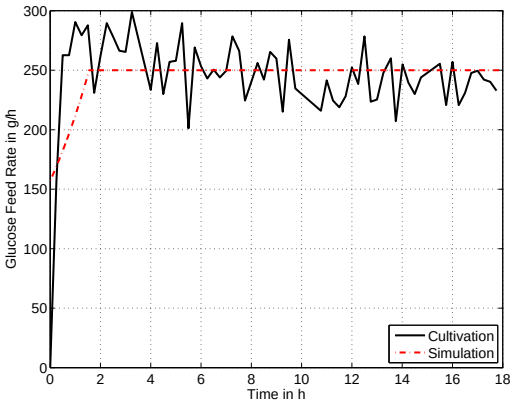

Figure 5.3: Substrate feed in cultivation and growth simulation at 30 °C, $u_{\beta 0} = 0.034 \frac{\mathrm{m}}{\mathrm{s}}$, feed function see equation 4.33

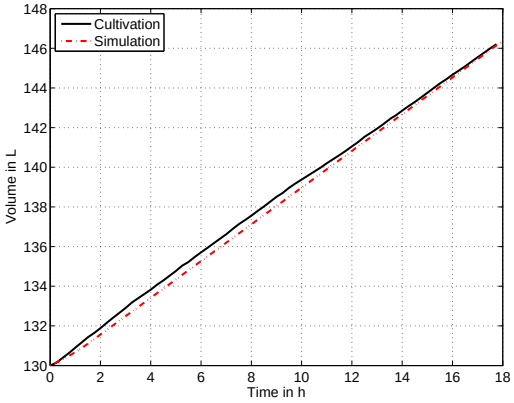

Figure 5.4: Overall reaction volume in fed-batch cultivation and growth simulation at 30 °C, $u_{\beta 0} = 0.034 \frac{\mathrm{m}}{\mathrm{s}}$

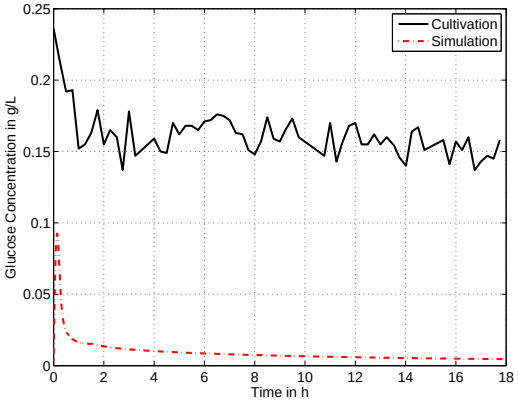

Figure 5.5: Glucose concentration in fed-batch cultivation and growth simulation at 30 °C, $u_{\beta 0} = 0.034 \frac{\mathrm{m}}{\mathrm{s}}$

In contrast to glucose concentration, the measured solved oxygen concentrations are much more reliable (**figure 5.6**). The solved oxygen concentration is significantly below the saturation concentration for air in water. Except from some peaks in the measured profile, the values remain constant during the entire cultivation. Absolute deviations of simulated values probably result from uncertainties in the model of oxygen mass transfer. This may also be the major reason for deviations of simulation results. The use of the correct bubble diameters is required in order to achieve optimal models.

Growth as well as fluid dynamics are directly influenced by bubble size. Model sensitivity with respect to changes in bubble size are discussed in the following paragraphs. Deviations in bubble size may either be represented by larger or by smaller bubble diameters.

Modeling bubbles with smaller diameters, the average rise velocity and induced liquid velocity decrease while dispersed phase volume fraction and interphase area density increase. On the contrary, modeling bubbles with larger diameters results in increasing rise and liquid velocities. Dispersed phase volume fraction, interphase area density, solved oxygen concentration and mixing time are reduced at the same time.

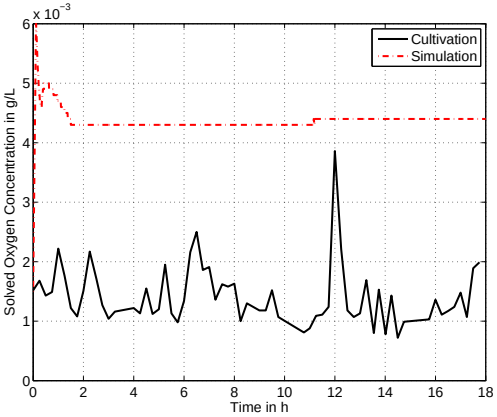

Figure 5.6: Solved oxygen concentration in fed-batch cultivation and growth simulation at 30 °C, $u_{\beta 0} = 0.034\,\frac{\mathrm{m}}{\mathrm{s}}$

Assuming modeled bubble diameter to deviate $i\,\%$ and consequently dispersed phase volume fraction to deviate $ii\,\%$ from the correct value, equation 5.1 shows the resulting error in calculated interphase area density and thereby in mass transfer rate.

$$\frac{a_{\alpha\beta id}}{a_{\alpha\beta i}} = \frac{6\frac{r_{\beta id}}{d_{\beta,id}}}{6\frac{r_{\beta i}}{d_{\beta,i}}} = \frac{\frac{1+ii\,\%}{1+i\,\%}\frac{r_{\beta i}}{d_{\beta,i}}}{\frac{r_{\beta i}}{d_{\beta,i}}} = \frac{1+ii\,\%}{1+i\,\%} \tag{5.1}$$

Decreasing bubble diameters generally come along with increasing dispersed phase volume fractions. That is, i and ii have different signs amplifying the deviation in interphase area density and mass transfer rate. The factor from equation 5.1 may be rewritten as follows.

$$\frac{1+ii\,\%}{1+i\,\%} \quad\Longrightarrow\quad \frac{1+|ii\,\%|}{1-|i\,\%|} \quad \text{or} \tag{5.2}$$

$$\Longrightarrow\quad \frac{1-|ii\,\%|}{1+|i\,\%|} \tag{5.3}$$

Amplification of errors does not much influence growth as long as oxygen support is not limited. Equation 5.1 points out model sensitivity with respect

to the bubble diameters. In case that both, bubble diameter and dispersed phase volume fraction, deviate 10 % from the correct value the resulting error ranges between 18 and 22 % following equations 5.2 and 5.3.

The growth simulation sufficiently predicts yeast growth. Treating the reaction volume as a single perfectly mixed element in the simple growth simulation might be a reason for deviations. This treatment well approximates growth in small reactors like the one used in this work. Prediction quality decreases with increasing volume. The sequential co-simulation is an alternative for simulation of large reaction volumes. The element size for the growth sequences has to fulfill the requirements of perfectly mixed volumes.

Chapter 6

Sequential Co-simulation

6.1 Principle of the Method

Time scales in fluid dynamics of milli seconds to seconds and in growth of hours to days differ significantly and require special handling in combined simulations. In the near future, there is no chance to directly co-simulate growth and fluid dynamics for relevant cultivation times as it is possible for fast chemical reactions. Thus, a sequential treatment of the co-simulation partners is proposed.

After simulating fluid dynamics for a representative period of time, interphase parameters are exchanged for growth simulation. Since the time scale for growth is much larger than it is for fluid dynamics, the periods of time for growth simulation will generally exceed those for fluid dynamics simulation by far. The fundamental principle of the sequential co-simulation is shown in **figure 6.1**. Fluid dynamics are calculated with Ansys CFX while yeast growth is calculated with Matlab and Simulink.

The chosen periods of time for every single sequence depend upon the expected changes during these periods. A sequence may be long if growth parameters do not significantly change. The same holds true for fluid dynamics. In case of great changes of fluid characteristics or volume for example due to growth there is a definite need for shorter sequences.

There are two fundamental ways of sequential co-simulation. First, the length of sequences can be held constant which cannot account for the rate of

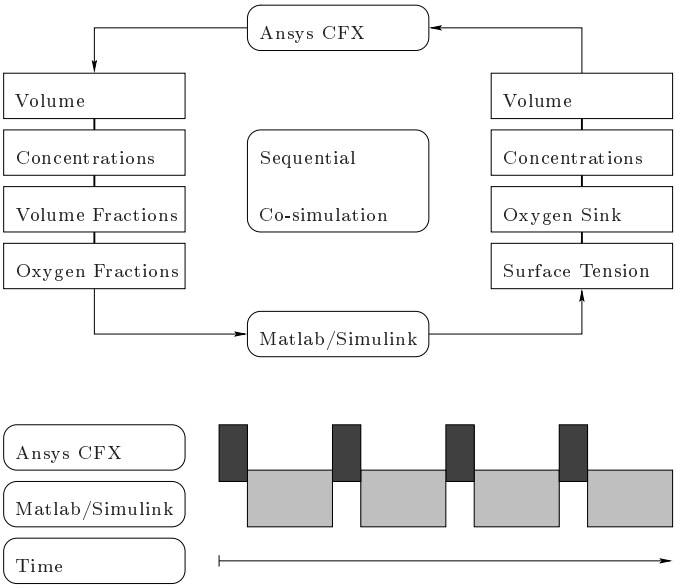

Figure 6.1: Sequential co-simulation in principle with its interfaces used in this work, see also section 2.11

change of a relevant variable. Second, the rate of change of the variable can be bound such that the length of sequences will probably differ. Simulating the same problem set and assuming a similar number of sequences the latter method is assumed to provide better results.

It is assumed that flow conditions do not significantly change during the simulated sequence of growth. Correspondingly, each element has its constant supply of substrates and oxygen. During growth, no exchange between elements is considered. Modeling error decreases with an increasing number of simulated sequences.

A feed function for medium is given up-front as defined in equation 4.33. It depends upon the method of cultivation, the overall volume as well as yeast and substrate concentration at the beginning. Start and end point of a growth sequence determine the related part of the feed function.

6.2 Interfaces

Interface parameters are exchanged switching the modules between calculations (figure 6.1). Significant changes are related to concentrations of the microorganism, substrates and products. Volume changes are also considered. Results of the simulation of growth are interpolated to the grid of the flow field as initialization of the CFX calculation. The results from CFX are reduced to a set of convenient size as described in section 6.4. This set forms the basis for growth simulations with Matlab. Growth simulations may be parallelized in the future.

6.2.1 Interface from CFX to Matlab

For simulation of growth in Matlab, the following variables have to be transmitted.

- position
- element volume
- local gas volume fractions
- oxygen concentration, air
- ethanol concentration, liquid
- glucose concentration, liquid
- oxygen concentration, liquid
- yeast concentration, liquid

The term *history of air* describes the history a specific volume element of air has experienced on the way to the present position. The dispersed phase experiences different volume elements and therefore differently transfers oxygen.The transmitted variables are used to calculate the history of air as well as oxygen mass transfer. Especially in large reactors the oxygen concentration in air may very much differ depending on position. At only very few positions the oxygen concentration in air will be close to the concentration in fresh air.

A finite number of volume elements represents the reduced data set for growth simulation. For simplicity the volume elements are assumed to be equal in size. This method reduces complexity but decreases quality of representing the original system. Areas with many small elements will be overrepresented whereas those with coarse grid resolution will be underrepresented. Since fine mesh resolution mainly correlates with near wall regions

or those close to the gassing system and both regions have opposite oxygen concentrations the errors from over-representation will fairly compensate.

Equation 6.2 gives the definition of the element volume V_{red} for the reduced data set.

$$V_{CFX} = \sum_{i_{CFX}}^{n_{CFX}} V_{i,CFX} \tag{6.1}$$

$$V_{red} = \frac{1}{n_{red}} \sum_{i_{CFX}}^{n_{CFX}} V_{i,CFX} \tag{6.2}$$

6.2.2 Interface from Matlab to CFX

For initialization of the next sequence in CFX the following variables are transmitted.

- position
- element volume
- ethanol concentration, liquid
- glucose concentration, liquid
- oxygen concentration, liquid
- yeast concentration, liquid
- oxygen sink representing the oxygen consumption of yeast in the continuous phase

The data has to be processed in a way that the *initialize profile data* function in CFX is able to interpolate the data to the new mesh.

Feed in the growth simulation is the same function for all volume elements. It is assumed that mixing processes in average result in the same feed for every position in the reactor. When the feed function is the same for all elements this is also true for the increase in element volume. Therefore, the overall volume after a growth sequence is calculated as $V_{CFX,vc}$.

$$V_{CFX,vc} = n_{red} V_{red,vc} \tag{6.3}$$

Beside the volume the oxygen sink $\dot{m}_{Y,Matlab}$ as a representation of oxygen consumption of yeast in the continuous phase describes an important variable

Table 6.1: Physical properties of the continuous phase at the beginning and the end of a cultivation

Property	Unit	Beginning of Cultivation	End of Cultivation
η_α	$\frac{\mathrm{kg}}{\mathrm{s\,m}}$	10^{-3}	$2 \cdot 10^{-3}$
ϱ_α	$\frac{\mathrm{kg}}{\mathrm{m}^3}$	997	1029
σ	$\frac{\mathrm{kg}}{\mathrm{s}^2}$	0.0735	0.04

to be transmitted.

$$\dot{m}_{Y,Matlab} = \frac{1}{n_{red} V_{red,vc}} \sum_{i}^{n_{red}} q_{O_2} X V_{red,vc} \tag{6.4}$$

$$= \frac{1}{n_{red}} \sum_{i}^{n_{red}} q_{O_2} X \tag{6.5}$$

In this work values for $\dot{m}_{Y,Matlab}$ resulting from the sequential co-simulation at the beginning of a cultivation, after six, twelve and eighteen hours are $1.962 \cdot 10^{-4}\ \frac{\mathrm{kg}}{\mathrm{s\,m}^3}$, $2.38 \cdot 10^{-4}\ \frac{\mathrm{kg}}{\mathrm{s\,m}^3}$, $2.45 \cdot 10^{-4}\ \frac{\mathrm{kg}}{\mathrm{s\,m}^3}$ and $2.51 \cdot 10^{-4}\ \frac{\mathrm{kg}}{\mathrm{s\,m}^3}$, respectively. The oxygen concentration of the liquid phase in CFX then results from the sum of source and sink terms.

Physical properties of the continuous phase or the system of fluids such as viscosity, density and surface tension are of major interest in fluid dynamics simulation. Typical property ranges are given in **table 6.1**. Viscosity measurements of cultivation samples have shown values from about $10^{-3}\ \frac{\mathrm{kg}}{\mathrm{s\,m}}$ at the beginning of a cultivation to $2 \cdot 10^{-3}\ \frac{\mathrm{kg}}{\mathrm{s\,m}}$ at the end of a cultivation. Changes in viscosity are negligible for the cultivation presented in this work. The density ranges from $997\ \frac{\mathrm{kg}}{\mathrm{m}^3}$ to $1029\ \frac{\mathrm{kg}}{\mathrm{m}^3}$ and may also be neglected. Surface tension between the continuous and the dispersed phase varies much from $0.0735\ \frac{\mathrm{kg}}{\mathrm{s}^2}$ to $0.04\ \frac{\mathrm{kg}}{\mathrm{s}^2}$.

6.3 Sequencing

An up-front fluid dynamics simulation gives initial values for the first sequence of growth. As mentioned in section 6.1, a crucial part of the sequen-

tial co-simulation is the decision about a new sequence. When changes in growth are significant relative to a specified comparative value there is need to re-simulate the flow field.

The flow field will change considerably when the change in volume is high. As first criterion for assessment the volume change may be related to the volume at the beginning of a cultivation.

$$crit_1 = \frac{\Delta V}{V_{0,s}} = \frac{|V - V_{0,s}|}{V_{0,s}} \tag{6.6}$$

For volume changes due to changing operation level given in section 2.11, the values for criterion $crit_1$ after six, twelve and eighteen hours are 0.0414, 0.0406 and 0.0382. No parameter study has been performed with respect to $crit_1$. As educated guess, values of $crit_1$ may be limited to 0.1 or to 0.05 in order to keep resulting errors low.

Major changes in growth as second criterion influence the oxygen sink representing the biomass in the continuous phase. Following equation 6.5, the criterion is composed of the oxygen uptake rate q_{O_2} and the biomass concentration X. These variables differ for every volume element. An up-front calculation of growth for all elements of the reduced data set for determination of sequence lengths is computationally too expensive. Therefore, growth is simulated for the entire reactor treated as one single element. The product of q_{O_2} and X from this calculation is taken to decide about sequence lengths.

$$crit_2 = \frac{|q_{O_2} X - q_{O_2,0,s} X_{0,s}|}{q_{O_2,0,s} X_{0,s}} \tag{6.7}$$

After six, twelve and eighteen hours, values for criterion $crit_2$ are 0.2131, 0.0304 and 0.0245, respectively. A parameter study for this criterion has not been performed. An educated guess again for this criterion also limits the value to 0.1 or even 0.05. The value for $crit_2$ between the first and the second sequence exceeds the guessed limit. Consequently, the sequence should have been subdivided.

Restriction of criteria $crit_1$ and $crit_2$ to a certain value defines a decision system. One of the criteria always limits first and therefore decides about a new sequence. The system ensures that either major changes in fluid dynamics or changes in growth initiate a new sequence. **Table 6.2** gives typical values.

Major objective of this work has been the development of a simulation framework for coupled simulations of fluid dynamics and biological growth.

Table 6.2: Decision criteria for sequencing

Criterion	Value	Decision Character
$crit_1$	≤ 0.1	fluid dynamics
$crit_2$	≤ 0.1	yeast growth

Simulation practice has shown that computational restrictions are still limiting. As a consequence, large scale systems cannot be simulated without violencing a number of best practice guidelines. The defined decision criteria have not been applied so far. For exemplary calculations, the entire cultivation process has been divided into four sequences equally spaced in time (chapter 7).

6.4 Data Reduction

For the simulation of fluid dynamics, the reactors are discretized into a few hundred thousand finite volume elements. The output from CFX gives the relevant set of data for each volume element. Due to computational restrictions for simulation of growth on large domains, a self-organizing maps (SOM) algorithm [74] reduces the data set to several thousand elements. This algorithm is called neural gas (NG) [88]. The reduced set is applied to sequences of growth simulation only. Meshes for sequences of fluid dynamics simulation are not affected.

Self-organizing maps are un-supervised artificial neural networks. Their advantage is that they do not need explicit training data for organization of the network. In general, a number of neurons has to be distributed on the input space to optimally represent it. Different metrics are the basis for the subsequent redistribution of the neurons. In problems where information about input space dimensionality is not available different approaches such as the neural gas algorithm have to be applied.

A fundamental application of this neural network approach is vector quantization in terms of clustering of data as well as data reduction and data compression [74, 109]. In many cases restrictions due to computational power or storage space require data compression with little related errors [14].

In general, an input space is mapped to a neural network. Beside other parameters the number of neurons determines the computational cost. On the one hand, few neurons will not fulfill requirements of adequate description of the input space. On the other hand, too many neurons increase computational cost and do not reach compression requirements.

6.4.1 Neural Gas Algorithm

A specified number of neurons is randomly distributed over the input space. These neurons will subsequently be shifted such that they reach positions where the distance between neurons is maximized but they still reflect the input space distribution. The latter effect is produced by the repelling coupling of the neurons. The averaged change in space of a neuron is similar to the movement of gas molecules in their potential well. These two effects have named the algorithm [88].

It has been shown that the density distribution of neurons is non linear proportional to the element distribution in the input space. Relative spatial element density is identical. The data compression therefore is optimally distribution conservative [88, 14].

Detailed information about the algorithm and its implementation can be found in the related literature [88, 14]. For use in Matlab a toolbox with different SOM implementations as well as with a neural gas implementation is available in the Internet.

http://www.cis.hut.fi/projects/somtoolbox/

From this toolbox the implementation of the neural gas algorithm has been used for data reduction in this work. The following section gives a simple two-dimensional example for a plane in the reactor. The selection of algorithm parameters is based upon this example and some assumptions.

6.4.2 Neural Gas 2D Example

This example gives an illustrative impression of data reduction by the neural gas algorithm. The variation of epochs has been performed in order to compromise between reduced computational cost and acceptable distribution quality. Influences of distribution quality on results of the sequential co-simulation have not been determined.

Table 6.3: Neural gas example settings and results

Neurons	Epochs	Training Steps	Time in s
1000	1	12,122	101
1000	5	60,610	158
1000	10	121,220	369
1000	50	606,100	1,964
1000	100	1,212,200	7,202

A set of data represents 12122 finite volume elements in a mid plane of the reactor. It is the objective to reduce the vector length of the set to a representative number of 1000. Varying the number of training epochs influences the quality of representation of original data. The product of the vector length of the input space data set and the number of epochs gives the related number of training steps performed by the neural gas algorithm. **Table 6.3** summarizes the example settings. The calculations have been performed on a Windows XP PC with a single Pentium 4 processor with the clock rate of 3.2 GHz and 1024 MB RAM.

While results for ten epochs still show bands and uneven distributions, results for 50 and 100 epochs adequately represent the original distribution (**figure 6.2**). The quality of the distribution does not change much from doubling the number of epochs from 50 to 100. Nevertheless, CPU time increases significantly wherefore 50 epochs will be used as standard.

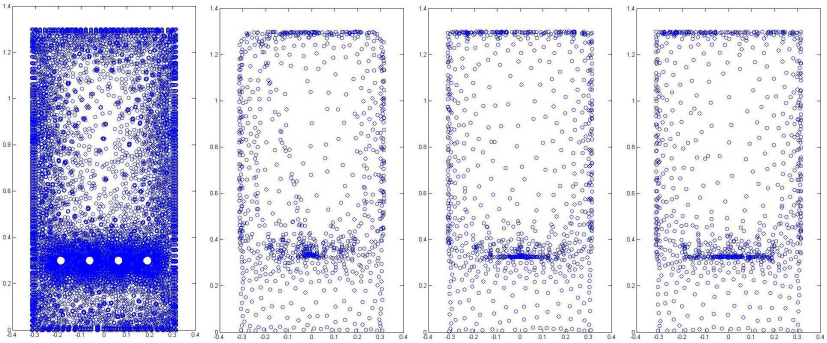

(a) Original Data (b) Ten Epochs (c) 50 Epochs (d) 100 Epochs

Figure 6.2: Neural gas example, the original data set and with 1000 neurons after ten, 50 and 100 epochs

6.5 Model Assumptions

In addition to the afore mentioned properties and adjustments of simulations, model assumptions are listed below. These assumptions are a substantial component of the developed simulation framework.

- Growth does not directly influence fluid dynamics.
- Yeast is equally distributed.
- Sinks and sources are constant for a given sequence length.
- Errors introduced by the method of simulation do not influence central deductions.
- Simulations do neither account for feed nor for cooling circuit.
- Temperature is kept constant.
- Limited growth in the cooling circuit has a negligible influence on the overall yield.

Chapter 7

Sequential Co-simulation Example

It has been the declared aim to develop a method for combination of multiphase computational fluid dynamics and simulation of biological growth. The tool is meant to support optimization of reactors and processes.

Oxygen concentration in the dispersed phase is of major interest. It is expected to show highest values close to the gas inlet decreasing with increasing distance in flow direction. Different bubble classes behave in the same way. The level of decrease in oxygen concentration in the dispersed phase depends upon oxygen concentration in the liquid and with it upon oxygen consumption by yeast cells. Oxygen consumption by yeast cells is directly proportional to yeast concentration.

Figure 7.1 shows the simulated oxygen concentration in all three bubble classes. From left to right the contour plots show class three with $d_{\beta,3} = 0.8$mm, class two with $d_{\beta,2} = 3$mm and class one with $d_{\beta,1} = 80$mm.

Small bubbles rise slowly. They have a high volume specific surface area. As a consequence, there is much time and area for mass transfer. Decrease in oxygen concentration of these bubbles reaches the highest level (figure 7.1 left). Highest loss of about 20 % is reached at the top outer edge of the reactor. On the one hand, following the concept of liquid phase up- and down-flow regions, the lowest concentration level is expected to be below the jet tubes. On the other hand, liquid phase down-flow region at the

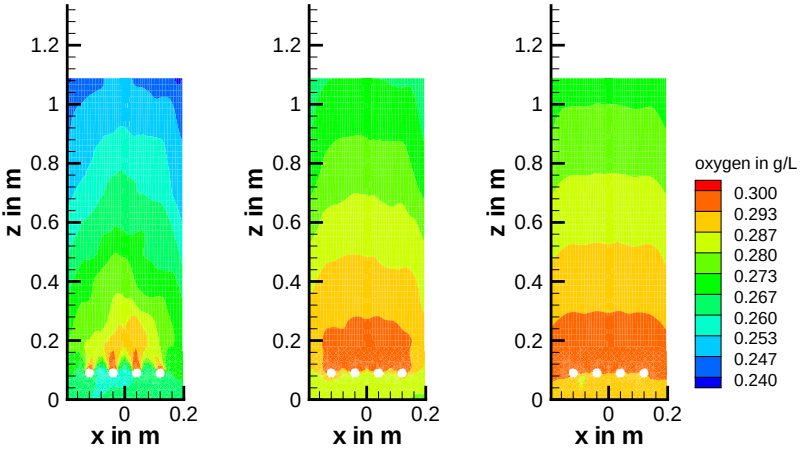

Figure 7.1: Simulated oxygen concentration in the gas phase with different bubble size classes on plane $y = 0$ at start of cultivation, bubble diameters of size classes from left to right: $d_{\beta,3} = 0.8\,\text{mm}$, $d_{\beta,2} = 3\,\text{mm}$ and $d_{\beta,1} = 80\,\text{mm}$, time average

cylinder jacket entrains bubbles from the up-flow region downwards. Bubbles do not completely follow liquid phase up- and down-flow. This is why lowest concentration values are not reached below the gassing system.

Large bubbles rise fast and almost directly to the reactor top. They have a low volume specific surface area. As a consequence, oxygen concentration in the bubbles stays at higher levels (figure 7.1 right). Maximal loss of about 10 % is reached at the top outer edge. The medium sized class shows oxygen

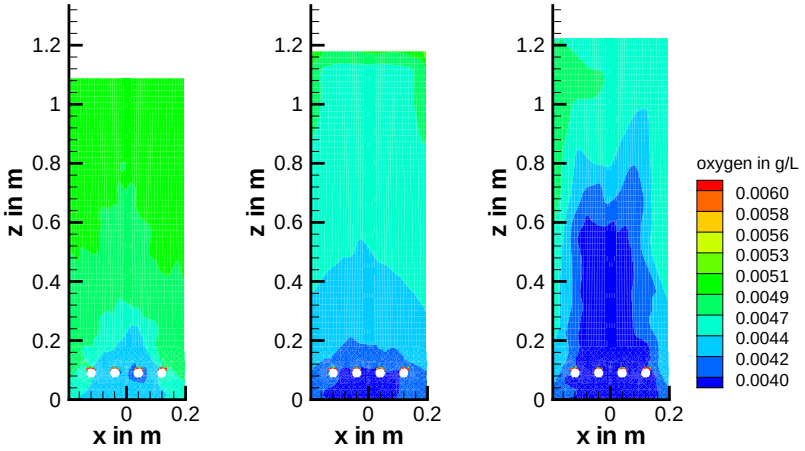

Figure 7.2: Simulated oxygen concentration in water on plane $y = 0$ from left to right: at start of cultivation, after 12 and 18 hours, time average

concentrations in between. Optimization target may be an optimum bubble size compromising the behavior of mixing and mass transfer.

The liquid side oxygen concentration is the second variable of interest. **Figure 7.2** shows simulated values as time average at the beginning of the cultivation, after 12 and 18 hours, from left to right.

Assuming homogenous oxygen consumption, the flow field directly informs about areas of lowest oxygen concentration. In average, fluid elements follow one after another up- and down-flow region. Relating this flow behavior to oxygen support by dispersed phases as discussed above, areas of lowest

liquid side oxygen concentration have to be below and around the gassing system.

Rising yeast concentrations during cultivation increase oxygen consumption. The unchanged gas flow rate worsens oxygen support for yeast cells. This effect becomes obvious in figure 7.2. Here, lowest values of oxygen concentration range about 50 % of oxygen saturation concentration. Consequently, sufficient oxygen support guarantees oxidative growth without production of ethanol. Adequate adjustment of gas support is a related topic of optimization.

Comparing the methods of sequential co-simulation and growth simulation without consideration of fluid dynamics (chapter 5), the sequential method denotes significantly increased workload. To be justified, it has to enhance quality of results in a similar manner. Biomass yield is the major target in mass production. For this reason, simulations have to correctly predict this target.

Figure 7.3 shows biomass dry weight concentration of experimental results, of growth simulations and of the sequential co-simulation. For the sequential method, only distinct points for zero, six, 12 and 18 hours of cultivation are available. The dashed line simply supports visualization. The sequential co-simulation very well predicts yeast concentration.

The growth simulation without consideration of fluid dynamics systematically over-predicts biomass concentration beginning about nine hours after start of cultivation. Decisions about the reactor system and the process based upon wrong predictions may permanently increase operation costs. This is why enhancement of prediction quality is very important for optimization in mass production.

Results from the sequential co-simulation are almost identical to experimental results. The method slightly over-predicts biomass dry weight concentration beginning from 15 hours after start of cultivation. The relative error at the end of cultivation is below three percent. The precision is impressive even though only a few and long sequences have been used.

The method has been applied to a small system. In a promising way it enhances target prediction. Anyhow, the sequential co-simulation shows finite predominancy in comparison to a growth simulation without consideration of fluid dynamics. The effect is expected to be significant for larger systems as used in industry. Application to huge reactor systems still suffers from limited computational resources. Size of volume elements in computational fluid

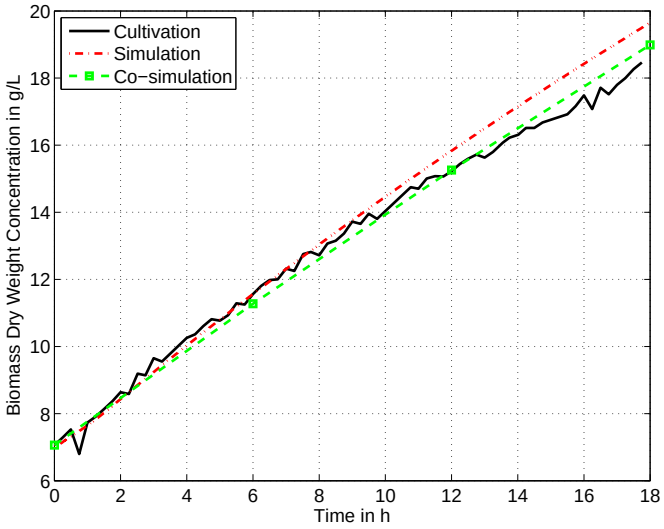

Figure 7.3: Biomass dry weight concentration in fed-batch cultivation, growth simulation without consideration of fluid dynamics and sequential co-simulation

dynamics cannot significantly be decreased without giving rise to numbers of volume elements in the order of billions.

Nevertheless, a first trial in roughly simulating systems of industrial size is to increase element size in fluid dynamics simulations [144]. This obviously increases discretization error. Depending on the assignment the general prediction of flow field characteristics may still be sufficient.

At the present time, the sequential co-simulation as presented is the most realistic and feasible way for combined simulation of computational fluid dynamics and biological growth.

Chapter 8

Summary and Future Prospects

It has been the scope of this work to develop a basic method for coupled simulation of slowly reacting systems in multiphase flow. The example of this work has been baker's yeast production.

Time scales in fluid dynamics of milli seconds or seconds and time scales in biological growth of hours to days differ significantly from each other. Therefore, direct coupling of fluid dynamics and biological growth is not feasible. This holds especially true with respect to relevant real time and relevant reactor size.

These are the reasons why the method of sequential co-simulation has been proposed. Every sequential co-simulation consists of modules for fluid dynamics and biological growth. Defined interfaces couple the modules. The method has been implemented in commercial codes. CFX by Ansys has been used for computational fluid dynamics. Matlab and Simulink have been used for implementation of a biological growth model. Both modules are iteratively or sequentially applied in the sequential method, giving its name.

For sequences of growth simulation the set of volume elements is reduced using the neural gas algorithm. Consequently, computational demand for growth simulations significantly decreases.

The modules have been validated separately with experimental data. Experimental data for both, fluid dynamics and yeast cultivation, have been determined in the same system.

Axial liquid velocities have been determined with a pitot tube as well as with a developed strain gauge cantilever probe. Results from the strain gauge cantilever probe still need to be enhanced in quality. Measurements from the pitot tube are good. Data from literature has additionally been used for validation. The flow field information has been used to validate simulation results with respect to sufficiently fine grids and time steps. The time step has been set to $\Delta t = 0.005\,\mathrm{s}$.

A growth model from literature has been implemented and modified in order to account for relevant mass transfer options needed in the framework of sequential co-simulation. In future work growth simulations may be parallelized.

Crucial for success of the sequential co-simulation is the sequence length. A decision system has been suggested consisting of two criteria, one for changes in fluid dynamics and one for changes in biological growth. It has carefully to be tested. For increase in automation, a decision system has to be implemented. Furthermore, interfaces between the modules shall be simplified and automated.

A sequential co-simulation has been performed for the mentioned reactor system. The method has proven significant enhancement of target prediction quality in comparison to growth simulations without consideration of fluid dynamics. Biomass dry weight concentration has been the target variable.

Application of the proposed method to industrial reactor systems is not feasible at the present time. Computational power and hardware restrictions limit application of computational fluid dynamics for multiphase systems to relatively small size. Use for optimization problems has to be demonstrated.

Any model included in the sequential framework has to be improved to optimally represent reality. For multiphase flow simulations bubble behavior, interphase drag forces, mass transfer and turbulence may stay in the foreground.

In sum the sequential co-simulation has been proposed as powerful tool which can be applied to generally simulate slow chemical or biological reactions in multiphase flow systems.

References

[1] *ANSYS CFX-Solver Theory Guide: ANSYS CFX Release 11.0.* ANSYS, Canonsburg, 2006. 17

[2] S. S. Alves, S. P. Orvalho, and J. M. T. Vasconcelos. Effect of bubble contamination on rise velocity and mass transfer. *Chemical Engineering Science*, 60:1–9, 2005. 29

[3] G. F. Andrews, J. P. Fonta, E. Marrotta, and P. Stroeve. The Effects of Cells on Oxygen Transfer Coefficients I: Cell Accumulation around Bubbles. *The Chemical Engineering Journal*, 29:B39–B46, 1984. 30

[4] G. H. Aylward and T. J. V. Findlay. *Datensammlung Chemie in SI-Einheiten.* VCH Verlagsgesellschaft, Physik-Verlag, Weinheim, 2nd edition, 1986. 31

[5] R. K. Bajpai and M. Reuss. Coupling of Mixing and Microbial Kinetics for Evaluating the Performance of Bioreactors. *The Canadian Journal of Chemical Engineering*, 60:384–392, 1982. 14

[6] S. Barth. *Entwicklung eines hochauflösenden Geschwindigkeitssensors.* PhD thesis, Universität Oldenburg, Oldenburg, July 2004. 42, 45

[7] S. Barth, H. Koch, A. Kittel, J. Peinke, J. Burgold, and H. Wurmus. Laser-Cantilever-Anemometer: A new high resolution sensor for air and liquid flows. 2005. 44, 45

[8] E. Bartholome, H. H. Mayer, and H. W. Schmidt. Aufbau und Einsatz eines Computerprogramms zur Beschreibung chemischer Umsetzungen in Blasensäulen. *Chemie-Ingenieur-Technik*, 45, 15:974–979, 1973. 15

[9] M. Bauer and G. Eigenberger. A concept for multi-scale modeling of bubble columns and loop reactors. *Chemical Engineering Science*, 54:5109–5117, 1999. 15

[10] M. Bauer and G. Eigenberger. Multiscale modeling of hydrodynamics, mass transfer and reaction in bubble column reactors. *Chemical Engineering Science*, 56:1067–1074, 2001. 15

[11] K. Bech. Dynamic simulation of a 2Dbubble column. *Chemical Engineering Science*, 60:5294–5304, 2005. 8, 13

[12] S. Becker, H. De Bie, and J. Sweeney. Dynamic flow behaviour in bubble columns. *Chemical Engineering Science*, 54:4929–4935, 1999. 42

[13] E. Bergander. *Biochemie und Technologie der Hefe*, volume 59 of *Technische Fortschrittberichte*. Verlag von Theodor Steinkopff, Dresden, Leipzig, 1959. 6, 56

[14] A. Berger. *Zur Theorie selbstorganisierender und topologieerhaltender Neuronaler Netze und deren Evaluation mittels komplexer anästhesiologischer Signaturen des Narkose-EEG*. PhD thesis, Technische Universität Clausthal, Clausthal, December 1999. 79, 80

[15] F. Bertola, G. Baldi, D. Mechisio, and M. Vanni. Momentum transfer in a swarm of bubbles: Estimates from fluid-dynamic simulations. *Chemical Engineering Science*, 59:5209–5215, 2004. 9, 10, 24

[16] F. Bertola, M. Vanni, and G. Baldi. Application of Computational Fluid Dynamics to Multiphase Flow in Bubble Columns. *International Journal of Chemical Reactor Engineering*, 1, A3:1–14, 2003. 9, 10, 14

[17] J. Beyersdorf. *Verhalten von Luftblasen und Sedimenten in Blasensäulen in Abhängigkeit vom Salzgehalt im Wasser*. PhD thesis, Universität Hannover, Hannover, 1997. 21

[18] M. R. Bhole, J. B. Joshi, and D. Ramkrishna. CFD simulation of bubble columns incorporating population balance modeling. *Chemical Engineering Science*, 63:2267–2282, 2008. 10

[19] O. Borchers. *Zweiphasen-Particle-Tracking-Velocimetry (PTV) zur detailierten Analyse der Hydrodynamik von Blasensäulenreaktoren.* PhD thesis, Universität Stuttgart, Stuttgart, August 2002. 43

[20] O. Borchers, C. Busch, A. Sokolichin, and G. Eigenberger. Applicability of the standard k-epsilon turbulence model to the dynamic simulation of bubble columns. Part II: Comparison of detailed experiments and flow simulations. *Chemical Engineering Science*, 54:5927–5935, 1999. 8, 42

[21] S. Bordel, R. Mato, and S. Villaverde. Modeling of the evolution with length of bubble size distributions in bubble columns. *Chemical Engineering Science*, 61:3663–3673, 2006. 20

[22] C. Boyer, Duquenne A.-M., and G. Wild. Measuring techniques in gas-liquid and gas-liquid-solid reactors. *Chemical Engineering Science*, 57:3185–3215, 2002. 43, 46

[23] H. Brauer. *Grundlagen der Einphasen- und Mehrphasenströmungen.* Grundlagen der Chemischen Technik – Verfahrenstechnik der chemischen und verwandter Industrien. Verlag Sauerländer, Aarau, 1971. 6, 20, 23

[24] H. Brauer. Turbulenz in mehrphasigen Strömungen. *Chemie-Ingenieur-Technik*, 51, 10:934–948, 1979. 10

[25] H. Brauer and H. Thiele. Bewegung von Partikelschwärmen. *Chemie-Ingenieur-Technik*, 45, 13:909–912, 1973. 21

[26] H. H. Bruun. *Hot-Wire Anemometry: Principles and Signal Analysis.* Oxford University Press, Oxford, New York, 1995. 44

[27] A. D. Burns, T. Frank, I. Hamill, and J. M. Shi. The Favre Averaged Drag Model for Turbulent Dispersion in Eulerian Multi-Phase Flows. In *5th International Conference on Multiphase Flow, ICMF'04*, pages 1–17, Yokohama, Japan, June 2004. 12

[28] Thomas Börner. *Laser-Doppler- und Heiß-Film-Anemometrie zur Ermittlung von Strömungsstrukturen in Blasensäulen, Neigung von Blasensäulen, Neigungsproblem.* PhD thesis, Universität Dortmund, Dortmund, December 1983. 43, 44, 45, 49

[29] F. Camacho Rubio, A. Sanchez Miron, M. C. Ceron Garcia, F. Garcia Camacho, E. Molina Grima, and Y. Chisti. Mixing in bubble columns: A new approach for characterizing dispersion coefficients. *Chemical Engineering Science*, 59:4369–4376, 2004. 6

[30] L. Cammarata, P. Lettieriy, G. D. M. Micalez, and D. Colman. 2D and 3D CFD Simulations of Bubbling Fluidized Beds Using Eulerian-Eulerian Models. *International Journal of Chemical reactor Engineering*, 1, A48:1–15, 2003. 8

[31] C. Chen and L.-S. Fan. Discrete Simulation of Gas-Liquid Bubble Columns and Gas-Liquid-Solid Fluidized Beds. *AIChE Journal*, 50, 2:288–301, 2004. 21

[32] P. Chen, J. Sanyal, and M. P. Dudukovic. Numerical simulation of bubble columns flows: effect of different breakup and coalescence closures. *Chemical Engineering Science*, 60:1085–1101, 2005. 9, 10, 11, 12, 14

[33] R. C. Chen and L.-S. Fan. Particle Image Velocimetry for Characterizing the Flow Structure in Three-Dimensional Gas-Liquid-Solid Fluidized Beds. *Chemical Engineering Science*, 47, 13/14:3615–3622, 1992. 42, 43

[34] W. Chen, T. Hasegawa, A. Tsutsumi, and K. Otawara. Scale-up effects on the time-averaged and dynamic behavior in bubble column reactors. *Chemical Engineering Science*, 56:6149–6155, 2001. 6

[35] M. Y. Chisti. *Airlift Bioreactors*. Elsevier Applied Science, London, New York, 1989. 20, 21

[36] D. Claes. *Numerische Simulation von instationären Strömungen mit freien Oberflächen am Beispiel ablösender und aufsteigender Blasen*. PhD thesis, Ruhr-Universität Bochum, Bochum, February 1990. 20

[37] R. Clift, J. R. Grace, and M. E. Weber. *Bubbles, drops, and particles*. Academic Press, New York, 1978. 23, 24, 38

[38] R. Courant, K. Friedrichs, and H. Lewy. On the Partial Difference Equations of Mathematical Physics. *IBM Journal*, March:215–234, March 1967. 37

[39] D. Darmana, N. G. Deen, and J. A. M. Kuipers. Detailed modeling of hydrodynamics, mass transfer and chemical reactions in a bubble column using a discrete bubble model. *Chemical Engineering Science*, 60:3383–3404, 2005. 15

[40] D. Darmana, R. L. B. Henket, N. G. Deen, and J. A. M. Kuipers. Detailed modelling of hydrodynamics, mass transfer and chemical reactions in a bubble column using a discrete bubble model: Chemisorption ofCO2 into NaOH solution, numerical and experimental study. *Chemical Engineering Science*, 62:2556–2575, 2007. 13, 15

[41] W.-D. Deckwer. *Reaktionstechnik in Blasensäulen*. Otto Salle Verlag, Verlag Sauerländer, Frankfurt am Main, Aarau, 1st edition, 1985. 38

[42] W.-D. Deckwer, R. Burckhart, and G. Zoll. Mixing and Mass Transfer in Tall Bubble Columns. *Chemical Engineering Science*, 29:2177–2188, 1974. 30

[43] E. Delnoij, J. A. M. Kuipers, and W. P. M. van Swaaij. Computational fluid dynamics applied to gas-liquid contactors. *Chemical Engineering Science*, 52, 21/22:3623–3638, 1997. 8, 9

[44] E. Delnoij, F. A. Lammers, J. A. M. Kuipers, and W. P. M. van Swaaij. Dynamic simulation of dispersed gas-liquid two-phase flow using a discrete bubble model. *Chemical Engineering Science*, 52, 9:1429–1458, 1997. 8

[45] K. M. Dhanasekharan, J. Sanyl, A. Jain, and A. Haidari. A generalized approach to model oxygen transfer in bioreactors using population balances and computational fluid dynamics. *Chemical Engineering Science*, 60:213–218, 2005. 13

[46] M. T. Dhotre, K. Ekambara, and J. B. Joshi. CFD simulation of sparger design and height to diameter ratio on gas hold-up profiles in bubble column reactors. *Experimental Thermal and Fluid Science*, 28:407–421, 2004. 6

[47] M. T. Dhotre and B. L. Smith. CFD simulation of large-scale bubble plumes: Comparisons against experiments. *Chemical Engineering Science*, 62:6615–6630, 2007. 12

[48] M. T. Dhotre, B. L. Smith, and B. Niceno. CFD simulation of bubbly flows: Random dispersion model. *Chemical Engineering Science*, 62:7140–7150, 2007. 12

[49] H. Dziallas. *Lokale Phasengehalte in zwei- und dreiphasig betriebenen Blasensäulenreaktoren*. PhD thesis, TU Braunschweig, Braunschweig, in Hempel D. C. (editor): ibvt-Schriftenreihe Vol. 10, FIT-Verlag, Paderborn, December 1999. 8

[50] H. Eckelmann. *Einführung in die Strömungsmesstechnik*, volume 74 of *Leitfäden der angewandten Mathematik und Mechanik*. Teubner, Stuttgart, 1997. 47, 48

[51] J. Ellenberger and R. Krishna. Improving mass transfer in gas liquid dispersions by vibration excitement. *Chemical Engineering Science*, 57:4809–4815, 2002. 30

[52] F. Elstner. *Untersuchungen zum Stoffübergang von Sauerstoff aus Luft in wässrige Lösungen*. PhD thesis, Universität Dortmund, Dortmund, October 1978. 38

[53] F. Emde. *TRG 18000 – New high-performance aerator*. Heinrich Frings GmbH & Co. KG, Bonn, 2004. 2, 6

[54] J. H. Enß. *Einfluss der Viskosität auf Blasenströmungen*. PhD thesis, TU Braunschweig, Braunschweig, in Hempel D. C. (editor): ibvt-Schriftenreihe Vol. 25, FIT-Verlag, Paderborn, 2005. 8, 10

[55] L.-S. Fan and K. Tsuchiya. *Bubble Wake Dynamics in Liquids and Liquid-Solid Suspensions*. Butterworth-Heinemann Series in Chemical Engineering. Butterworth-Heinemann, Boston, London, Singapore, Sydney, Toronto, Wellington, 1990. 20

[56] K. Franz. *Untersuchungen zur Turbulenzstruktur in Blasensäulen mittels einer neu entwickelten richtungsspezifieschen Heißfilm-Anemometertechnik*. PhD thesis, Universität Dortmund, Dortmund, July 1983. 44

[57] C.-C. Fu, S.-Y. Lu, Y.-J. Hsu, G.-C. Chen, Y.-R. Lin, and W.-T. Wu. Superior mixing performance for airlift reactor with a net draft tube. *Chemical Engineering Science*, 59:3021–3028, 2004. 6

[58] F. Garcia-Ochoa and E. Gomez. Theoretical prediction of gas-liquid mass transfer coefficient, specific area and hold-up in sparged stirred tanks. *Chemical Engineering Science*, 59:2489–2501, 2004. 29

[59] P. Giesecke. *Dehnungsmessstreifentechnik: Grundlagen und Anwendungen in der industriellen Messtechnik.* Messen – Steuern – Regeln. Vieweg, Braunschweig, Wiesbaden, 1994. 120

[60] O. Gnotke. *Experimentelle und theoretische Untersuchungen zur Bestimmung von veränderlichen Blasengrößen und Blasengrößenverteilungen in turbulenten Gas-Flüssigkeits-Strömungen.* PhD thesis, TU Darmstadt, Darmstadt, July 2004. 44

[61] O. Gnotke, H. Benk, and R. Loth. Experimental study on the number density distribution function in turbulent bubbly flows with coalescence and break-up. *Experimental Thermal and Fluid Science*, 27:803–816, 2003. 44

[62] P. Grassmann. *Physikalische Grundlagen der Verfahrenstechnik.* Otto Salle Verlag, Verlag Sauerländer, Frankfurt am Main, Aarau, 1983. 46

[63] J. Hallensleben. *Simultaner Stoffaustausch von CO_2 und Sauerstoff an Einzelblasen und in Blasenschwärmen.* PhD thesis, Universität Hannover, Hannover, June 1980. 29, 32

[64] J. J. Heijnen and K. Vantriet. Mass Transfer, Mixing and Heat Transfer Phenomena in Low Viscosity Bubble Column Reactors. *The Chemical Engineering Journal*, 28:B21–B42, 1984. 30

[65] H. Herwig. *Strömungsmechanik: Eine Einführung in die Physik und die mathematische Modellierung von Strömungen.* Springer, Berlin, Heidelberg, 2002. 18, 25, 26

[66] W. Hilgert. *Charakterisierung der Gasphasenströmung in Blasensäulen mit Hilfe eines Ultraschall-Doppler-Messverfahrens.* PhD thesis, Universität Erlangen-Nürnberg, Erlangen, July 1985. 45, 49

[67] J. H. Hills. Radial non-uniformity of velocity and voidage in a bubble column. *Transactions of the Instituation of Chemical Engineers*, 52:1–9, 1974. 50, 51, 52, 118, 119

[68] C. L. Hyndman, F. Larachi, and C. Guy. Understanding gas-phase hydrodynamics in bubble columns: a convective model based on kinetic theory. *Chemical Engineering Science*, 52, 1:63–77, 1997. 9

[69] Y. Jiang, J. Guo, and M. H. Al-Dahhan. Multiphase Flow Packed-Bed Reactor Modeling: Combining CFD and Cell Network Model. *Industrial & Engineering Chemistry Research*, 44:4940–4948, 2005. 15

[70] J. Kantorek. *Mischvorgänge in Blasensäulenreaktoren unter Berücksichtigung deterministischer und stochastischer Transportmechanismen.* PhD thesis, Universität Dortmund, Dortmund, 1988. 46, 49

[71] I Kataoka and A. Serizawa. Basic Equations of Turbulence in Gas-Liquid Two-Phase Flow. *International Journal of Multiphase Flow*, 15, 5:843–855, 1989. 11, 27

[72] Y. Kawase, B. Halard, and M. Moo-Young. Theoretical Prediction of Volumetric Mass Transfer Coefficients in Bubble Columns for Newtonian and Non-Newtonian Fluids. *Chemical Engineering Science*, 42:1609–1617, 1987. 12

[73] M. Koebe. *Numerische Simulation aufsteigender Blasen mit und ohne Stoffaustausch mittels der Volume of Fluid (VOF) Methode.* PhD thesis, Universität Paderborn, Paderborn, August 2004. 13, 20, 21, 38

[74] T. Kohonen. *Self-Organizing Maps*, volume 30 of *Springer Series in Information Science*. Springer-Verlag, Berlin, Heidelberg, 3rd edition, 2001. 79

[75] N. I. Kolev. *Multiphase Flow Dynamics 1, Fundamentals*, volume 1. Springer Verlag, Berlin Heidelberg New York, 2002. 7

[76] T. Korte. *Messtechnik zur Charakterisierung von Blasensäulenreaktoren: Das Ultraschallimpuls-Doppler-Anemometer.* PhD thesis, Universität Hannover, Hannover, 1986. 45

[77] R. Krishna, M. I. Urseanu, J. M. van Baten, and J. Ellenberger. Influence of scale on the hydrodynamics of bubble columns. *Chemical Engineering Science*, 54:4903–4911, 1999. 46, 50

[78] R. Krishna, M. I. Urseanu, J. M. van Baten, and J. Ellenberger. Rise velocity of a swarm of large gas bubbles in liquids. *Chemical Engineering Science*, 54:171–183, 1999. 8, 21

[79] R. Krishna and J. M. van Baten. Rise Characteristics of Gas Bubbles in a 2d Rectangular Column: VOF Simulations vs Experiments. *International Communications on Heat and Mass Transfer*, 26, 7:965–974, 1999. 9

[80] R. Krishna and J. M. van Baten. Mass transfer in bubble columns. *Catalysis Today*, 79–80:67–75, 2003. 13

[81] R Krishna, J. M. van Baten, and M. I. Urseanu. Three-phase Eulerian simulations of bubble column reactors operating in the churn-turbulent regime: a scale up strategy. *Chemical Engineering Science*, 55:3275–3286, 2000. 9

[82] A. A. Kulkarni. Lift force on bubbles in a bubble column reactor: Experimental analysis. *Chemical Engineering Science*, 63:1710–1723, 2008. 12

[83] A. A. Kulkarni, K. Ekambara, and J. B. Joshi. On the Development of Flow Pattern in a Bubble Column Reactor: Experiments and CFD. *Chemical Engineering Science*, 62:1049–1072, 2007. 14, 42

[84] S. Lain, D. Bröder, M. Sommerfeld, and M. F. Göz. Modell hydrodynamics and turbulence in a bubble column using the Euler-Lagrange procedure. *International Journal of Multiphase Flow*, 28:1381–1407, 2002. 11, 28

[85] D. J. Lee, X. Luo, and L.-S. Fan. Gas disengagement technique in a slurry bubble column operated in the coalesced bubble regime. *Chemical Engineering Science*, 54:2227–2236, 1999. 43

[86] F. Lehr and D. Mewes. A transport equation for the interfacial area density applied to bubble columns. *Chemical Engineering Science*, 56:1159–1166, 2001. 8

[87] Z. Liu and Y. Zheng. PIV study of bubble rising behavior. *Powder Technology*, 168:10–20, 2006. 43

[88] T. Martinetz. *Selbstorganisierende neuronale Netzwerkmodelle zur Bewegungssteuerung*. PhD thesis, Technische Universität München, München, May 1992. 79, 80

[89] A. Mersmann. Auslegung und Maßstabsvergrößerung von Blasen- und Tropfensäulen. *Chemie-Ingenieur-Technik*, 49, 9:679–691, 1977. 6

[90] D. Mewes and D. Wiemann. Two-Phase Flow with Mass Transfer in Bubble Columns. *Chemical Engineering and Technology*, 26:862–868, 2003. 11, 13, 39

[91] V. Michele. *CFD Modeling and Measurement of Liquid Flow Structure and Phase Holdup in Two- and Three-Phase Bubble Columns*. PhD thesis, TU Braunschweig, Braunschweig, in Hempel D. C. (editor): ibvt-Schriftenreihe Vol. 13, FIT-Verlag, Paderborn, March 2002. 8

[92] I. Michiyoshi and A. Serizawa. Turbulence in Two-phase Bubbly Flow. *Nuclear Engineering and Design*, 95:253–267, 1986. 10

[93] A. A. Mouza, G. K. Dalakogulou, and S. V. Paras. Effect of liquid properties on the performance of bubble column reactors with fine pore spargers. *Chemical Engineering Science*, 60:1465–1475, 2005. 5, 7

[94] R. F. Mudde and O. Simonin. Two- and three-dimensional simulations of a bubble plume using a two-fluid model. *Chemical Engineering Science*, 54:5061–5069, 1999. 27

[95] R. F. Mudde and H. E. A. Van Den Akker. Dynamic behaviour of the flow field of a bubble column at low to moderate gas fractions. *Chemical Engineering Science*, 54:4921–4927, 1999. 42

[96] N. N. *Frings TRG Mixing and Aeration Systems for Gas/Liquid Reactions*. Frings, Bonn, 2004. 6

[97] E. Nagy, B. Mayr, and A. Moser. Bioprocess Scale-Up Using a Structured Mixing Model. *Computers Chemical Engineering*, 18:S663–S667, 1994. 14

[98] W. Nitsche. *Strömungsmesstechnik*. Springer-Lehrbuch. Springer-Verlag, Berlin, Heidelberg, New York, 1994. 44, 46, 47, 49

[99] F. Oehme and P. Schuler. *Gelöst-Sauerstoff-Messung: Physikalische Grundlagen, Mess- und Analysentechnik, Anwendungen.* Dr. Alfred Hüthig Verlag, Heidelberg, 1983. 30, 31

[100] H. Oertel and E. Laurien. *Numerische Strömungsmechanik.* Strömungsmechanik. Vieweg, Braunschweig, Wiesbaden, 2nd edition, 2003. 16

[101] E. Olmos, C. Gentric, and N. Midoux. Numerical description of flow regime transitions in bubble column reactors by a multiple gas phase model. *Chemical Engineering Science*, 58:2113–2121, 2003. 9, 10, 11, 28

[102] G.-P. Ostermeyer. *Mechanik III.* Number 5 in Braunschweiger Schriften zum Maschinenbau. Fachbereich der Technischen Universität Braunschweig, Braunschweig, 2001. 111

[103] P. Painmanakul, K. Loubiere, G. Hebrard, M. Mietton-Peuchot, and M. Roustan. Effect of surfactants on liquid side mass transfer coefficients. *Chemical Engineering Science*, 60:6480–6491, 2005. 29

[104] J. Pauli. *Einsatz der Elektrodiffusionsmesstechnik in Gas-Flüssigkeits-Strömungen mit Sauerstoff als Depolarisator.* PhD thesis, Universität Dortmund, Dortmund, 1991. 42, 45

[105] D. Pfleger and S. Becker. Modelling and simulation of the dynamic flow behaviour in a bubble column. *Chemical Engineering Science*, 56:1737–1747, 2001. 8, 11, 12, 13, 27, 28

[106] H. T. B. Pham, G. Larsson, and S.-O. Enfors. Growth and Energy Metabolism in Aerobic Fed-Batch Cultures of Saccharomyces cerevisiae: Simulation and Model Verification. *Biotechnology and Bioengineering*, 60, 4:474–482, 1998. 55, 56, 122

[107] T. Potma. *Dehnungsmessstreifen-Messtechnik.* Deutsche Philips GmbH, Hamburg, 1968. 117

[108] S. Rigopoulos and A. Jones. A hybrid CFD reaction engineering framework for multiphase reactor modelling: basic concept and application to bubble column reactors. *Chemical Engineering Science*, 58:3077–3089, 2003. 15

[109] H. Ritter, K. Schulten, and T. Martinetz. *Neuronale Netze: Eine Einführung in die Neuroinformatik selbstorganisierender Netzwerke.* Addison-Wesley, Bonn, München, 2nd edition, 1991. 79

[110] J. J. Romanainen. Numerical approach to modeling of dynamic bubble columns. *Chemical Engineering and Processing*, 36:1–15, 1997. 15

[111] R. Sardeing, P. Painmanakul, and G. Hebrard. Effect of surfactants on liquid-side mass transfer coefficients in gas-liquid systems: A first step to modeling. *Chemical Engineering Science*, 61:6249–6260, 2006. 29, 30

[112] Y. Sato and M. Sadatomi. Momentum and Heat Transfer in Two-phase Bubbly Flow – I. *International Journal of Multiphase Flow*, 7:167–177, 1981. 10, 27

[113] Y. Sato, M. Sadatomi, and K. Sekoguchi. Momentum and Heat Transfer in Two-Phase Bubble Flow II – A Comparison Between Experimental Data and Theoretical Calculations. *International Journal of Multiphase Flow*, 7:179–190, 1981. 10

[114] Y. Sato and K. Sekoguchi. Liquid Velocity Distribution in Two-phase Bubble Flow. *International Journal on Multiphase Flow*, 2:79–95, 1975. 10, 27

[115] J. Schallenberg. *Modellierung von zwei- und dreiphasigen Strömungen in Blasensäulenreaktoren.* PhD thesis, TU Braunschweig, Braunschweig, in Hempel D. C. (editor): ibvt-Schriftenreihe Vol. 24, FIT-Verlag, Paderborn, Oktober 2005. 8, 9, 10, 11

[116] H. Schlichting and K. Gersten. *Grenzschichttheorie.* Springer, Berlin, Heidelberg, New York, 10th edition, 2006. 17, 28

[117] M. Schlüter. *Blasenbewegung in praxisrelevanten Zweiphasenströmungen.* PhD thesis, Universität Bremen, Bremen, Februar 2002. 21

[118] S. Schmalzriedt. *CFD-Simulationen von Mischvorgängen und biotechnischen Stoffumsetzungen in begasten Rührkesselreaktoren.* PhD thesis, Universität Stuttgart, Stuttgart, June 2001. 15

[119] A. Schumpe and G. Grund. The Gas Disengagement Technique for Studying Gas Holdup Structure in Bubble Columns. *The Canadian Journal of Chemical Engineering*, 64:891–896, 1986. 9, 21

[120] K. Schügerl. Apparative Aspekte von Blasensäulen-Bioreaktoren. *Chemie-Ingenieur-Technik*, 49:605–611, 1977. 5, 6

[121] J. Schütze. *Die numerische Simulation von Strömung und Stoffaustausch in gerührten, begasten Bioreaktoren.* PhD thesis, Technische Universität Braunschweig, Braunschweig, November 2001. 29

[122] M. Simonnet, C. Gentric, E. Olmos, and N. Midoux. Experimental determination of the drag coefficient in a swarm of bubbles. *Chemical Engineering Science*, 62:858–866, 2007. 21, 22

[123] V. Singh, A. Constantinides, and R. Fuchs. A New Method for Fermenter Scale-up Incorporating Both Mixing and Mass Transfer Effects – I. Theoretical Basis. *Biotechnology Processes*, 1987. 13

[124] A. Sokolichin. *Mathematische Modellbildung und numerische Simulation von Gas-Flüssigkeits-Blasenströmungen.* PhD thesis, Universität Stuttgart, Stuttgart, December 2003. 11

[125] A. Sokolichin and G. Eigenberger. Gas-Liquid Flow in Bubble Columns and Loop Reactors: Part I. Detailed Modelling and Numerical Simulation. *Chemical Engineering Science*, 49, 2:5735–5746, 1994. 9

[126] A. Sokolichin, G. Eigenberger, and A. Lapin. Simulation of Buoyancy Driven Bubbly Flow: Established Simplifications and Open Questions. *AIChE Journal*, 50, 1:24–45, 2004. 8, 9, 10, 11, 12, 13, 14, 27

[127] B. Sonnleitner and O. Käppeli. Growth of Saccharomyces cerevisiae Is Controlled by Its Limited Respiratory Capacity: Formulation and Verification of a Hypothesis. *Biotechnology and Bioengineering*, 28:927–937, 1986. 55, 56

[128] H. Sontheimer, P. Spindler, and U. Rohmann. *Wasserchemie für Ingenieure.* ZfGW-Verlag GmbH, Frankfurt am Main, 1980. 31

[129] K. Sriram and R. Mann. Dynamic Gas Disengagement a New Technique for Assessing the Behaviour of Bubble Columns. *Chemical Engineering Science*, 32:571–580, 1977. 21

[130] P. Steinke. *Finite-Elemente-Methode: Rechnergestützte Einführung*. Springer-Verlag, Berlin, Heidelberg, 2nd edition, 2007. 111

[131] A. Steinmann. *Numerische und experimentelle Untersuchung der ein- und zweiphasigen Strömung in einem technisch belüfteten Abwasserteich*. PhD thesis, TU Berlin, Berlin, August 2002. 6, 37

[132] M. Stöhr. Entwicklung dreidimensionaler Particle Tracking Velocimetry zur Messung der Zweiphasenströmung in Gas-Flüssig-Reaktoren. Master's thesis, Universität Heidelberg, Heidelberg, July 1998. 43

[133] E. K. Todtenhaupt. Blasengrößenverteilung in technischen Begasungsapparaten. *Chemie-Ingenieur-Technik*, 43:336–342, 1971. 6

[134] A. A. Troshko and Y. A. Hassan. A two-equation turbulence model of turbulent bubbly flows. *International Journal of Multiphase Flow*, 27:1965–2000, 2001. 27

[135] A. Tsutsumi and R. Kikuchi. Design and scale-up methodology for multi-phase reactors based on non-linear dynamics. *Applied Energy*, 67:195–219, 2000. 6

[136] K. Ueyama and T. Miyauchi. Properties of Recirculating Turbulent Two Phase Flow in Gas Bubble Columns. *American Institute of Chemical Engineers Journal*, 25:258–266, 1979. 49, 50

[137] J. M. van Baten, J. Ellenberger, and R. Krishna. Scale-up strategy for bubble column slurry reactors using CFD simulations. *Catalysis Today*, 79–80:259–265, 2003. 6

[138] J. M. van Baten and R. Krishna. Eulerian simulations for determination of the axial dispersion of liquid and gas phases in bubble columns operating in the churn-turbulent regime. *Chemical Engineering Science*, 56:503–512, 2001. 6, 9, 11, 12

[139] J. M. van Baten and R. Krishna. Comparison of Hydrodynamics and Mass Transfer in Airlift and Bubble Column Reactors Using CFD. *Chemical Engineering and Technology*, 26, 10, 2003. 13

[140] P. C. van der Aar, H. W. van Verseveld, and A. H. Stouthamer. Stimulated glycolytic flux increases the oxygen uptake rate and aerobic

ethanol production, during oxido-reductive growth of Saccharomyces cerevisiae. *Journal of Biotechnology*, 13:347–359, 1990. 56

[141] W. R. A. Vauk and H. A. Müller. *Grundoperationen chemischer Verfahrenstechnik*. Deutscher Verlag für Grundstoffindustrie, Stuttgart, 11. edition, 2000. 21

[142] C. Verduyn, A. H. Stouthamer, W. A. Scheffers, and J. P. van Dijken. A theoretical evaluation of growth yields of yeasts. *International Journal of General and Molecular Microbiology*, 59:49–63, 1991. 124

[143] H. K. Versteeg and W. Malalasekera. *An Introduction to Computational Fluid Dynamics: The Finite Volume Method*. Pearson, Harlow, 1995. 16, 17, 18, 25, 26, 27, 37

[144] A. Vetter, D. C. Hempel, and A. Haarstrick. A method to couple cfd and biological growth. *in progress*. 87

[145] P. Vrabel, R. van der Lans, F. van der Schot, K. Luyben, B. Xu, and S.-O. Enfors. CMA: integration of fluid dynamics and microbial kinetics in modelling of large-scale fermentations. *Chemical Engineering Journal*, 84:463–474, 2001. 14

[146] T. Wang and J. Wang. Numerical simulations of gas liquid mass transfer in bubble columns with a CFD PBM coupled model. *Chemical Engineering Science*, 62:7107–7118, 2007. 13

[147] Daniel Weinzierl. Hefezellen als Template für die Erzeugung hohler Pigmente durch Beschichtung mit anorganischen Feststoffen. In *Vortragstexte der 20. VH-Hefetagung am 23. und 24. April 2007*, number 20 in Fortschritte in Wissenschaft und Technik der Hefeproduktion, pages 127–133, Berlin, 2007. Versuchsanstalt der Hefeindustrie e.V. 1

[148] J. P. Wen, X. Q. Jia, and W. Feng. Hydrodynamic and Mass Transfer of Gas-Liquid-Solid Three-Phase Internal Loop Airlift Reactors with Nanometer Solid Particles. *Chemical Engineering & Technology*, 28:53–60, 2005. 13

[149] C. Wiebels. *A Novel Bubble Size Measuring Technique for High Bubble Density Flows*. PhD thesis, TU Braunschweig, Braunschweig, in Hempel D. C. (editor): ibvt-Schriftenreihe Vol. 39, FIT-Verlag, Paderborn, December 2008. 10, 39, 42

[150] M. D. Williams and M. Oostrom. Oxygenation of anoxic water in a fluctuating water table system: an experimental and numerical study. *Journal of Hydrology*, 230:70–85, 2000. 38

[151] P. Zehner. Impuls-, Stoff- und Wärmetransport in Blasensäulen. *Chemie-Ingenieur-Technik*, 54:248–251, 1982. 50

[152] D. Zhang, N. G. Deen, and J. A. M. Kuipers. Numerical simulation of the dynamic flow behavior in a bubble column: A study of closures for turbulence and interface forces. *Chemical Engineering Science*, 61:7593–7608, 2006. 27, 28

[153] T. Zhang, B. Zhao, and J. Wang. Mathematical models for macro-scale mass transfer in airlift loop reactors. *Chemical Engineering Journal*, 119:19–26, 2006. 13

[154] H. Znad, M. Tokumura, and Y. Kawase. Axial Distribution of Oxygen Concentration in Different Airlift Bioreactor Scales: Mathematical Modeling and Simulation. *Chemical Engineering Technology*, 29, 9:1042–1047, 2006. 14

Appendix A

Cantilever Probe

Section 3.1 has shown that there is no cheap and easy to handle measurement technique giving average flow velocity information and determining the direction at the same time. No systems are known being applicable to high disperse phase holdups and optically dense fluids. In many cases these are exactly the requirements for a given multiphase measurement case.

A.1 Measuring Device

According to accelerometers and clinometers a strain gauge cantilever probe shown in **figure A.1** has been developed within the frame of this work in order to fulfill these requirements. The probe is based on a cantilever with a cross section profile being very stiff against bending in one direction but well-defined stiff against bending perpendicular to the first direction in means of the z-axis in figure A.1.

Figure A.2 shows the cross section view of the probe. A strain gauge is appliqued to one side of the cantilever beam measuring beam deflection. Due to probe use in conductive fluids the strain gauge is coated. Enameled copper wire connects the strain gauge to the amplifier. Locking pins lock the cantilever beam into position. Connections are sealed against surrounding fluids. The beam measures 45 mm in length, 7.5 mm in width and 0.3 mm in height. Measured liquid velocity is therefore an average value of the surrounding volume.

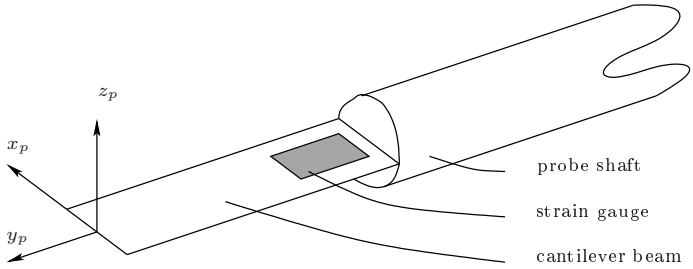

Figure A.1: Strain gauge cantilever probe

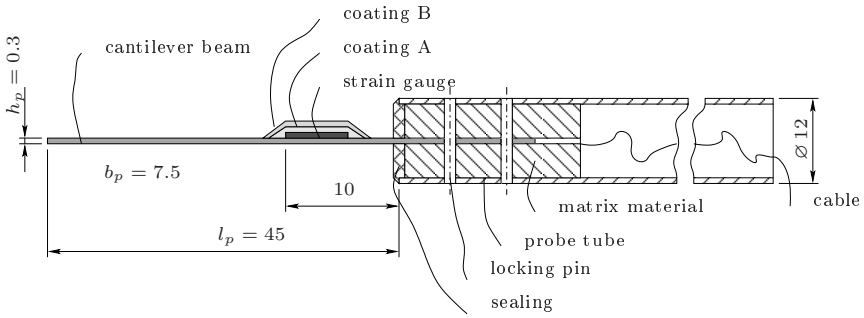

Figure A.2: Cross sectional view of the strain gauge cantilever probe with measures in mm

Not a single strain gauge as shown in figure A.1 has been appliqued but a full bridge strain gauge with four single gauges as shown in **figure A.3**. The gauges R_2 and R_3 do not contribute. A full bridge circuit is recommended for linearity reasons and temperature compensation.

The measuring system communicates as shown in **figure A.4**. The voltage signal from the strain gauge is amplified. A voltage frequency converter converts the signal to a frequency which is input into a standard sound card in a computer. The free acquisition software *uf_verlauf* by Klaus-Dieter Grüninger reconverts the frequency signal into a voltage with the Fast Fourier

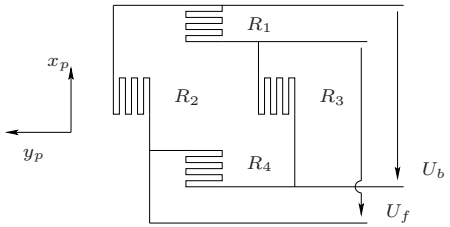

Figure A.3: Full strain gauge bridge circuit as appliqued to the carbon cantilever beam with probe coordinates as well as feeding and bridge voltage

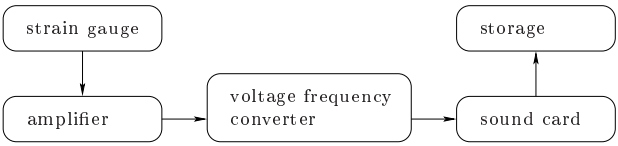

Figure A.4: Structure of the measuring system and the data acquisition

Transform (section A.4). Finally, voltage signals are stored together with time information.

Beam material, strain gauge as well as beam dimensions are the parameters for adjusting the probe to a specified measuring range. Velocity ranges from some millimeters up to several meters per second are possible. Basic formulas for the outer fiber tension σ_p and the related strain ε_p due to a single load F at the beam tip and the section modulus W_p are given by equations A.1 to A.3. h_p, b_p and l_p are the cantilever beam height, width and length, respectively. E_p is the elastic modulus of the beam material.

$$\sigma_p = \varepsilon_p E_p = \frac{T}{W_p} = \frac{F l_p}{W_p} \tag{A.1}$$

$$W_p = \frac{b_p h_p^2}{6} \tag{A.2}$$

$$\varepsilon_p = \frac{F l_p}{W_p E_p} = \frac{6 F l_p}{b_p h_p^2 E_p} \tag{A.3}$$

As an invasive probe of significant size this measurement technique influences the flow field. For a deflected beam the incident flow direction changes even though the real flow direction remains unchanged. Relatively small deflections are assumed. Errors due to deflection may consequently be neglected. Depending on the incident flow direction the probe shaft may influence the flow field leading to additional errors.

The probe averages the fluid velocity. Probe size determines averaging quality. Large probes are less sensitive to disturbances due to the dispersed phase. Dispersed phase movement is expected to have only a little influence since liquid phase momentum exceeds the momentum of the gas phase by far. The mentioned effects raise questions about good calibration methods which is discussed in section A.3.

A.2 Eigen Frequencies of a Cantilever Beam

Cantilever beams are dynamic systems. Dynamic systems have characteristic eigen frequencies and eigen modes where little energy is needed to get huge system responses. First, these modes may destroy the system. Second, close to the eigen frequencies measurement results do not necessarily reflect the actual state of the system. As a consequence, measurements have to be performed in a certain distance to the eigen frequencies.

A comparison of the smallest eigen frequency and measured frequencies shall show this distance. Macroscopic scales are of interest since microscopic scales cannot affect the function of the relatively large probe. Inertia forces for the most part damp small scale effects.

Figure A.5 shows a uniformly distributed load case, similar to realistic load cases of the probe.

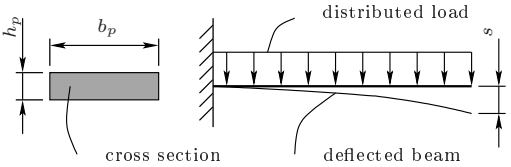

Figure A.5: Cantilever beam with exemplary uniformly distributed load

Equations A.4 to A.6 give estimates of the lowest eigen frequency for the given load case [102, 130].

$$\omega_{1a} \leq \frac{\sqrt{20}}{l_p^2}\sqrt{\frac{E_p I}{\varrho A}} \tag{A.4}$$

$$\omega_{1b} = \frac{0.562}{l_p^2}\sqrt{\frac{E_p I}{\varrho A}} \tag{A.5}$$

$$\omega_{1c} \approx \frac{3.61}{l_p^2}\sqrt{\frac{E_p I}{\varrho A}} \tag{A.6}$$

With the measures $l_p = 0.045\,\mathrm{m}$, $b_p = 0.0075\,\mathrm{m}$ and $h_p = 0.0003\,\mathrm{m}$ the geometrical moment of inertia of bending about the lateral axis I and the cross section area A are calculated:

$$I = \frac{b_p h_p^3}{12} = 1.6875 \cdot 10^{-14}\,\mathrm{m}^4 \tag{A.7}$$

$$A = b_p h_p = 2.25 \cdot 10^{-6}\,\mathrm{m}^2 \tag{A.8}$$

The mass density ϱ_c of the carbon fiber fabric depends upon the volume fractions of fiber and matrix material and their mass density. Values are related to the used fabric with Köper binding.

$$\begin{aligned} \varrho_c &= \varrho_m r_m + \varrho_f r_f \\ &= 1161\,\frac{\mathrm{kg}}{\mathrm{m}^3} \cdot 0.65 + 1797\,\frac{\mathrm{kg}}{\mathrm{m}^3} \cdot 0.35 \\ &= 1384\,\frac{\mathrm{kg}}{\mathrm{m}^3} \end{aligned} \tag{A.9}$$

The elastic modulus is calculated in a similar way.

$$\begin{aligned} E_p &= E_\parallel = E_f r_{f\parallel} + E_m\,(r_m + r_{f\perp}) \\ &= 238000\,\frac{\mathrm{N}}{\mathrm{mm}^2} \cdot 0.35 \cdot 0.5 + \\ &\quad 3000\,\frac{\mathrm{N}}{\mathrm{mm}^2}\,(0.65 + 0.35 \cdot 0.5) \\ &= 44125\,\frac{\mathrm{N}}{\mathrm{mm}^2} \approx 45000\,\frac{\mathrm{N}}{\mathrm{mm}^2} \end{aligned} \tag{A.10}$$

Using equations A.4 to A.10 the lowest eigen frequency can be estimated. The strain gauge additionally stiffens the beam resulting in an even higher first eigen frequency.

$$\omega_{1a} = 1090.58\,\text{Hz} \tag{A.11}$$
$$\omega_{1b} = 137.04\,\text{Hz} \tag{A.12}$$
$$\omega_{1c} = 880.31\,\text{Hz} \tag{A.13}$$

Frequency estimation of macroscopic fluid motion from experimental results gives typical frequencies ω_{flow} of some Hertz.

$$\omega_{flow} \approx 5\,\text{Hz} \overset{\checkmark}{\ll} 130\,\text{Hz} \approx \omega_{eigen} \tag{A.14}$$

Thus, the eigen frequencies of this probe do not cause any difficulties in the specified flow case.

A.3 Calibration

Calibration is a central part of most measurement techniques. Since real measurement cases are complex systems, calibrators have to be chosen in a sense of realistic system simplification.

The strain gauge cantilever probe is made to measure velocity components in z-direction of the probe which is the normal vector of the cantilever beam surface (figure A.1). The angle between the incident flow direction and the probe normal vector is defined as the probe angle α_i as shown in **figure A.6**. The angle of $0\,^\circ$ corresponds to an incident flow direction opposite parallel to the normal vector $\underline{n}$.

A calibration system as shown in **figure A.7** has been used. Water from a basin is circulated at a specified flow rate. Before entering the basin via a circular orifice as a water jet the water is straightened and pacified in order to reduce turbulence. The circular orifice has a diameter of 8 mm. The probe is positioned 20 mm downstream from the orifice with the beam tip in the center of the jet.

The jet case is closer to a single load than it is to a distributed. In the bubble column the actual beam load depends upon the eddy size and position. Single loads applied to the beam have decreasing influence on tip deflection with increasing distance to the beam tip. It is assumed that the probe is best

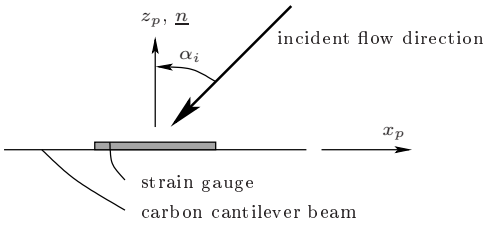

Figure A.6: Definition of the probe angle with respect to the incident flow direction

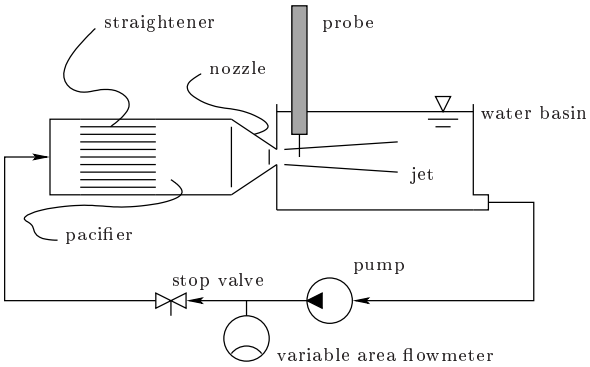

Figure A.7: Probe calibration system

calibrated with its beam tip in the center of the jet. The probe only gives average information about the flow field. Therefore, measurement time must not be too short in order to reduce the impact of the known error.

As the strain gauge has been appliqued to only one side, the bending characteristic of the cantilever beam is biased. Consequently, calibration curves for both, 0 ° and 180 ° as direction of incident flow are needed. The branches of the calibration curve in **figure A.8** thus show different slopes.

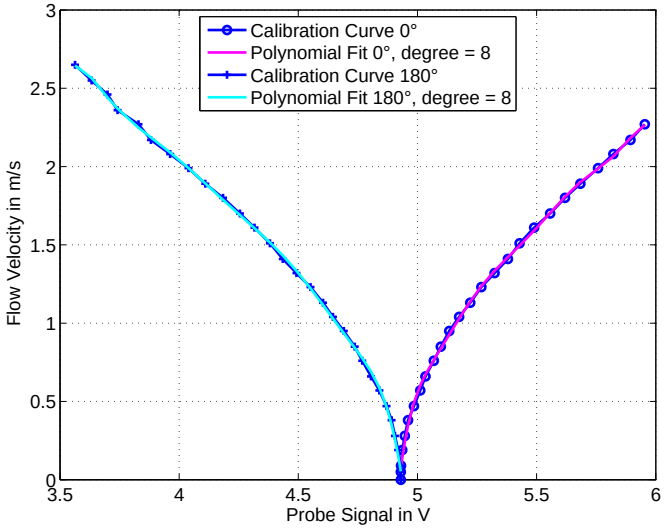

Figure A.8: Calibration curve for incident flow direction of 0 ° and 180 °, for coefficients of calibration curves see table A.1

Strain gauges give distinct information depending on compression or elongation due to beam deflection. The probe normal vector shall be parallel to the velocity component of interest.

A.4 Signal Analysis

The software *uf_verlauf* stores the voltage ten times a second over 50 s. Velocity information is then calculated from the raw data using the relevant calibration curve by means of the polynomial fit (**table A.1**). Voltage signals greater than the zero velocity voltage are converted by the right half of the curve shown in figure A.8. Values below that are converted with the left half of the curve from figure A.8. The velocity information is finally averaged over the entire measurement time.

Table A.1: Polynomial Coefficients of calibration curves (figure A.8)

Coefficients of Calibration Curve 0 °				
x^8	x^7	x^6	x^5	x^4
-449	$1.967 \cdot 10^4$	$-3.764 \cdot 10^5$	$4.113 \cdot 10^6$	$-2.807 \cdot 10^7$
x^3	x^2	x^1	x^0	
$\cdot 226 \cdot 10^8$	$-3.342 \cdot 10^8$	$5.205 \cdot 10^8$	$-3.544 \cdot 10^8$	
Coefficients of Calibration Curve 180 °				
x^8	x^7	x^6	x^5	x^4
-48	$-1.622 \cdot 10^3$	$-2.390 \cdot 10^4$	$2.009 \cdot 10^5$	$-1.053 \cdot 10^6$
x^3	x^2	x^1	x^0	
$3.530 \cdot 10^6$	$-7.382 \cdot 10^6$	$8.807 \cdot 10^6$	$-4.589 \cdot 10^6$	

http://www.schule-bw.de/unterricht/faecher/physik/mess/soundkarte/uf_verlauf.htm#documentContent

A.5 Probe Angular Characteristic

The probe measures velocity components parallel to the probe normal vector. At the present time, the probe has not been calibrated in the y_p-z_p-plane where results are expected to be less good. Tip deflection causes a systematic error because of relative changes in incident flow direction.

Assuming only velocity vectors in the probe x_p-z_p-plane with the magnitude u, the magnitude of the component u_n normal to the probe is calculated using the cosine of the angle (figure A.6).

$$u_n = u \cdot \cos(\alpha_i) \tag{A.15}$$

Probes with good angular characteristics measure exactly the component determined by equation A.15 for any given angle of incident flow. This test has been done for the velocities $u = n \cdot 0.5 \frac{\mathrm{m}}{\mathrm{s}}$ with $n = [1, 2, 3, 4, 5]$ and the angles $\alpha_i = 0\,^\circ + m \cdot 30\,^\circ$ with $m = [0, 1, 2, \ldots 11]$. Exemplary results are given as polar plot in **figure A.9**. The two circles represent the exact velocity values in normal direction. The probe shows good overall performance.

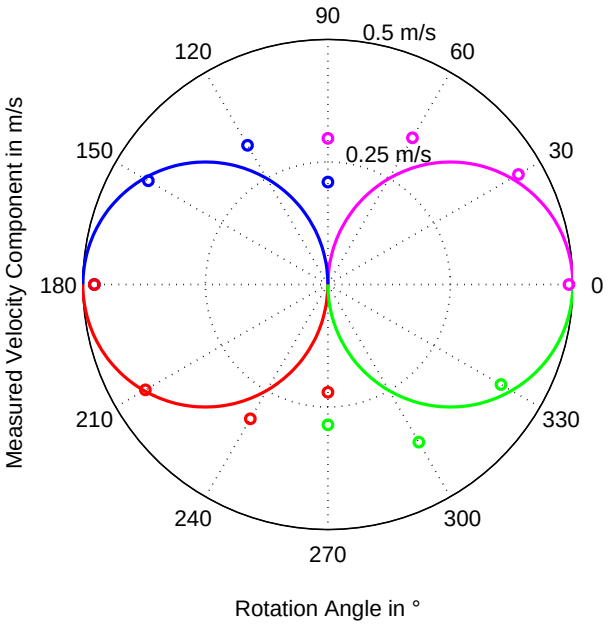

Figure A.9: Probe x_p-z_p angular characteristic for incident flow velocity 0.5 m/s, colored lines represent exact normal velocity components, the dotted circle represents velocity 0.25 m/s, the outer circle represents velocity 0.5 m/s

Relative errors in the low velocity range are greater than those in the high velocity range. As a prototype this probe is not optimized for a certain velocity level. Results for 60° to 120° and 240° to 300° show worst probe performance. This is due to the airfoil character the probe shows under these angles.

Together with characteristics of the y_p-z_p-plane the probe characteristic becomes a three-dimensional hull body made of two spheres touching each other similar to the two circles in figure A.9. The probe will probably not

show this theoretical behavior because of interference from the probe shaft and from asymmetric probe geometry.

Conclusively, the new strain gauge cantilever probe is a great device to measure specified average liquid velocity components in liquid and gas/liquid flows. The impact of the dispersed gas phase is neglected due to the relatively low mass density and thus the relatively low momentum transport. The probe is invasive but not restricted to any dispersed phase holdup or to the optical quality of the mixture.

A general problem with the probe design is its size. Calibration and measurement do not apply the same loads to the strain gauge cantilever probe which has to be taken into account for the measurements presented. Future development may miniaturize the probe. Calibration situation will then not much differ from measurement situation. As a consequence, measured results will be much more reliable with increased spatial resolution.

A.6 Measured Velocity Profiles

Each position has been measured twice with the probe normal vector in parallel to the reactor axis. First the strain gauge faces the bottom and second it faces the reactor head. Measurement results taken with the probe from the opposite side of the reactor agree. In addition to figures 3.3 and 3.4 the **figures A.10** and **A.11** show the values taken with the strain gauge cantilever probe.

The profile measured with the strain gauge cantilever probe deviates significantly from the profile measured with the pressure probe in the region close to the fittings at level 1120 mm. The measured values show the correct order of magnitude over the entire range.

A.7 Attempts in Measurement Development

Strain gauges work in optimal manner when elongated. Therefore, they shall be appliqued to both, upper and lower face of the cantilever beam in a way that one strain gauge is elongated in either direction of bending.

Similar to cantilever beam based clinometers, a second direction of measurement can be added by another cantilever beam fixed to the tip of the first in axial direction but rotated 90 ° about the axis [107]. An important

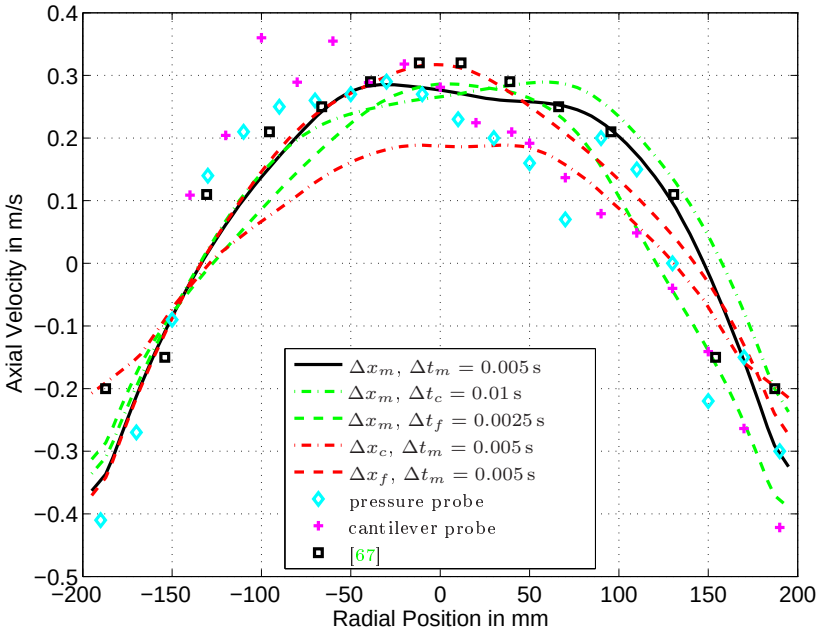

Figure A.10: Measured and simulated velocity profiles at vertical position $z = 900\,\mathrm{mm}$, for positions and coordinates see figure 2.1, for mesh sizes see table 2.2

disadvantage of such an add-on is the increased probe size. Superposition of effects might increase the measurement error.

Beam material and geometry have to be optimized with respect to known quality requirements. The probe has to be designed to optimally resolve velocities in an expected range. The used prototype performs great in the velocity range above $1\,\frac{\mathrm{m}}{\mathrm{s}}$. Low-cost production of the probe enables the use of a set of range-optimized probes.

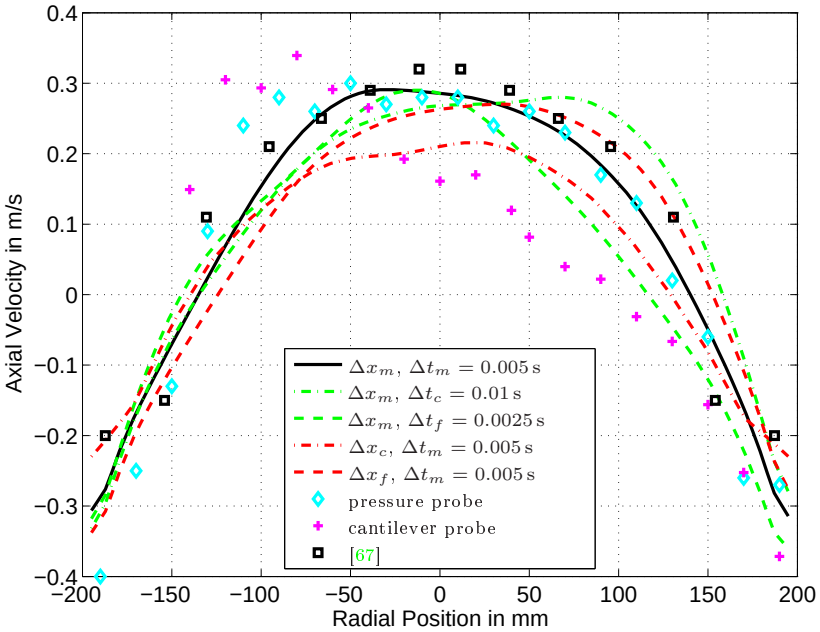

Figure A.11: Measured and simulated velocity profiles at vertical position $z = 1120\,\mathrm{mm}$, for positions and coordinates see figure 2.1, for mesh sizes see table 2.2

Smaller probes reduce flow disturbance. The reduced measurement volume gives information which can be referred to be local. The tip of the probe shaft may be of conical shape to reduce the influence of the shaft.

A step to the micro-electromechanical systems (MEMS) with cantilever beams and possibly integrated strain gauges gives possibilities to reduce probe size down to the sub-millimeter scale. Simple cantilever beam probes likewise the suggested probe type can also be integrated to form probes for three-

dimensional measurements similar to tactile sensor heads used in robotics [59].

Even though the presented strain gauge cantilever probe still has its problems, the idea of simple cantilever beams for detection of flow direction and velocity is convincing. Measurement results have especially shown good angular performance which is of great importance in transient flow measurements.

Reactor systems often require special hygienic treatment in terms of sterilization. This complicates application of measurement systems in production runs. The following probe type may solve a number of related problems. A small spherical sensor in the range of 10 to 15 mm in diameter and of the same density as the fluid traces the flow field. The sensor is assumed to follow the fluid not accounting for turbulent fluctuations.

This sensor has to have one translational and one rotational accelerometer for each axis as well as an appropriate power support, a microprocessor and a memory storing the information. Latest sensor development at Bosch Sensortec came up with a three-axial acceleration sensor called SMB 380 in the size of a match head.

Subsequent integration theoretically gives velocity information together with trajectories considering a known start and end position with zero velocity. Statistical evaluation of the data provides with an insight into the average flow field. Acceptable measurement times effect flow field measurement result of sufficient resolution. Provided that this technique works well, the sensor gives industry at hand a powerful, affordable and easy to handle tool.

The sensor can be varied using a gyroscope instead of the three rotational accelerometers to hinder the sensor from rotating. Of course, this type requires increased energy support but significantly reduces complexity of analysis and sources of error. Both latter techniques have not been tested, yet.

Appendix B

Constants and Parameters for the Growth Model

Table B.1: Model constants parameters and initial values [106]

Parameter	Value	Unit
C_e	$4.35 \cdot 10^{-2}$	mol$C$ g^{-1}
C_s	$3.33 \cdot 10^{-2}$	mol$C$ g^{-1}
C_x	$3.84 \cdot 10^{-2}$	mol$C$ g^{-1}
K_e	0.1	g L^{-1}
K_i	10	g L^{-1}
K_s	0.12	g L^{-1}
q_m	0.01	g g^{-1} h^{-1}
$q_{O_2,max}$	0.3	g g^{-1} h^{-1}
$q_{s,max}$	2.4	g g^{-1} h^{-1}
t_L	0.75	h
S_{crit}	0.04	g L^{-1}
Y_{es}	0.51	g g^{-1}
Y_{oe}	2.087	g g^{-1}
Y_{os}	1.067	g g^{-1}
Y_{xe}	0.72	g g^{-1}
Y_{xs_f}	0.1	g g^{-1}
$Y_{xs_{ox}}$	0.48	g g^{-1}
E_0	0	g L^{-1}
$O_{\alpha 0}$	$1.52 \cdot 10^{-3}$	g L^{-1}
$O_{\beta 0}$	0.29963	g L^{-1}
S_0	$2.36 \cdot 10^{-4}$	g L^{-1}
X_0	7.0628	g L^{-1}
V_0	120	L
S_{in}	270	g L^{-1}
$q_{s,in,0}$	1.21	g L^{-1} h^{-1}
$q_{s,in,max}$	1.72	g L^{-1} h^{-1}
k_L	$3.1 \cdot 10^{-4}$	m s^{-1}

Appendix C

Material for Cultivation Experiments

C.1 Instruments for Experimental Setup

- Pressure reduction valve: Reduces supply line pressure from about $13 \cdot 10^5$ to $1 \cdot 10^5 \frac{\mathrm{kg}}{\mathrm{s}^2\,\mathrm{m}}$.
- Variable area flow meter: Yokogawa G263 SW = PD26N
- O_2 probe: BlueSens BCP-O_2, $0 - 25\,\mathrm{Vol}\%$, $0.8 - 1.3 \frac{\mathrm{kg}}{\mathrm{s}^2\,\mathrm{m}}$ abs
- CO_2 probe: BlueSens BCP-CO_2, $0 - 25\,\mathrm{Vol}\%$, $0.8 - 1.3 \frac{\mathrm{kg}}{\mathrm{s}^2\,\mathrm{m}}$ abs
- Medium pump: Meredos GLV-70
- Alkaline solution pump: Meredos TV 20
- Cooling and heating circuit pump: Ivaki Magnetic Gear Pump MDG-M15S3B, Siemens motor
- Secondary cooling and heating circuit pump and control: Lauda Ecoline Staredition RE 107, Lauda Ecoline Staredition E 100
- Thermometer: Juno itron 08, thermo couple

- pH probe and control: Mettler Toledo 405-DPAS-SC-KOS/225 combination pH, Meredos pH Control 2
- pO_2 probe and control: WTW CellOx 325 galvanic electrode, WTW ProfiLab Oxi 597-S

C.2 Material for Experiments

- Alkaline solution: 5 M NaOH
- Antifoam agent: Fragol, Ucolub N115 based on polypropylenglycol, limited solubility in mineral oil, hydrophobic
- Yeast *Saccharomyces cerevisiae*: Uniferm, commercial quality, $48 \cdot 42\,\mathrm{g} \cdot 0.27$ dry biomass for 125 L as inoculum
- The medium is based on the medium proposed by Verduyn [142]. Values for salts, trace elements, glucose and vitamins are given below.

Salts

- initial: $15\,\frac{\mathrm{g}}{\mathrm{L}}$ $(NH_4)_2SO_4$
- feed: $7.7\,\frac{\mathrm{g}}{\mathrm{L}}$ $(NH_4)_2SO_4$
- $3\,\frac{\mathrm{g}}{\mathrm{L}}$ KH_2PO_4
- $1.5\,\frac{\mathrm{g}}{\mathrm{L}}$ $MgSO_4 \cdot 7\ H_2O$

Trace Elements

- $4.5 \cdot 10^{-3}\,\frac{\mathrm{g}}{\mathrm{L}}$ Na_2EDTA
- $13.5 \cdot 10^{-3}\,\frac{\mathrm{g}}{\mathrm{L}}$ $ZnSO_4 \cdot 7\ H_2O$
- $2.52 \cdot 10^{-3}\,\frac{\mathrm{g}}{\mathrm{L}}$ $MnCl_2 \cdot 2\ H_2O$
- $0.9 \cdot 10^{-3}\,\frac{\mathrm{g}}{\mathrm{L}}$ $CoCl_2 \cdot 6\ H_2O$
- $0.9 \cdot 10^{-3}\,\frac{\mathrm{g}}{\mathrm{L}}$ $CuSO_4 \cdot 5\ H_2O$
- $1.2 \cdot 10^{-3}\,\frac{\mathrm{g}}{\mathrm{L}}$ $Na_2MoO_4 \cdot 2\ H_2O$
- $13.5 \cdot 10^{-3}\,\frac{\mathrm{g}}{\mathrm{L}}$ $CaCl_2 \cdot 2\ H_2O$
- $9 \cdot 10^{-3}\,\frac{\mathrm{g}}{\mathrm{L}}$ $FeSO_4 \cdot 7\ H_2O$
- $3 \cdot 10^{-3}\,\frac{\mathrm{g}}{\mathrm{L}}$ H_3BO_3
- $0.3 \cdot 10^{-3}\,\frac{\mathrm{g}}{\mathrm{L}}$ KI

Glucose

- $270\,\frac{g}{L}$

Vitamins

- $0.05 \cdot 10^{-3}\,\frac{g}{L}$ d-biotin
- $1 \cdot 10^{-3}\,\frac{g}{L}$ ca-d-pantothenate
- $1 \cdot 10^{-3}\,\frac{g}{L}$ nicotinic acid
- $25 \cdot 10^{-3}\,\frac{g}{L}$ myo-inositol
- $1 \cdot 10^{-3}\,\frac{g}{L}$ thiamine hydrochloride
- $1 \cdot 10^{-3}\,\frac{g}{L}$ pyridoxine hydrochloride
- $0.2 \cdot 10^{-3}\,\frac{g}{L}$ p-aminobenzoic acid

C.3 Instruments for Analysis

Devises used for sample preparation and experiment analysis are listed below. Moreover, settings and methods are mentioned where necessary.

- Filter: CA membrane, $0.2\,\mu$m, non-pyrogenic, hydrophilic
- Glucose measurement: YSI 2700 Select Biochemistry Analyzer
- Optical density measurement: Bio Rad Smart Spec 3000
- Centrifuge: Heraeus Biofuge stratos
- HPLC: Polyspher OAHY Cat 1.51272 300×6.5 at 343.15 K, runtime 15 minutes, flow rate 0.8 mL per minute, flow agent 2.5 mmol H_2SO_4

C.4 Constants for the Pure Growth Model

Table C.1: Model constants, parameters and initial values for the pure growth simulation

Parameter	Value	Unit
E_0	0	gL^{-1}
O_0	0.00152	$\mathrm{g\,L}^{-1}$
$O_{0,g}$	0.29963	$\mathrm{g\,L}^{-1}$
S_0	0.000236	$\mathrm{g\,L}^{-1}$
X_0	7.0628	$\mathrm{g\,L}^{-1}$
V_0	130	L
S_{in}	270	$\mathrm{g\,L}^{-1}$
$q_{s,in,0}$	157	$\mathrm{g\,h}^{-1}$
$q_{s,in,max}$	250	$\mathrm{g\,h}^{-1}$
k_L	$3.1 \cdot 10^{-4}$	$\mathrm{m\,s}^{-1}$
$r_{\beta 1}$	0.025882	1
$r_{\beta 2}$	0.053109	1
$r_{\beta 3}$	0.024370	1
$d_{\beta,1}$	0.08	m
$d_{\beta,2}$	0.003	m
$d_{\beta,3}$	0.0008	m

Notation

The following list shows the used notation, symbols and variables.

Variables

Variable	Unit	Description
A	m^2	Cross section area
$A_{\alpha\beta}$	m^2	Interphase area
A_β	m^2	In flow direction projected area of single bubble
a	1	Stoichiometric coefficient
$a_{\alpha\beta}$	$\frac{1}{\mathrm{m}}$	Interphase area density, volume specific surface area
$a_{\alpha\beta i}$	$\frac{1}{\mathrm{m}}$	Interphase area density, volume specific surface area of class i
$a_{\alpha\beta id}$	$\frac{1}{\mathrm{m}}$	Deviating interphase area density, volume specific surface area of class i
b	1	Stoichiometric coefficient
b_p	mm	7.5, Width of strain gauge cantilever probe
C	1	Carbon, in chemical formulas
C_e	$\frac{\mathrm{mol}C}{\mathrm{g}}$	0.0435, Carbon content of ethanol
C_k	1	$C_{\varepsilon 1}$, Constant in bubble induced turbulence k-ε model
C_s	$\frac{\mathrm{mol}C}{\mathrm{g}}$	0.0333, Carbon content of glucose
C_x	$\frac{\mathrm{mol}C}{\mathrm{g}}$	0.0384, Carbon content of biomass/yeast
$C_{\varepsilon 1}$	1	1.44, Constant in k-ε model

Variable	Unit	Description
$C_{\varepsilon 2}$	1	1.92, Constant in k-ε model
$C_{\varepsilon 3}$	1	$C_{\varepsilon 2}$, Constant in bubble induced turbulence k-ε model
C_{μ}	1	0.09, Constant in k-ε model
c	1	Stoichiometric coefficient
$c_{D\beta}$	1	Drag coefficient
$c_{D\beta,i}$	1	Drag coefficient of class i
$c_{D\beta\infty}$	1	Drag coefficient of a single bubble
$c_{D\beta\infty,cap}$	1	Drag coefficient of a single cap bubble
$c_{D\beta\infty,ellipsoid}$	1	Drag coefficient of a single ellipsoidal bubble
$c_{D\beta\infty,sphere}$	1	Drag coefficient of a single spherical bubble
$crit_1$	1	Decision criterion 1 for sequencing
$crit_2$	1	Decision criterion 2 for sequencing
c_{α}	$\frac{\mathrm{kg}}{\mathrm{m}^3}$	Concentration of oxygen in continuous phase, short form
c^*_{α}	$\frac{\mathrm{kg}}{\mathrm{m}^3}$	Saturation concentration of oxygen in continuous phase, short form
c_{α,O_2}	$\frac{\mathrm{kg}}{\mathrm{m}^3}$	Concentration of oxygen in continuous phase
c_{β,O_2}	$\frac{\mathrm{kg}}{\mathrm{m}^3}$	Concentration of oxygen in dispersed phase
$D_{p\beta}$	$\frac{\mathrm{kg\,m}}{\mathrm{s}^2}$	Drag force of single bubble
D_{α}	$\frac{\mathrm{m}^2}{\mathrm{s}}$	$2.45{\cdot}10^{-9}$, Diffusion coefficient of oxygen in continuous phase
D_{β}	$\frac{\mathrm{m}^2}{\mathrm{s}}$	$2.0 \cdot 10^{-5}$, Diffusion coefficient of oxygen in dispersed phase
d	1	Stoichiometric coefficient
d_p	m, mm	Relevant probe outer diameter
d_{β}	m, mm	Bubble equivalent diameter
$d_{\beta,1}$	m, mm	Bubble equivalent diameter class one
$d_{\beta,2}$	m, mm	Bubble equivalent diameter class two
$d_{\beta,3}$	m, mm	Bubble equivalent diameter class three
$d_{\beta,i}$	m, mm	Bubble equivalent diameter of class i
$d_{\beta,id}$	m, mm	Deviating bubble equivalent diameter of class i
E	$\frac{\mathrm{g}}{\mathrm{L}}$	Ethanol concentration
E_f	$\frac{\mathrm{kg}}{\mathrm{s}^2\mathrm{m}}$	Elastic modulus of fiber material
E_m	$\frac{\mathrm{kg}}{\mathrm{s}^2\mathrm{m}}$	Elastic modulus of matrix material

Variable	Unit	Description
E_p	$\frac{\mathrm{kg}}{\mathrm{s^2 m}}$	Elastic modulus
E^*	g	Ethanol
E_0	$\frac{\mathrm{g}}{\mathrm{L}}$	0, Initial ethanol concentration
$E_\parallel$	$\frac{\mathrm{kg}}{\mathrm{s^2 m}}$	Elastic modulus parallel to load direction
Eo	1	Eötvös number
F	$\frac{\mathrm{kg\,m}}{\mathrm{s^2}}$	Force
$f_{c_{D\beta\infty}}$	1	Correction factor for drag coefficient
$f_{p,red}$	1	Reduction factor
g	1	Stoichiometric coefficient
H	1	Hydrogen, in chemical formulas
H	1	equation 2.28
H_m	m	Mixture height in reactor above pressure probe
H_{m,O_2}	$\frac{\mathrm{s^2}}{\mathrm{m^2}}$	Henry constant
H_r	m, mm	Operation level
h	1	Stoichiometric coefficient
h_m	m	Liquid height in inclined tube manometer above pressure probe
h_p	m	0.3, Height of strain gauge cantilever probe
hx	1	Stoichiometric coefficient
I	m^4	Geometrical moment of inertia
i	1	Running variable
i	1	Stoichiometric coefficient
i_{CFX}	1	Volume element i in CFX
J	1	equation 2.27
j	1	Stoichiometric coefficient
K_e	$\frac{\mathrm{g}}{\mathrm{L}}$	0.1, Saturation constant ethanol uptake
K_i	$\frac{\mathrm{g}}{\mathrm{L}}$	10, Inhibition constant ethanol
K_s	$\frac{\mathrm{g}}{\mathrm{L}}$	0.12, Saturation constant glucose uptake
k	1	Stoichiometric coefficient
k	$\frac{\mathrm{m^2}}{\mathrm{s^2}}$	Turbulence kinetic energy
k_1	1	1.2, Constant in Sato model for bubble induced turbulence
k_L	$\frac{\mathrm{m}}{\mathrm{s}}$	$3.1 \cdot 10^{-4}$, Oxygen mass transfer coefficient
l	1	Stoichiometric coefficient
l_p	m	45, Length of strain gauge cantilever probe

Variable	Unit	Description
Mo	1	Morton number
M_{O_2}	$\frac{\text{kg}}{\text{mol}}$	$3.198 \cdot 10^{-2}$, Molecular weight of oxygen
$M_{\alpha x}$	$\frac{\text{kg}}{\text{m}^2\text{s}^2}$	Interphase momentum exchange term in x-direction
$M_{\alpha y}$	$\frac{\text{kg}}{\text{m}^2\text{s}^2}$	Interphase momentum exchange term in y-direction
$M_{\alpha z}$	$\frac{\text{kg}}{\text{m}^2\text{s}^2}$	Interphase momentum exchange term in z-direction
M_α	$\frac{\text{kg}}{\text{m}^2\text{s}^2}$	Overall interphase momentum exchange term for phase α
$M_{\alpha\beta}$	$\frac{\text{kg}}{\text{m}^2\text{s}^2}$	Interphase momentum exchange term from phase β to phase α
M_β	$\frac{\text{kg}}{\text{mol}}$	Molar mass of dispersed phase
m	1	Stoichiometric coefficient
m	kg	Mass
$\dot{m}_{Y,Matlab}$	$\frac{\text{kg}}{\text{sm}^3}$	Oxygen sink term in continuous phase as yeast representation, calculated in Matlab
$\dot{m}_{Y,O_2}$	$\frac{\text{kg}}{\text{sm}^3}$	Oxygen sink term in continuous phase as yeast representation, restricted
$\dot{m}_{\beta,i}$	$\frac{\text{kg}}{\text{sm}^3}$	Mass flow rate from phase β, i to phase α
N	1	Nitrogen, in chemical formulas
N_β	1	Number of dispersed phases
n	1	Stoichiometric coefficient
n	1	2, Correction exponent
$\underline{n}$	$[\underline{n}]$	Normal vector
n_{CFX}	1	Number of volume elements in CFX
$n_{p\beta}$	1	Number of bubbles in the element
n_{red}	1	Number of volume elements of reduced data set
nx	1	Stoichiometric coefficient
n_β	$\frac{\text{mol}}{\text{m}^3}$	Total mole concentration in dispersed phase
$n_{\beta,0}$	$\frac{\text{mol}}{\text{m}^3}$	44.615, Initial total mole concentration in dispersed phase
n_{β,O_2}	$\frac{\text{mol}}{\text{m}^3}$	Mole concentration of oxygen in dispersed phase
$n_{\beta,O_2,0}$	$\frac{\text{mol}}{\text{m}^3}$	9.3468, Initial mole concentration of oxygen in dispersed phase

Variable	Unit	Description
O	1	Oxygen, in chemical formulas
O	$\frac{\mathrm{g}}{\mathrm{L}}$	Oxygen concentration
O^*	g	Oxygen
$O_{\alpha 0}$	$\frac{\mathrm{g}}{\mathrm{L}}$	0.00152, Initial oxygen concentration, liquid
$O_{\beta 0}$	$\frac{\mathrm{g}}{\mathrm{L}}$	0.29963, Initial oxygen concentration, gas
ox	1	Stoichiometric coefficient
P	$\frac{\mathrm{kg}}{\mathrm{s^2 m}}$	Mean pressure
P_α	$\frac{\mathrm{kg}}{\mathrm{m\,s^3}}$	Turbulence production term
p_N	$\frac{\mathrm{kg}}{\mathrm{s^2 m}}$	101325, Normal pressure
p_α	$\frac{\mathrm{kg}}{\mathrm{s^2 m}}$	Pressure in continuous phase
p'_α	$\frac{\mathrm{kg}}{\mathrm{s^2 m}}$	3170, Saturation vapor pressure in continuous phase
p^∞_β	$\frac{\mathrm{kg}}{\mathrm{s^2 m}}$	Ambient pressure
$p^\infty_{\beta,i}$	$\frac{\mathrm{kg}}{\mathrm{s^2 m}}$	Partial pressure of component i in the core of the dispersed phase
p_{β,O_2}	$\frac{\mathrm{kg}}{\mathrm{s^2 m}}$	Partial pressure of oxygen in the dispersed phase
$q_{e_{an}}$	$\frac{\mathrm{g}}{\mathrm{gh}}$	Ethanol uptake rate anabolism
q_{ec}	$\frac{\mathrm{g}}{\mathrm{gh}}$	Ethanol uptake rate
$q_{e_{en}}$	$\frac{\mathrm{g}}{\mathrm{gh}}$	Ethanol uptake rate energy metabolism
q_{ep}	$\frac{\mathrm{g}}{\mathrm{gh}}$	Ethanol production rate
q_m	$\frac{\mathrm{g}}{\mathrm{gh}}$	0.01, glucose uptake rate for maintenance
q_{O_2}	$\frac{\mathrm{g}}{\mathrm{gh}}$	Oxygen uptake rate
$q_{O_2,0,s}$	$\frac{\mathrm{g}}{\mathrm{gh}}$	Sequence initial oxygen uptake rate
$q_{O_2,in}$	$\frac{\mathrm{g}}{\mathrm{Lh}}$	Oxygen input rate gassing system
$q_{O_2,max}$	$\frac{\mathrm{g}}{\mathrm{gh}}$	0.3, maximum oxygen uptake rate
$q_{O_2 s}$	$\frac{\mathrm{g}}{\mathrm{gh}}$	Oxygen uptake rate glucose oxidation
q_s	$\frac{\mathrm{g}}{\mathrm{gh}}$	Glucose uptake rate
$q_{s,crit}$	$\frac{\mathrm{g}}{\mathrm{gh}}$	Critical glucose uptake rate
$q_{s,in}$	$\frac{\mathrm{g}}{\mathrm{Lh}}$	Glucose feed rate
$q_{s,in,0}$	$\frac{\mathrm{g}}{\mathrm{Lh}}$	1.21, Initial glucose feed rate
$q_{s,in,max}$	$\frac{\mathrm{g}}{\mathrm{Lh}}$	1.72, Maximum glucose feed rate
$q_{s,max}$	$\frac{\mathrm{g}}{\mathrm{gh}}$	2.4, maximum glucose uptake rate
q_{s_f}	$\frac{\mathrm{g}}{\mathrm{gh}}$	Glucose uptake rate fermentative growth

Variable	Unit	Description
$q_{s_f an}$	$\frac{\mathrm{g}}{\mathrm{gh}}$	Glucose uptake rate fermentative anabolism
$q_{s_f en}$	$\frac{\mathrm{g}}{\mathrm{gh}}$	Glucose uptake rate fermentative energy metabolism
$q_{s_{ox}}$	$\frac{\mathrm{g}}{\mathrm{gh}}$	Glucose uptake rate oxidative growth
$q_{s_{ox}an}$	$\frac{\mathrm{g}}{\mathrm{gh}}$	Glucose uptake rate oxidative anabolism
$q_{s_{ox}en}$	$\frac{\mathrm{g}}{\mathrm{gh}}$	Glucose uptake rate oxidative energy metabolism
R	$\frac{\mathrm{kg\,m^2}}{\mathrm{K\,mol\,s^2}}$	8.314472, Gas constant
R_1	Ω	Electric resistance
R_2	Ω	Electric resistance
R_3	Ω	Electric resistance
R_4	Ω	Electric resistance
Re_p	1	Probe Reynolds number
Re_β	1	Dispersed phase Reynolds number
r_f	1	Volume fraction of fiber material in composite
$r_{f\parallel}$	1	Volume fraction of fiber material in composite parallel to load direction
$r_{f\perp}$	1	Volume fraction of fiber material in composite perpendicular to load direction
r_m	1	Volume fraction of matrix material in composite
r_α	1	Volume fraction of continuous phase
r_β	1	Volume fraction of dispersed phase
r_β^*	1	Local volume fraction of dispersed phase
$r_{\beta i}$	1	Volume fraction of dispersed phase i
$r_{\beta id}$	1	Deviating volume fraction of dispersed phase i
$r_{\beta i}^*$	1	Local volume fraction of dispersed phase i
S	$\frac{\mathrm{g}}{\mathrm{L}}$	Glucose concentration
S^*	g	Glucose
S_0	$\frac{\mathrm{g}}{\mathrm{L}}$	0.000236, Initial glucose concentration
$S_{M\alpha}$	$\frac{\mathrm{kg}}{\mathrm{sm^3}}$	Mass source term
$S_{Mx\alpha}$	$\frac{\mathrm{kg}}{\mathrm{m^2s^2}}$	External body forces in x-direction
$S_{My\alpha}$	$\frac{\mathrm{kg}}{\mathrm{m^2s^2}}$	External body forces in y-direction
$S_{Mz\alpha}$	$\frac{\mathrm{kg}}{\mathrm{m^2s^2}}$	External body forces in z-direction
S_{crit}	$\frac{\mathrm{g}}{\mathrm{L}}$	0.04, critical glucose concentration for overflow metabolism

Variable	Unit	Description
S_{in}	$\frac{\mathrm{g}}{\mathrm{L}}$	270, Glucose feed concentration
s	mm	Strain gauge cantilever probe tip deflection
T	$\frac{\mathrm{kg\,m^2}}{\mathrm{s^2}}$	Torque
Tu	1	Turbulence intensity
$T_{\alpha\beta k}$	$\frac{\mathrm{kg}}{\mathrm{m\,s^3}}$	Additional term from bubble induced turbulence model for k-equation
$T_{\alpha\beta\varepsilon}$	$\frac{\mathrm{kg}}{\mathrm{m\,s^3}}$	Additional term from bubble induced turbulence model for ε-equation
T_α	K	Temperature of continuous phase
T_β	K	Temperature of dispersed phase
t	h	Time
t_0	h	Start time
t_L	h	0.75, lag time
U_b	V	Bridge voltage
U_f	V	Feeding voltage
U_α	$\frac{\mathrm{m}}{\mathrm{s}}$	Mean velocity component of the continuous phase in x-direction
u	$[u]$	Exemplary variable
u	$\frac{\mathrm{m}}{\mathrm{s}}$	Velocity or velocity component in x-direction
u_n	$\frac{\mathrm{m}}{\mathrm{s}}$	Normal component of velocity
$u_{\beta 0}$	$\frac{\mathrm{m}}{\mathrm{s}}$	Superficial gas velocity
u_t	$\frac{\mathrm{m}}{\mathrm{s}}$	Terminal rise velocity
$\underline{u}_\alpha$	$\frac{\mathrm{m}}{\mathrm{s}}$	Velocity vector of the continuous phase
$\underline{u}_\beta$	$\frac{\mathrm{m}}{\mathrm{s}}$	Velocity vector of the dispersed phase
V	m^3, L	Volume
V_0	m^3, L	130, Initial volume
$V_{0,s}$	m^3, L	Sequence initial volume
V_{CFX}	m^3, L	Overall volume in CFX
$V_{CFX,vc}$	m^3, L	Overall volume in CFX after growth sequence
$V_{i,CFX}$	m^3, L	Volume of volume element i in CFX
V_M	$\frac{\mathrm{m}^3}{\mathrm{mol}}$	$2.2414 \cdot 10^{-2}$Mole volume
V_{red}	m^3, L	Volume of volume element of reduced data set
$V_{red,vc}$	m^3, L	Volume of volume element of reduced data set after growth sequence

Variable	Unit	Description
V_α	$\frac{\mathrm{m}}{\mathrm{s}}$	Mean velocity component of the continuous phase in y-direction
V_β	m^3	Total volume of dispersed phase
$V_{\beta,i}$	m^3	Volume of component i in the dispersed phase
v	$\frac{\mathrm{m}}{\mathrm{s}}$	Velocity component in y-direction
var	$[var]$	Variable
var_c	$[var_c]$	Variable consumption term
var_p	$[var_p]$	Variable production term
W_p	m^3	Section modulus
W_α	$\frac{\mathrm{m}}{\mathrm{s}}$	Mean velocity component of the continuous phase in z-direction
w	$\frac{\mathrm{m}}{\mathrm{s}}$	Velocity component in z-direction
X	$\frac{\mathrm{g}}{\mathrm{L}}$	Biomass/yeast concentration
X^*	g	Biomass/yeast
$X_{\beta,i}$	1	Fraction of component i in dry air
X_{β,O_2}	1	Oxygen mole fraction in dry air
X_0	$\frac{\mathrm{g}}{\mathrm{L}}$	7.0628, Initial biomass concentration
$X_{0,s}$	$\frac{\mathrm{g}}{\mathrm{L}}$	Sequence initial biomass concentration
x	m, mm	First Cartesian coordinate
x_p	m, mm	First Cartesian probe coordinate
Y_{es}	$\frac{\mathrm{g}}{\mathrm{g}}$	0.51, Ethanol yield on glucose
Y_{oe}	$\frac{\mathrm{g}}{\mathrm{g}}$	2.087, Coefficient of respiration on ethanol
Y_{os}	$\frac{\mathrm{g}}{\mathrm{g}}$	1.067, Coefficient of respiration on glucose
Y_{xe}	$\frac{\mathrm{g}}{\mathrm{g}}$	0.72, Biomass yield on ethanol
Y_{xs_f}	$\frac{\mathrm{g}}{\mathrm{g}}$	0.1, Biomass yield on glucose, fermentative
$Y_{xs_{ox}}$	$\frac{\mathrm{g}}{\mathrm{g}}$	0.48, Biomass yield on glucose, oxidative
y	m, mm	Second Cartesian coordinate
y_p	m, mm	Second Cartesian probe coordinate
y	$[y]$	Exemplary function
y_0	$[y]$	Initial value for exemplary function y
z	m, mm	Third Cartesian coordinate
z_p	m, mm	Third Cartesian probe coordinate

Greek Symbols

Symbol	Unit	Description
α	1	Index of continuous phase
α_B	1	$2.844 \cdot 10^{-2}$, Bunsen absorption coefficient
α_i	$^\circ$	Angle of incident flow direction
α_p	$^\circ$	Inclination angle of inclined tube manometer
β	1	Index of dispersed phase
$\Gamma_{\alpha\beta}$	$\frac{\mathrm{kg}}{\mathrm{s\,m^3}}$	Mass flow rate from phase β to α
γ	1	1, Relative humidity
Δ	1	Difference
Δt	s	0.005,Time step
Δt_c	s	0.01, Coarse time step
Δt_f	s	0.0025, Fine time step
Δt_m	s	0.005, Medium time step
Δx	m	Characteristic element length
Δx_c	m	Characteristic element length, coarse mesh
Δx_f	m	Characteristic element length, fine mesh
Δx_m	m	Characteristic element length, medium mesh
$\delta_{\alpha\beta}$	1	Kronecker operator, 1 for $\alpha = \beta$ and 0 for $\alpha \neq \beta$
ε	$\frac{\mathrm{m^2}}{\mathrm{s^3}}$	Turbulent energy dissipation rate
ε_p	1	Outer fiber strain
η_{ref}	$\frac{\mathrm{kg}}{\mathrm{s\,m}}$	0.0009, Reference viscosity
$\eta_{t,bit}$	$\frac{\mathrm{kg}}{\mathrm{s\,m}}$	Bubble induced dynamic viscosity of continuous phase
η_α	$\frac{\mathrm{kg}}{\mathrm{s\,m}}$	$8.899 \cdot 10^{-4}$, Dynamic viscosity of continuous phase
$\eta_{\alpha eff}$	$\frac{\mathrm{kg}}{\mathrm{s\,m}}$	Effective dynamic viscosity
$\eta_{\alpha t}$	$\frac{\mathrm{kg}}{\mathrm{s\,m}}$	Turbulent/eddy dynamic viscosity of continuous phase
$\eta_{\beta t}$	$\frac{\mathrm{kg}}{\mathrm{s\,m}}$	Turbulent/eddy dynamic viscosity of dispersed phase
λ_α	$\frac{\mathrm{kg}}{\mathrm{s\,m}}$	Second dynamic viscosity of continuous phase
μ	$\frac{1}{\mathrm{h}}$	Specific growth rate
ξ	$\frac{\mathrm{kg}}{\mathrm{s^2 m}}$	Pressure probe maximum deviation

Symbol	Unit	Description
ϱ_c	$\frac{\mathrm{kg}}{\mathrm{m}^3}$	1,384, Mass density of the composite
ϱ_f	$\frac{\mathrm{kg}}{\mathrm{m}^3}$	1,797, Mass density of the fiber material
ϱ_m	$\frac{\mathrm{kg}}{\mathrm{m}^3}$	1,161, Mass density of the matrix material
ϱ_α	$\frac{\mathrm{kg}}{\mathrm{m}^3}$	997, Mass density of continuous phase, water
ϱ_β	$\frac{\mathrm{kg}}{\mathrm{m}^3}$	Mass density of dispersed phase, air
σ	$\frac{\mathrm{kg}}{\mathrm{s}^2}$	Surface tension coefficient
σ_{k_α}	1	1, Constant in k-ε model
σ_p	$\frac{\mathrm{kg}}{\mathrm{s}^2\,\mathrm{m}}$	Outer fiber tension
$\sigma_{\varepsilon_\alpha}$	1	1.3, Constant in k-ε model
Φ	$[\Phi]$	Mean of flow property
$\varphi(t)$	$[\varphi(t)]$	Flow property
φ'	$[\varphi']$	Fluctuating component of flow property
ω_{1a}	Hz	Estimated first eigen frequency
ω_{1b}	Hz	Estimated first eigen frequency
ω_{1c}	Hz	Estimated first eigen frequency

Universal Constants

Constant	Unit	Value, Description
e	1	2.71828, Base of the natural logarithm
g	$\frac{\mathrm{m}}{\mathrm{s}^2}$	9.81, Gravitational acceleration
π	1	3.14159, Circular constant
R	$\frac{\mathrm{kg}\,\mathrm{m}^2}{\mathrm{K}\,\mathrm{mol}\,\mathrm{s}^2}$	8.314472, Universal gas constant

Special Symbols, Abbreviations

Symbol	Unit	Description
d	–	differential symbol
$[i]$	–	Convention for units of variable i
$[i,j]$	–	Closed interval, including i and j
$]i,j[$	–	Open interval, excluding i and j
$\lvert i \rvert$	$[i]$	Magnitude of i
$\max(i)$	$[i]$	Maximum of i
$\min(i)$	$[i]$	Minimum of i
pH	–	pH-value
$\stackrel{!}{=}$	–	must equal
$\frac{\mathrm{D}u}{\mathrm{D}t}$	$\frac{[\mathrm{u}]}{\mathrm{s}}$	Total derivative of variable u with respect to time, $\frac{\partial u}{\partial t} + \frac{\partial u}{\partial x}\frac{\partial x}{\partial t} + \frac{\partial u}{\partial y}\frac{\partial y}{\partial t} + \frac{\partial u}{\partial z}\frac{\partial z}{\partial t}$
$\frac{\partial}{\partial i}$	$\frac{1}{[\mathrm{i}]}$	Partial derivative with respect to i
$\overline{i}$	$\left[\overline{i}\right]$	Time average of i
i'	$[i']$	Fluctuating component of i
$\underline{i}$	$[\underline{i}]$	Vector
BIT	–	Bubble Induced Turbulence
CFD	–	Computational Fluid Dynamics
CFL	1	Courant-Friedrichs-Lewy number
CFX	–	CFD code by Ansys
CPU	–	Central Processing Unit
DNS	–	Direct Numerical Simulation
EDM	–	Electro Diffusion Measurement
F-LDA	–	Fiber Laser Doppler Anemometry
HFA	–	Hot-Film Anemometry
HPLC	–	High Performance Liquid Chromatography
HWA	–	Hot-Wire Anemometry
LCA	–	Laser Cantilever Anemometry
LDA	–	Laser Doppler Anemometry
MMF-LDA	–	Multi Mode Fiber Laser Doppler Anemometry
NG	–	Neural Gas
PC	–	Personal Computer

Symbol	Unit	Description
PIV	–	Particle Image Velocimetry
PMMA	–	Polymethylmethacrylate
PT	–	Particle tracking
PTV	–	Particle Tracking Velocimetry
RAM	–	Random Access Memory
RMS	–	Root mean square
SOM	–	Self-Organizing Map
UDA	–	Ultrasonic Doppler Anemometry
VOF	–	Volume of Fluid
XP	–	Operating System by Microsoft